Laboratory Investigation of Collisionless Kinetic Effects and 3D Topological Triggers for Magnetic Reconnection

by

Paul D. Gradney

A dissertation submitted in partial fulfillment of
the requirements for the degree of

Doctor of Philosophy

(Physics)

at the

UNIVERSITY OF WISCONSIN–MADISON

2025

Date of final oral examination: 11/05/2025

The dissertation is approved by the following members of the Final Oral Committee:
Jan Egedal, Professor, Physics
Cary Forest, Professor, Physics
Stanislav Boldyrev, Professor, Physics
Benedikt Geiger, Professor, Engineering

To Alisa.

LABORATORY INVESTIGATION OF COLLISIONLESS KINETIC EFFECTS AND 3D TOPOLOGICAL TRIGGERS FOR MAGNETIC RECONNECTION

Paul D. Gradney

Under the supervision of Professor Jan Egedal
At the University of Wisconsin-Madison

Magnetic reconnection is a fundamental plasma process responsible for the rapid conversion of magnetic energy into particle energy. This process occurs ubiquitously in astrophysical, space, and laboratory plasmas, including solar flares, Earth's magnetosphere, and fusion devices. Despite its importance, key questions remain, including how reconnection dynamics are modified in the collisionless kinetic regime, and what mechanisms trigger fast reconnection in three-dimensional (3D) systems as they transition from stable or quasi-stable magnetic configurations to configurations that enable rapid energy release.

This thesis presents experimental studies of collisionless magnetic reconnection using the Terrestrial Reconnection EXperiment (TREX) at the Wisconsin Plasma Physics Laboratory (WiPPL). To minimize collisional effects and access the kinetic regime relevant to space plasmas, a reconnection Drive Cylinder was developed. This system increases both the effective system size and the driving rate of reconnection, enabling TREX to reach a regime where electron dynamics are dominated by kinetic rather than collisional processes. Technical details of the Drive Cylinder design, including its coil configuration and magnetic field shaping, are presented along with measurements of its performance.

Using the 3-coil TREX configuration, the dynamics of 3D reconnection were investigated in a laboratory-generated mini-magnetosphere. Observations demonstrate that the explosive onset of reconnection can be triggered by a bifurcation of the magnetic topological structure. In particular, the rapid approach and crossing of separatrix surfaces led to the bifurcation of magnetic null points, restructuring of separator lines, and a marked increase in the reconnection electric field along the separator. These results provide experimental evidence that geometric reconfiguration of a 3D magnetic topology can initiate the onset of fast reconnection. The findings have broad implications for understanding space weather, astrophysical explosions, and relaxation events in magnetically confined laboratory plasmas.

TABLE OF CONTENTS

LIST OF TABLES

LIST OF FIGURES

1 INTRODUCTION

1.1 Scientific Motivation

Understanding the mechanisms of energy transfer in physical systems has guided many fundamental discoveries across physics. In plasma physics, one of the key relaxation process is magnetic reconnection [93, 72, 21], which governs the transition of energy between magnetic fields and plasma through the breaking and rejoining of magnetic field lines. This process alters the topology of magnetic field lines and frequently produces rapid energization of plasma particles. With plasma being the dominant form of visible matter in the universe, magnetic reconnection plays a crucial role in a wide range of astrophysical phenomena. Examples include solar flares [60], coronal mass ejections (CMEs) [58], and planetary solar storms [61, 103]. Beyond our solar system, reconnection has been invoked as a possible particle acceleration mechanism theorized to generate high-energy electrons responsible for gamma ray emissions[92].

A particularly important natural laboratory for reconnection is the interaction between the interplanetary magnetic field (IMF) and Earth's magnetosphere. Here, the solar wind impinges on Earth's magnetic field at super-Alfvènic speeds, driving the formation of a bow shock on the dayside and establishing the magnetopause current sheet (an illustrative representation is shown in Fig. 1.1(a)). Reconnection at this boundary is typically asymmetric because Earth's magnetic field is stronger while the solar-wind plasma is denser. In its simplest description, anti-parallel reconnection occurs at the dayside magnetopause; the newly reconnected field lines are then convected tailward into the magnetotail, Fig. 1.1(b), where a second, nearly symmetric current sheet forms and further reconnection takes place. The reconnected flux subsequently returns earthward, channeling energetic particles into the polar ionosphere and producing the aurora borealis. This global circulation of magnetic flux and plasma, known as the Dungey cycle [20], illustrates the fundamental role of reconnection in coupling the solar wind to the magnetosphere.

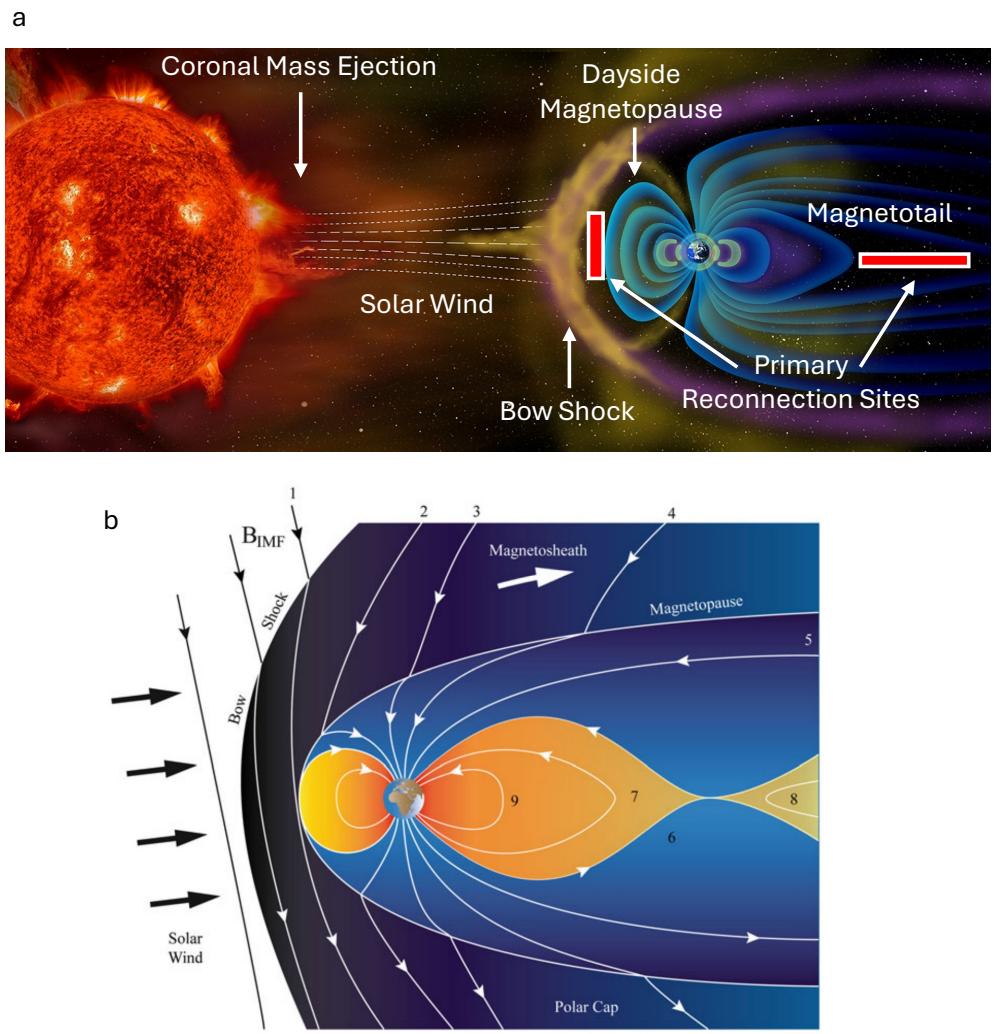

Figure 1.1: Panel (a) describes the different regions within the Earth's magnetosphere (Credit: NASA), and panel (a) is an illustration of the evolution of magnetic field lines (1-9) as they progress through the Dungey cycle. Figure taken from ref. [85].

The objective of this thesis to explore magnetic reconnection in two different systems: (1) a dedicated experiment designed to study controlled reconnection dynamics and (2) a configuration that mimics the interaction between the IMF and a mini-magnetosphere. By experimentally isolating and diagnosing the kinetic and three-dimensional (3D) aspects of reconnection, this work aims to identify plasma dynamics unique to the kinetic collisionless regime and to determine the mechanism for triggering fast reconnection in a physically relevant 3D geometry.

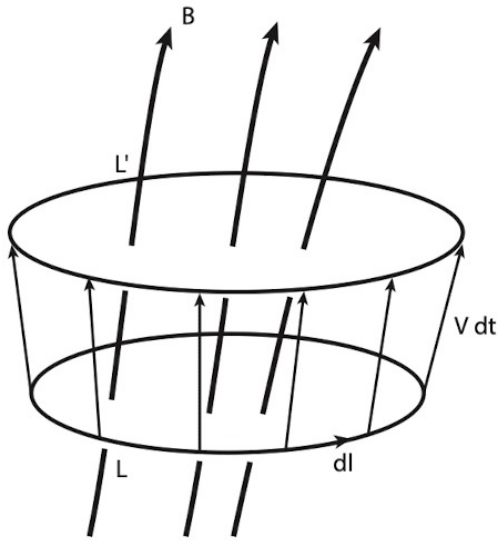

Figure 1.2: A schematic representing flux contour L moving with velocity V in a time dt to a new location at L′. [101]

1.2 2D Magnetic Reconnection

Magnetic reconnection in two dimensions (2D) provides the foundation for most theoretical and experimental descriptions of topological change in plasmas. In this framework, magnetic field lines lie in a single plane, typically the x–y plane, with the electric field oriented in the z direction. Reconnection proceeds where magnetic field lines of opposite direction are forced together, breaking and rejoining in a localized diffusion region.

1.2.1 Plasma Frozen-in Condition

In the ideal Magnetohydrodynamic (MHD) model, where the plasma has negligible resistivity, the plasma particles are often said to be frozen-in to the field lines. Consequently, any plasma elements located on a common magnetic field line of force at time t will remain on a common line of force at any future time t′. Significantly, the line of force at time t and t′ must be the same field line. This is known as the frozen-in condition, and is defined using the magnetic flux,

$$\Psi = \int \mathbf{B}\, \mathrm{d}\mathbf{a}, \tag{1.1}$$

through a closed contour L at time t and L′ at a later time t′, as shown in Fig. 1.2. The rate of change of flux is

$$\frac{d\Psi}{dt} = \int \frac{\partial \mathbf{B}}{\partial t} \cdot d\mathbf{a} + \oint \mathbf{B} \cdot (\mathbf{v} \times d\boldsymbol{l}), \tag{1.2}$$

where the first term represents the change in flux due to the changing magnetic field and the second term is due to the motion of the contour L to L′. This can be rewritten as

$$\frac{d\Psi}{dt} = -\int \nabla \times \mathbf{E} \cdot d\mathbf{a} + \oint (\mathbf{B} \times \mathbf{v}) \cdot d\boldsymbol{l}, \tag{1.3}$$

Where the first term invoked Faraday's law, $\nabla \times \mathbf{E} = -\partial \mathbf{B}/\partial t$, and the vector identity $\mathbf{A} \cdot (\mathbf{B} \times \mathbf{C}) = \mathbf{C} \cdot (\mathbf{A} \times \mathbf{B})$ was used for the second term. Finally, Stoke's theorem can be used on the second term, which gives the result

$$\frac{d\Psi}{dt} = -\int \nabla \times (\mathbf{E} + \mathbf{v} \times \mathbf{B}) \cdot d\mathbf{a}. \tag{1.4}$$

The term in the parenthesis of the integrand of equation 1.4 is Ohm's law, and for an ideal MHD plasma with negligible resistivity

$$\mathbf{E} + \mathbf{v} \times \mathbf{B} = 0, \tag{1.5}$$

which forces $d\Psi/dt = 0$.

A relationship between flux conservation and the frozen-in condition can be illustrated using Fig. 1.2. The figure shows three surfaces: the lower surface enclosed by L, the upper surface enclosed by L′, and the differential side surface swept out by the line element $d\mathbf{l}$ as it moves from L to L′ over a displacement $\mathbf{v}\,dt$. When magnetic flux is conserved, the total flux through one surface must equal the sum of the flux through the other two. To further clarify this concept, the loops L and L′ can be reduced in a width that encompasses a single magnetic field line. In this limit, the line of magnetic force acting on a charged particle remains constant and is described by the flux contour that threads the region.

This result naturally raises an important question, under what conditions is the frozen-in condition violated? The answer to this question defines the physical mechanisms by which magnetic reconnection occurs, with significant insight be provided from an examination of the generalized Ohm's law.

1.2.2 Generalized Ohm's Law

The generalized Ohm's law (GOL)provides a description of the momentum balance of the electron fluid. The importance of the electron momentum balance, as compared to the ion momentum balance, is due to the large mass difference, $m_i \gg m_e$. Consequently, the current is predominantly carried by electrons owing to their faster response to the electric field. In addition, the kinetic spacial scales that govern many magnetic reconnection dynamics are described by the electron motion. With these consideration, the necessary starting equation for determining the GOL is the electron plasma kinetic equation, which describes the evolution of the distribution function, $f_e(\mathbf{r}, \mathbf{v}, t)$, and is defined as

$$\left[\frac{\partial}{\partial t} + \mathbf{v}\cdot\nabla - \frac{e}{m_e}(\mathbf{E} + \mathbf{v}\times\mathbf{B})\cdot\nabla_v\right] f_e(\mathbf{r}, \mathbf{v}, t) = \left(\frac{\partial f_e}{\partial t}\right)_c, \tag{1.6}$$

in configuration space $\mathbf{r}$, velocity space $\mathbf{v}$, and time t. In equation 1.6, the ∇_v is the velocity space gradient operator, $\left(\frac{\partial f_\alpha}{\partial t}\right)_c$ is the collision operator, e is the charge of the electron, and m_e is the electron mass.

The electron momentum equation is found by taking the first moment of the kinetic equation, giving

$$m_e \int \mathbf{v}\left[\frac{\partial}{\partial t} + \mathbf{v}\cdot\nabla - \frac{e}{m_e}(\mathbf{E} + \mathbf{v}\times\mathbf{B})\cdot\nabla_v\right] f_e(\mathbf{r}, \mathbf{v}, t)\, d\mathbf{v} = m_e \int \mathbf{v}\left(\frac{\partial f_e}{\partial t}\right)_c d\mathbf{v}. \tag{1.7}$$

By taking movements of the distribution function, the following relations are found for the

macroscopic number density, n_e, and fluid velocity, $\mathbf{u}_e$

$$n \approx n_e = \int f_e \, d\mathbf{v}$$
$$\mathbf{u}_e = \frac{1}{n} \int \mathbf{v} f_e \, d\mathbf{v},$$

where the quasi-neutral plasma approximation, $n_e \approx n_i$, has been invoked. In addition, the collision term on the right side of equation 1.7 can be found by assuming an electron-ion plasma and calculate the flow relaxation rate between two Maxwellian distributions drifting slowly with respect to each other [ref Callen Notes section 2.4.1.5], resulting in

$$m_e \int \mathbf{v} \left(\frac{\partial f_e}{\partial t} \right)_c d\mathbf{v} = m_e \nu_{ei} \int \mathbf{v} f_e \, d\mathbf{v} = m_e \nu_{ei} n (\mathbf{u}_i - \mathbf{u}_e). \tag{1.8}$$

In the second integral, which describes the momentum transfer due to Coulomb collisions between the electrons and ions, ν_{ei} is the electron-ion collision frequency.

Combining the definitions for n, $\mathbf{u}_e$, and equation 1.8 with equation 1.7 yields the electron momentum balance equation

$$m_e n \left(\frac{\partial \mathbf{u}_e}{\partial t} + \mathbf{u}_e \cdot \nabla \mathbf{u}_e \right) = -en \left(\mathbf{E} + \mathbf{u}_e \times \mathbf{B} \right) - \nabla \cdot \mathbb{P} + m_e \nu_{ei} n (\mathbf{u}_i - \mathbf{u}_e), \tag{1.9}$$

where $\mathbb{P} = m_e \int (\mathbf{v} - \mathbf{u}_e)(\mathbf{v} - \mathbf{u}_e) f_e \, d\mathbf{v}$ is the pressure tensor. By substituting the current density $\mathbf{J} = ne(\mathbf{u}_i - \mathbf{u}_e)$ and the Spitzer resistivity $\eta = m_e \nu_{ei} / n_e e^2$ into equation 1.8, the last term of equation 1.9 becomes

$$m_e \nu_{ei} n (\mathbf{u}_i - \mathbf{u}_e) = ne(\eta \mathbf{J}). \tag{1.10}$$

The GOL is then found by substituting equation 1.10 into 1.9 and solving for $\mathbf{E} + \mathbf{u}_e \times \mathbf{B}$, which gives

$$\mathbf{E} + \mathbf{u}_e \times \mathbf{B} = \eta \mathbf{J} - \frac{1}{ne} \nabla \cdot \mathbb{P} - \frac{m_e}{e} \left(\frac{\partial \mathbf{u}_e}{\partial t} + \mathbf{u}_e \cdot \nabla \mathbf{u}_e \right) \tag{1.11}$$

In this form, each term on the right side of equation 1.11 describes a possible path by which the frozen-in condition can be broken. Where breaking the frozen in condition means $\nabla \times \mathbf{E} \neq 0$ such that an inductive field is permitted. An additional term, which describes the Hall current but does not break the frozen in condition, can be found by substituting $\mathbf{u}_e = \mathbf{u}_i - \mathbf{J}/ne$ into the second term of equation 1.11 in the following manner,

$$\mathbf{u}_e \times \mathbf{B} = \mathbf{u}_i \times \mathbf{B} - \frac{1}{ne}(\mathbf{J} \times \mathbf{B}). \tag{1.12}$$

This gives the final form of the GOL

$$\mathbf{E} + \mathbf{u}_i \times \mathbf{B} = \eta \mathbf{J} + \frac{\mathbf{J} \times \mathbf{B}}{ne} - \frac{1}{ne}\nabla \cdot \mathbb{P} - \frac{m_e}{e}\left(\frac{\partial \mathbf{u}_e}{\partial t} + \mathbf{u}_e \cdot \nabla \mathbf{u}_e\right) \tag{1.13}$$

This final form not only describes how the frozen-in condition can be broken, but also how the rate of reconnection and the dynamics of both the macro and micro scales change as different terms become more influential at different scale length.

The terms in equation 1.13 are ordered such that their influence on electron dynamics increases as collisionality, spatial scales, and temporal scales decrease. The resistive diffusion term, $\eta\mathbf{J}$, dominates in the MHD regime of a collisional plasma and provides a mechanism for breaking the frozen-in condition. The Hall term, $\mathbf{J} \times \mathbf{B}/(ne)$, is a two-fluid effect that modifies plasma dynamics when the width of the diffusion region approaches the ion inertial length. The pressure tensor term, $\nabla \cdot \mathbb{P}/(ne)$, has different effects depending on the characteristic scale length. In the MHD and two-fluid regimes, the pressure tensor is approximated as $\mathbb{P} \approx p\mathbb{I}$, where p is the isotropic scalar pressure. This approximation enforces pressure balance, helping the current layer maintain its structure during reconnection. In the kinetic regime, where electrons are well magnetized and the electron collision time exceeds the transit time of an electron fluid element through the diffusion region, the pressure tensor is typically well approximated by its gyrotropic form and can be expressed as $\mathbb{P} \approx p_\perp \mathbb{I} + (p_\parallel - p_\perp)\hat{\mathbf{b}}\hat{\mathbf{b}}$. Here, $p_\parallel$ and $p_\perp$ are the electron pressures parallel

and perpendicular to the magnetic field, respectively. These diagonal components do not directly violate the frozen-in condition but can significantly influence electron dynamics.

At scales smaller than the electron inertial length, the off-diagonal elements of the pressure tensor become significant and contribute to breaking the frozen-in condition. At this length scale, the final term of equation 1.13, referred to as the inertial term, can also contribute to breaking the frozen-in condition. The effects from the inertial term are most noticeable when asymmetric conditions exist. A more thorough examination of each of these regimes is discussed in the following sections.

1.2.3 Resistive Diffusion

Examining the GOL with only the resistivity term, such that the single fluid MHD approximations are used, provides a description of the plasma when the electrons and ions are strongly coupled through Coulomb collisions. Equation 1.13 becomes

$$\mathbf{E} + \mathbf{v} \times \mathbf{B} = \eta \mathbf{J}, \tag{1.14}$$

where $\mathbf{v}$ represents the center of mass flow of the ions, with $\mathbf{v} = \mathbf{u}_i$ due to the fluid momentum being carried by the ions. Using Faraday's law, Amperes law, and the divergence free property of the magnetic field

$$\nabla \times \mathbf{E} = -\frac{d\mathbf{B}}{dt} \tag{1.15}$$

$$\nabla \times \mathbf{B} = \mu_0 \mathbf{J} \tag{1.16}$$

$$\nabla \cdot \mathbf{B} = 0 \tag{1.17}$$

the magnetic induction equation can be derived, which states

$$\frac{\partial \mathbf{B}}{\partial t} = \nabla \times (\mathbf{v} \times \mathbf{B}) + \frac{\eta}{\mu_0} \nabla^2 \mathbf{B}. \tag{1.18}$$

Here, the convective and diffusive components of the field are described by the first and second terms on the right, respectively. A useful quantity for comparing these terms is the Lundquist number,

$$S = \frac{\mu_0 L v_A}{\eta}, \tag{1.19}$$

a dimensionless value defined by the ratio of the convective term to the diffusive term of equation 1.18.

When the convective term is much greater than the diffusion term, field lines in a system size L will move with the bulk flow velocity at time scales of

$$\tau_c \sim \frac{L}{v_A}, \tag{1.20}$$

where the Alfvén speed, $v_A = B/\sqrt{\mu_0 n m_i}$, is the characteristic flow velocity in MHD. Applying this to the solar wind, the convection time to Earth is approximately 2 to 5 days, using $300\,\mathrm{km/s} \leqslant v_A \leqslant 800\,\mathrm{km/s}$ and L = 1AU, which agrees very well with observations. In contrast to this agreement, examining the diffusive time scale gives

$$\tau_d = \frac{\mu_0 L^2}{\eta} = 10^{-9} L^2 T^{3/2}, \tag{1.21}$$

with τ_d, L, and,T in seconds, meters and degrees K, respectively. Applying this to a typical coronal length scale, $L = 10^7$ m, and temperature, $T = 10^6$ K, yields a diffusion time of $\tau_d = 10^{14}$ sec or ~3 million years. This result demonstrates how this description is unable to capture the observed time scales for energetic changes in the reconfiguration of magnetic field line toplogies in the sun.

1.2.4 Sweet-Parker Reconnection

In 1943, Giovanelli first proposed that an electric field near a magnetic null point could accelerate charged particles [34]. This concept was later reinforced by Crowling [11], who

recognized that a current sheet formed by the collapse of an X-type null point would naturally produce such particle acceleration. Building on these ideas, Sweet [93] and Parker [72] developed a steady-state model of magnetic reconnection, where "steady state" implies that the global configuration evolves slowly compared to many Alfvèn transit times. In their model, magnetic field lines change connectivity, allowing plasma elements initially located along a single field line in the inflow region to emerge on different field lines in the outflow region.

As with resistive diffusion, the Sweet–Parker model is formulated within the framework of resistive MHD and assumes a thin, elongated current sheet ($L \gg \delta$), where L and δ denote the half-length and half-width of the sheet, respectively, as illustrated in Fig. 1.3. A key distinction from simple resistive diffusion is that, in the Sweet–Parker model, the global reconnection dynamics are governed by the narrow width of the diffusion region rather than its overall length. This geometric constraint results in a substantially higher rate at which magnetic field lines can diffuse through the current sheet compared with standard resistive diffusion.

The Sweet-Parker model is a 2D description of anti-parallel fields, B_{in}, driven towards each other in the presence of plasma. This field configuration is shown in the shaded gray region of Fig. 1.3(a), where the orange region represents the finite current layer that forms about the $\mathbf{B} = 0$ region. Using the ideal MHD Ohm's law, equation 1.5, for the inflow region (outside the current sheet) and the resistive Ohm's law, equation 1.14, for the outflow region (inside the current sheet), gives the following relations respectively

$$E_{in} = v_{in} B_{in}, \tag{1.22}$$

$$E_z = \eta J_z \tag{1.23}$$

where $E_{in} = E_z$. Here, the continuity of E follows from $\nabla \times \mathbf{E} = 0$, due to the convective and diffusive terms of equation 1.18 canceling at the boundary.

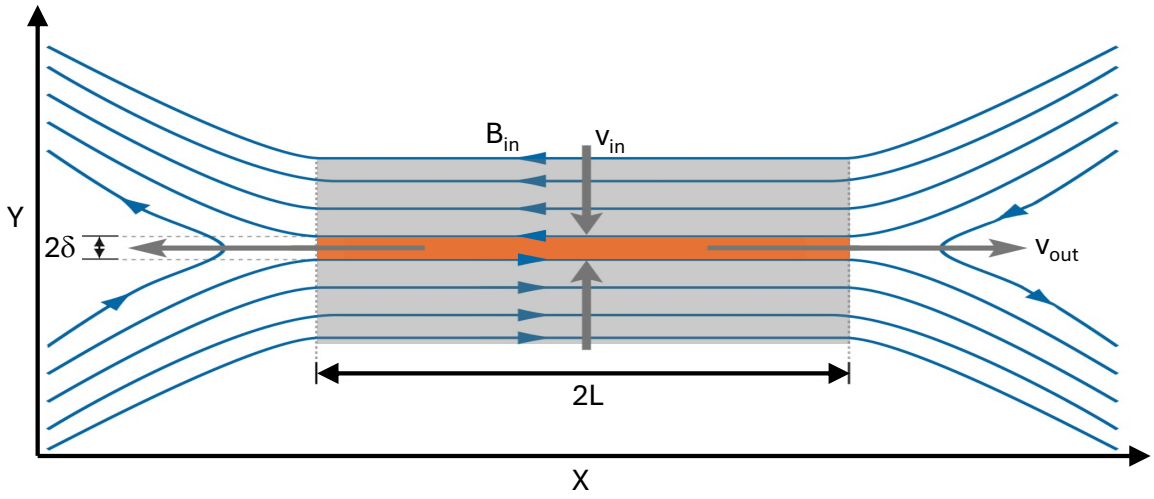

Figure 1.3: An illustration of the Sweet – Parker large aspect ratio magnetic reconnection field configuration. The gray region indicates the ant-parallel reconnection geometry used in the Sweet-Parker reconnection analysis. It is important to note the field lines have no curvature in this region, a detail that is exploited in the analysis. In this region, the orange shaded area is the reconnection current sheet, or diffusion region. Inside the diffusion region force balance is achieved between the magnetic pressure, $p_{mag} = B_x^2/2\mu_0$, and the plasma pressure, $p_{plasma} = B_{max}^2/2\mu_0 - p_{mag}$.

An Amperian loop can be used to calculate the current induced by B_{in}, which yields

$$B_{in} = \delta \mu_0 J_z. \tag{1.24}$$

Combining equations 1.22 and 1.23, and substituting J_z with equation 1.24 gives

$$v_{in} = \frac{\eta}{\mu_0 \delta} \tag{1.25}$$

An equation for v_{out} can be found by examining the MHD force balance equation, which is

$$\rho \frac{\partial \mathbf{v}}{\partial t} + \rho(\mathbf{v} \cdot \nabla)\mathbf{v} = -\nabla p + \mathbf{J} \times \mathbf{B}, \tag{1.26}$$

where $\rho = n m_i$ is the ion mass density and $p = n T_e$ is the scalar pressure. By substituting

$\mathbf{J} = \frac{1}{\mu_0}\nabla \times \mathbf{B}$ and using $\nabla \cdot \mathbf{B} = 0$, equation 1.26 becomes

$$\rho(\mathbf{v} \cdot \nabla)\mathbf{v} = -\nabla\left(\frac{B^2}{2\mu_0} + p\right) + \frac{1}{\mu_0}\nabla(\mathbf{BB}). \tag{1.27}$$

The last term in equation 1.27 represents the magnetic tension force due to field line curvature. Since the Sweet-Parker model considers only anti-parallel fields, as indicated by the gray region of Fig. 1.3, this term can be dropped. By first considering the inflow direction, the term on the left side of equation 1.27 is zero due to symmetry about $x = 0$. Therefore, the force balance in the inflow direction is

$$\frac{\partial}{\partial x}\left(\frac{B_{in}^2}{2\mu_0} + p_{in}\right) \approx 0, \tag{1.28}$$

which yields

$$\frac{B_{in}^2}{2\mu_0} + p_{in} \approx p_{max}, \tag{1.29}$$

where p_{max} is a constant equal to the max plasma pressure that offsets the minimum magnetic pressure inside the current layer.

Similarly, for the out flow region, equation 1.27 can be rewritten using $v_{out}\frac{\partial v_{out}}{\partial y} = \frac{1}{2}\frac{\partial {v_{out}}^2}{\partial y}$, and the understanding that $B = 0$ in this region, gives

$$\frac{1}{2}\rho {v_{out}}^2 + p_{in} \approx p_{max}. \tag{1.30}$$

v_{out} is then found by solving for the pressure difference and setting equations 1.29 and 1.30 equal to each other, which gives

$$v_{out} = \frac{B_{in}}{\sqrt{\mu_0\rho}} = v_A. \tag{1.31}$$

Lastly, the relationship between v_{in} and v_{out} is found from the conservation of mass, which

states

$$\frac{\partial \rho}{\partial t} + \nabla \cdot (\rho \mathbf{v}) = 0. \tag{1.32}$$

Using the steady state assumption, and invoking the divergence theorem, this can be written as

$$\rho \oint \mathbf{v} \cdot \, d\mathbf{a} = \rho \left(L v_{in} - \delta v_{out} \right) = 0. \tag{1.33}$$

Solving for v_{in}/v_{out}, and using equations 1.25 and 1.31, gives the normalized reconnection rate

$$\alpha = \frac{v_{in}}{v_{out}} = \frac{\delta}{L} = \sqrt{\frac{\eta}{\mu_0 v_A L}}. \tag{1.34}$$

comparing this to equation 1.19, gives the result

$$\alpha = S^{-1/2}. \tag{1.35}$$

In addition, equation 1.22 can be written in terms of α by substituting $v_{in} = \alpha v_A$, resulting in

$$\alpha = \frac{E_z}{v_A B_{in}} = \frac{E_{rec}}{v_A B_{rec}} \tag{1.36}$$

where the final equality defines the inductive field as the reconnection electric field and the inflow magnetic field as the reconnection magnetic field. It is important to note that the reconnection electric field is often referred to as the reconnection rate, since by Faraday's law the reconnection electric field is the rate by which magnetic flux is transported across the X-point.

A reconnection time scale for Sweet-Parker can be found from equations 1.34 and 1.35, which gives

$$\tau_d = \frac{\mu_0 L^2}{\eta} S^{-1/2} = 10^{-9} L^2 T^{3/2} S^{-1/2}, \tag{1.37}$$

with L in meters and T in degrees K. Due to the dependence on the Lundquist number, this diffusion time is still far to large for systems with high Lundquist numbers, such as

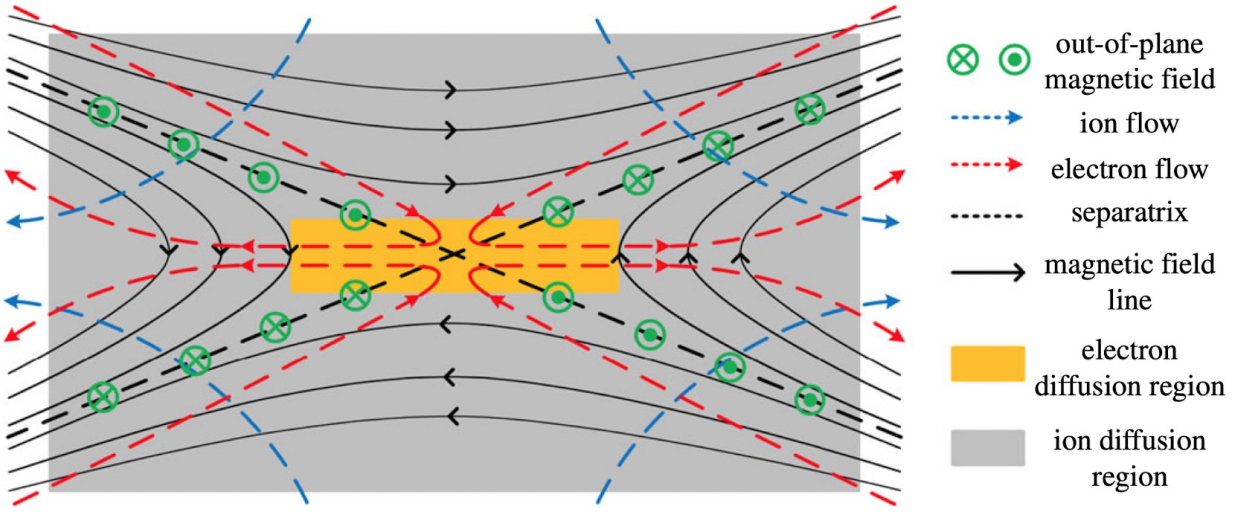

Figure 1.4: Hall magnetic reconnection arises in the ion diffusion region (grey area), where ions decouple from the magnetic field while electrons remain frozen-in as they move toward the electron diffusion region (yellow area). This decoupling creates field aligned currents that generate a characteristic quadrupolar out-of-plane magnetic field. These dynamics facilitate the onset of fast reconnection by reducing the aspect ratio of the diffusion region relative to the Sweet–Parker model. The resulting out-of-plane fields (green), produced by the differential motion of electrons (red dash line) and ions (blue dash line), allow the outflow region to expand, thereby enabling magnetic flux (black lines) to be transported through the reconnection site more efficiently. Figure taken from ref. [105]

the solar corona or the Earth's magnetopause. Although this model does not provide a complete description of magnetic reconnection, it establishes a useful starting point that many models are built on. As such, the definition of the normalized reconnection rate, reconnection magnetic field, and reconnection electric field are used throughout this thesis.

1.2.5 Hall Reconnection

For the Hall term, $\mathbf{J} \times \mathbf{B}/ne$, in the GOL (Eq. 1.13) to be dominate, two conditions must be satisfied. First, $\lambda_{mfp} > d_i$, where λ_{mfp} is the electron–ion mean free path and $d_i = c/\omega_{pi}$ is the ion inertial length. When this condition is met, Coulomb collisions are too weak to enforce $\mathbf{u_i} \approx \mathbf{u_e}$, allowing the electron and ion fluids to decouple such that two-fluid effects are important. Second, the width of the current layer must be on the order of or smaller than d_i. At this scale, the ions are prevented from following the $\mathbf{E} \times \mathbf{B}$ drift due to

their inertia, thereby breaking the ion frozen-in condition. With both conditions satisfied, the bottleneck imposed by the high-aspect-ratio Sweet–Parker current sheet is removed for the ion fluid, enabling inflow velocities on the order of $0.1\,v_A$, a regime known as fast reconnection. It is important to note that in this regime the hierarchy of fluid equations is typically closed by imposing a scalar pressure, $p = nT$.

The hall field configuration that supports these plasma dynamics is illustrated in Fig. 1.4. Within the ion diffusion region (grey area), where the ion momentum breaks the frozen-in condition, the ion flow paths (blue dashed line) are shorter compared to the electrons (red dashed line). In contrast, electrons remain magnetized due to their lower inertia, following field lines until they reach the electron diffusion region (yellow area). This difference in flow velocity generates a field aligned current, known as Hall currents, inducing an out of plane quadrupolar magnetic field (green circled cross and dot) [19]. The Hall effect transports magnetic flux through the diffusion region more efficiently, eliminating the reconnection rate's dependence on the Lundquist number and yielding $v_{in}/v_{out} \sim 0.1$ [47].

1.2.6 Collisionless Kinetic Regime

Similar to Hall reconnection, kinetic-scale dynamics arise when the width of the current layer is on the order of the ion inertial length. At this scale, the kinetic regime becomes dominant when the transit time of an electron fluid element across the diffusion region is shorter than the electron–ion collision time, τ_{ei}. Approximating the transit time as d_i/v_{out}, with $v_{out} \sim 0.1\,v_A$, the condition can be expressed as

$$\tau_{ei} > \frac{d_i}{0.1\,v_A}. \tag{1.38}$$

For typical laboratory plasmas, τ_{ei} is on the order of 10^{-6} s. When this condition is satisfied, the electron velocity distribution becomes anisotropic in the ion diffusion region (IDR), as illustrated in Fig. 1.5(a,b), and pressure anisotropy plays a dominant role in

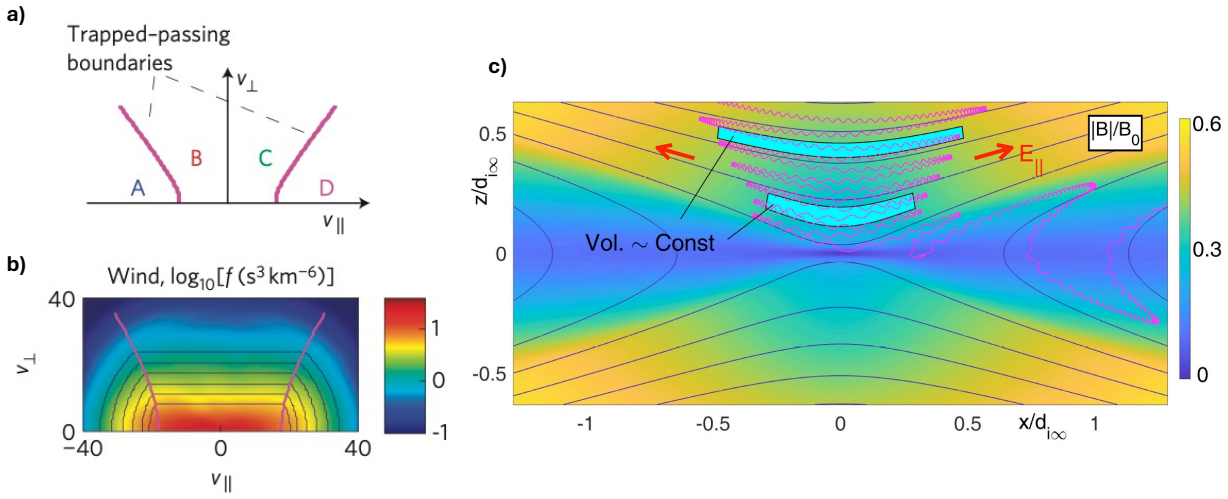

Figure 1.5: An overview of electron dynamics in the collisionless kinetic regime. Panels (a) and (b) are the electron velocity distribution, measured in the Earth magnetotail by the Wind space craft, where (a) defines the trapped passing population and (b) demonstrates the anisotropic shape of the distribution (Adapted from Ref. [23]). A trapped electron's path (red line) through the ion diffusion region (IDR) is shown in panel (d). In this region, the flux tubes (cyan region) are distorted as they near the electron diffusion region, causing the formation of $E_{||}$. Figure adapted from ref. [26]

the reconnection dynamics. In this regime, the pressure tensor is often approximated as gyrotropic near the boundary between the IDR and electron diffusion regions (EDR), and takes the form $\mathbb{P} = p_\perp \mathbf{I} + (p_{||} - p_\perp)\,\hat{\mathbf{b}}\hat{\mathbf{b}}$ [50]. These diagonal terms capture the effects of pressure anisotropy but do not directly contribute to breaking the frozen-in condition, in contrast to the off-diagonal components, which help balance the inductive electric field.

The pressure anisotropy in the kinetic regime arises from the expansion of magnetic flux tubes as they convect toward the electron diffusion region (EDR) with an $\mathbf{E} \times \mathbf{B}$ drift velocity. This process is illustrated in Fig. 1.5(c), where the cyan regions indicate that the flux-tube cross-sectional area scales as $A \propto 1/B$ due to magnetic flux conservation [25]. As in Hall reconnection, when the scale length falls below the ion inertial length d_i, the ions decouple from the flux-tube motion, while the electrons remain magnetized and continue to follow the expanding flux tubes. In response to the resulting charge separation, a parallel acceleration potential develops to maintain quasi-neutrality by drawing electrons into

regions of reduced electron density. This potential represents the work done by the parallel electric field $E_{||}$ on electrons streaming along magnetic field lines, and is defined as

$$\Phi_{||}(x) = \int_{x}^{\infty} E_{||}\, dl, \tag{1.39}$$

where the integration is performed along a magnetic field line from position x to the ambient plasma. From this definition, the gradient of $\Phi_{||}$ perpendicular to the magnetic field has no physical significance, and is therefore referred to as a pseudo-potential [25].

The parallel electric field both accelerates and traps electrons near the X-point, producing the trapped orbits illustrated in Fig. 1.5(c) and the anisotropic velocity distributions shown in Fig. 1.5(a, b). These features arise primarily from the parallel acceleration, with a smaller contribution from the reduction in perpendicular energy caused by the decreasing magnetic field strength near the X-point. This characteristic anisotropic velocity distribution has been directly observed by multiple spacecraft missions, including *Wind*, *Cluster*, *THEMIS*, and *MMS*. A representative example from the first *Wind* observations in 1999 [28] is shown in Fig. 1.5(c).

Developing a comprehensive description of the plasma dynamics within the kinetic regime has been a focus of the TREX research group, where the combination of spacecraft and laboratory data has guided an evolving theoretical model [25, 50, 27, 52, 62, 26]. The resulting equations of state (EoS), Lê 2009 EoS , developed for a collisionless plasma with a weak to moderate guide field, are based on a drift kinetic model derived from a gyro-average of the Vlasov equation for magnetized electrons. This analysis takes into account the double adiabatic particle trapping from $\Phi_{||}$ and the mirror force $-\mu\nabla_{||}B$. The fluid closure resulting from this work defines a pressure tensor term within the GOL that asymptotically approaches both the isotropic scalar pressure in the Hall regime and the Chew-Goldberger-Low (CGL) diagonal pressure tensor terms necessary for the kinetic regime.

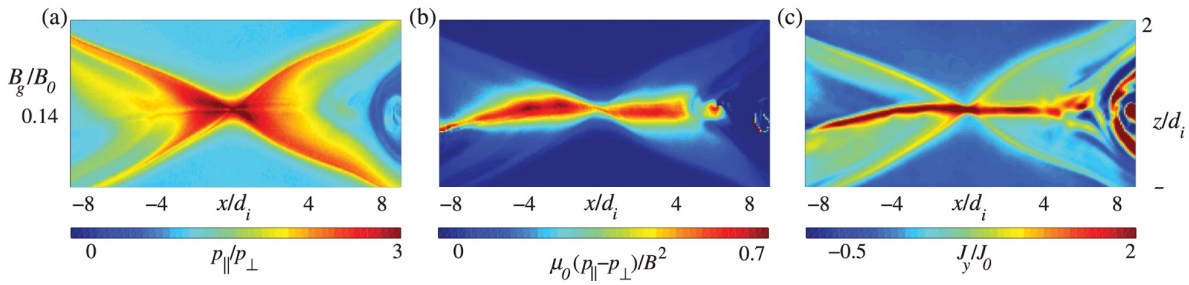

Figure 1.6: A fully collisionless simulation with a guide field of $B_g = 0.14B_0$ illustrating pressure and current dynamics in the IDR of the Kinetic regime. Pressure anisotropy develops in the outflow region of panel (a), where $p_{||} > p_{\perp}$. Panel (b) shows where the marginal firehose condition is satisfied. The characteristic out-of-plane current that extend multiple d_i outside the EDR. The current develops in response to the pressure anisotropy, such that force balance is satisfied. Figure adapted from ref. [52]

A distinguishing characteristic of the kinetic regime is the possibility of forming an out of plane current that extends multiple d_i from the EDR, driven by the upstream pressure anisotropy within the IDR, as shown in Fig. 1.6(c). The necessity of the current is seen by examining equation 1.11 for a steady state collisionless plasma in the EDR, which gives

$$ne\mathbf{E} = \mathbf{J}_{\perp} \times \mathbf{B} - \nabla \cdot \mathbb{P}, \tag{1.40}$$

where the inertia term is small as shown in PIC simulations [52] and $\mathbf{J}_{\perp} = \mathbf{J_e} = -ne\mathbf{u_e} \approx \mathbf{J}$ due to the electrons carrying 90% of the current [49]. For typical kinetic regime reconnection values, $|\mathbf{E}| = E_{rec} = 0.1v_A B$ is small compared to $\nabla \cdot \mathbb{P}/ne \approx v_{th,e}B$ [49], reducing the force balance relation to

$$\mathbf{J} \times \mathbf{B} - \nabla \cdot \mathbb{P} = 0. \tag{1.41}$$

The first term is the magnetic portion of the divergence of the Maxwell stress tensor, $\mathbf{J} \times \mathbf{B} = 1/\mu_0(\nabla \mathbf{BB} - (\nabla B^2/2)\mathbb{I}) = \nabla \cdot \mathbb{T}$, and the second term is given by the upstream pressure tensor defined in Le$\hat{2}$009 EoS. It then follows from momentum balance that a current density forms, $\mathbf{J}_{\perp} \sim (p_{||} - p_{\perp})\mathbf{B} \times (\mathbf{b} \cdot \nabla \mathbf{b})/B^2$, which increases as the marginal firehose condition is approached, $p_{||} - p_{\perp} \approx B^2/\mu_0$. Fig. 1.6(a–c) show a representative

example of the out of plane current (c) that forms when the firehose condition (b) and the necessary pressure anisotropy (a) exist in the presence of a guide field.

Further simulation analysis has examined the effects of density asymmetry across the reconnection current layer, as well as how the presence of a guide field (or component field) modifies the reconnection dynamics [52, 63]. Ongoing work in the TREX group aims to observe these effects with the Drive Cylinder experiment, described in the following chapter, which has the capability of accessing kinetic-scale physics.

1.3 3D Magnet Reconnection

While 2D models provide valuable insight, many natural and laboratory plasmas exhibit magnetic configurations that are inherently 3D. In these more complex geometries, a method for analyzing these systems is describing them in terms of their magnetic *skeletal structure* [83], illustrated in Fig. 1.7(a). The skeletal structure is built upon the topology of magnetic null points that have the following features [33, 46, 74]:

- A point in space where $\mathbf{B} = 0$.
- Because $\nabla \cdot \mathbf{B} = 0$, null points are necessarily hyperbolic.
- The *spine* is a pair of field lines that asymptotically approach or recede from the null point along a single axis. In Fig. 1.7(b), the spine is formed by the bundle of field lines parallel to the z-axis.
- The *fan* consists of a surface of field lines that spread out from or converge toward the null point. The field lines in the x-y plane form the fan in Fig. 1.7(b).
- *Separatrix* surfaces are formed by fan field lines as they extend away from the null. These surfaces partition space into topologically distinct flux domains.
- Nulls form together in a positive-negative pair to conserve the topological degree [36], with the intersection of their fans linking them, as shown in Fig 1.7(c). A *positive null*

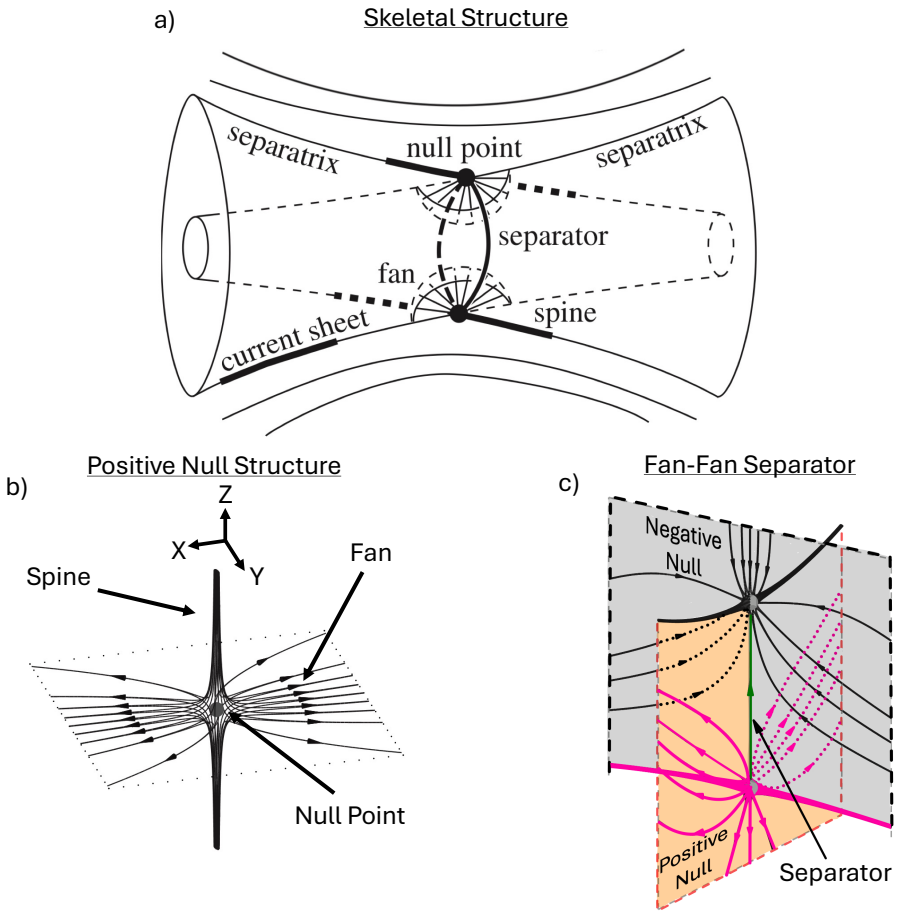

Figure 1.7: Panel (a) is a generic topological or skeletal structure that is used to define many complex magnetic toplogies. Panel (b) is a positive radial null point characterized by the fan field lines spreading outward from the null point, and (c) a standard two null fan-fan separator. In panel (c), the intersection of the separatrix surfaces forms the separator line connecting the positive (magenta lines) and negative (black lines) null points. Figures adapted from [84]

has fan field lines that diverge from the null, while in a *negative null* the fan field lines converge toward it.

- *Separators*, or X-lines, are special field lines that connect pairs of null points. They form at the transverse intersections of separatrix surfaces (fans) [83], as shown Fig. 1.7(b,c).

Extending the null features beyond a local spacial volume provides a detailed description of the magnetic topology of the system. Through this approach, the skeletal structure for a mini-magnetosphere was identified, enabling direct observation of the evolution of its

magnetic topology.

1.3.1 Distinguishing Between 2D and 3D Reconnection

In the most general sense, 3D reconnection is defined as occurring within a localized non-ideal region along magnetic field lines wherever $E_{||} \neq 0$ [88, 40], where $E_{||}$ denotes the component of the electric field parallel to the magnetic field. This broad definition encompasses both diffusion and field-line slippage, processes that are often excluded from narrower discussions of reconnection. In certain cases, however, the magnetic field-line mapping between two boundaries becomes singular, meaning that neighboring field lines experience a discontinuous change in connectivity across a specific line passing through the non-ideal region. This allows for a more restrictive definition of reconnection, known as *singular field-line reconnection* [81, 41, 82, 78], which is characterized by the topology of the magnetic field in a plane perpendicular to $E_{||}$.

If the transverse magnetic topology is X-type, the process is termed *X-type singular reconnection*, which closely resembles 2D reconnection and typically occurs along magnetic separators. Conversely, if the transverse topology is O-type, it is referred to as *O-type singular reconnection*, encompassing flux-tube disconnection [99] and certain forms of separator reconnection observed in numerical simulations [73]. This framework is applied in Chapter 3, where planes perpendicular to the separator exhibit an X-type magnetic configuration, thereby justifying the 2D reconnection analysis employed.

1.4 Thesis Outline

A long-standing goal of the Terrestrial Reconnection EXperiment (TREX) group has been to access the kinetic regime of magnetic reconnection. In this regime, the dynamics are governed by the electron fluid traversing the diffusion region on timescales shorter than the electron–ion collision time. The first part of this thesis describes the successful imple-

mentation of a TREX design that reached this milestone. Though kinetic dynamics have been observed, attaining diagnostic measurements capable of fully resolving many relevant plasma characteristics have remained challenging. With this limitation in mind, two exploratory experiments were conducted with varying levels of success. The first, described in section 2.5, sought to merge magnetic islands in order to enhance Fermi heating, which is a particle acceleration process known to occur during reconnection. While island merging was observed, the effect could not be reproduced consistently. The second experiment, described in section 2.6, investigated diamagnetic suppression of the reconnection rate. This study was considerably more successful, though further investigation is required to confirm and extend the results.

The second section, beginning in Chapter 3, investigates 3D reconnection within a mini-magnetopause. This study examines the complex magnetic geometry observed from a volumetric scan of a mini-magnetosphere, where the system size is less than the ion inertial length. By systematically characterizing the topology, the initiation of fast reconnection was linked to a topological change in the underlying magnetic skeletal structure. To our knowledge, this represents the first observation of such a trigger mechanism for fast magnetic reconnection.

2 IMPLEMENTATION OF A DRIVE CYLINDER FOR LOW COLLISIONAL EXPERIMENTS ON MAGNETIC RECONNECTION

Can a terrestrial plasma fluid element be driven through the diffusion region at a comparable timescale to the electron-ion collision time? Is it possible to create a uniform anti-parallel field configuration within a cylindrical system? Are the dynamics within this system robust and reproducible?

This chapter is a reprint from an RSI manuscript of the same title [35]. Section 2.5 and beyond describe improvements and experiments that were not covered in the published paper.

2.1 Introduction

Magnetic reconnection is a ubiquitous process that can occur in many astrophysical and laboratory settings [105]. It is a topological rearrangement of magnetic field lines in a plasma, leading to the release of stored energy through the conversion of magnetic energy into particle kinetic energy, thermal energy, and kinetic energy of large scale flow of plasma [98]. Magnetic reconnection is crucial in understanding various space physics phenomena, such as solar flares, coronal mass ejections, and magnetospheric dynamics [59, 10, 77, 21]. Moreover, it plays a significant role in laboratory plasma experiments that aim to study fundamental plasma physics and fusion energy [96].

Characteristics of reconnection are sensitive to a range of parameters including the local properties of the plasma as well as the size of the system in which the process occurs. In laboratory experiments, for example, the plasma density is often relatively large such that the time scale τ_{ei}, characterizing electron and ion Coulomb collision times, becomes shorter or comparable to the time scale governing the reconnection process. Coulomb collisions effectively smooth out structures in the electron velocity distributions, and for typical

laboratory experiments the electrons are usually well characterized as near-Maxwellian. The properties of the electron fluid (including viscosity and resistivity) may then be approximated by the Braginskii equations [6]. Meanwhile, in tenuous space plasma, τ_{ei} is often much longer than the time scale of reconnection. This situation then yields a kinetic regime where the electron distribution can develop strong pressure anisotropy, an important characteristic in the reconnection process [27, 26].

The shear angle [64] between the reconnecting magnetic field lines is another important parameter. The regime of low shear angle, also known as guide-field reconnection (or component reconnection), is relevant to saw-tooth relaxation events observed in magnetic confinement fusion devices [102]. The guide magnetic field, B_g, perpendicular to the reconnecting magnetic field, B_{rec}, here dominates $B_g/B_{rec} \gg 1$ and the size of the reconnection region is predicted by reconnection fluid models [45] to be on the order of the ion-sound-Larmor radius $\rho_s = \sqrt{2m_i(T_e + T_i)}/(eB_g)$, where T_e and T_i are the electron and ion temperatures, m_e is the electron mass, and e is the positive electron charge. Reconnection in space and magnetospheric plasma are typically characterized by a low-to-moderate guide field regime where $B_g/B_{rec} \lesssim 1$, and for this regime a typical length scale of the reconnection region is the ion-inertial-length $d_i = c/\omega_{pi} = \sqrt{m_i/(nq_i^2\mu_0)}$. Here ω_{pi} is the ion plasma frequency, m_i is the ion mass, n is the plasma density, and q_i is the ion charge. Ideally, laboratory experiments on reconnection should have system sizes much larger than d_i, such that the process is less affected by the boundary conditions.

2.1.1 Reconnection Phase Diagram

The phase diagram for reconnection [43, 13] is a useful tool for summarizing our current understanding of this process under various plasma conditions. The diagram was augmented in Ref. 51 to distinguish between the kinetic collisionless and Braginskii regimes previously discussed. A version of this diagram is shown in Fig. 2.1, which is spanned by the system size normalized to the ion-inertial-length, $\lambda = L/d_i$, and the dimensionless

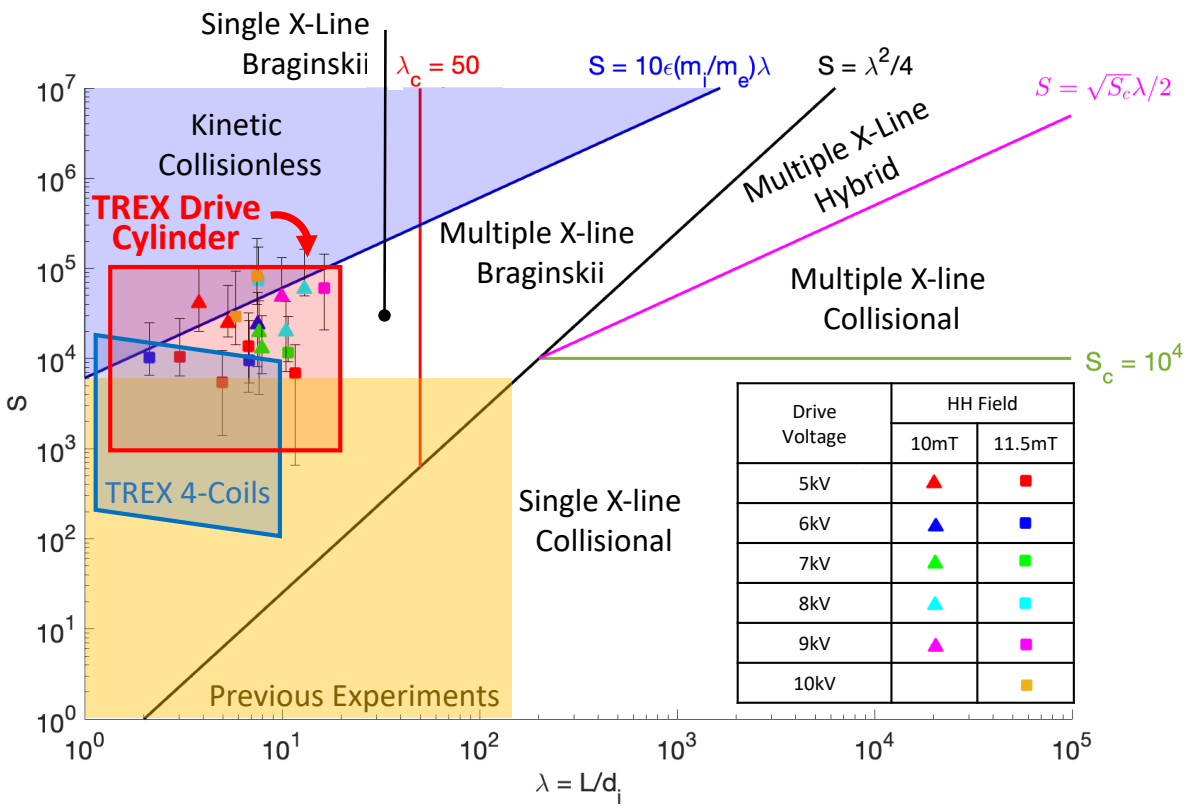

Figure 2.1: Phase diagram [43, 13, 51, 44] showing the different regimes of magnetic reconnection. Data points from a voltage scan with the Drive Cylinder are displayed in the shaded red region. Each data point represents a single discharge event, corresponding to a specific combination of the magnitude of the Helmholtz (HH) field and the magnitude of the discharged voltage of the capacitor bank (Drive Voltage). The location of each point is calculated using Langmuir and $\dot{B}$ probes, which measure T_e, n, and B_{rec}. The varied error range is due to the level of uncertainty in acquiring T_e and n data near the reconnection current sheet.

Lundquist number

$$S = \frac{\mu_0 v_A L_{cs}}{\eta}. \tag{2.1}$$

Here S is defined as the ratio of the Alfvén wave crossing time to a resistive diffusion time scale for a typical length scale L_{cs}. In Eq. 2.1, $L_{cs} \approx$ 1m is the half-length of the reconnecting current sheet and can be taken as $L_{cs} = \epsilon L$, where $L = 3/2$m is the half-length of the system size, which sets $\epsilon = 2/3$ for the Drive Cylinder [43]. $\eta = m_e/(ne^2\tau_{ei})$ is the plasma resistivity and $v_A = B_{rec}/\sqrt{\mu_0 m_i n}$ is the Alfvén velocity.

Within the Braginskii regime, the ions and electrons are not coupled by collisions

n	1×10^{17} – 3×10^{18} m^{-3}
T_e	3 – 80 eV
T_i	$\sim$ 3 eV
B_{rec}	1 – 10 mT
E_{rec}	0 – 900 V/m

Table 2.1: These plasma parameters for the Drive Cylinder were measured using a 16 tip biased Langmuir probe for T_e and n, and a linear array of $\dot{B}$ probes for B_{rec} and E_{rec}; these probes are described in Ref. 70. T_i is estimated based on the plasma source; there is no direct measurement of T_i. B_{rec} is calculated using the reduced magnetic field for asymmetric reconnection [9].

and two-fluid effects are here important. Meanwhile, the electron distribution function is still relaxed by collisions and remains a near Maxwellian without the development of significant pressure anisotropy. In contrast, investigating the kinetic collisionless regime, where pressure anisotropy becomes dominant requires the much more stringent condition that the time for the plasma to convect through the inflow region ($\tau_c \approx d_i/(0.1v_a)$) satisfy the condition [51]

$$\tau_c < \tau_{ei}. \tag{2.2}$$

Here the left-hand-side represents a typical time scale for a fluid element in the reconnection inflow to travel a distance of $1d_i$, where the inflow speed is $0.1v_A$. When this typical time is less than the electron-ion collision time τ_{ei}, the reconnection process is in the kinetic regime. Eq. 2.2 can be written in terms of the parameters spanning the phase diagram, which gives $S > 10\epsilon(m_i/m_e)\lambda$, and is plotted in Fig. 2.1. A goal of the Terrestrial Reconnection EXperiement (TREX) [68], developed within the Wisconsin Plasma Physics Laboratory (WIPPL) [32], is to explore reconnection at conditions relevant to the Earth's magnetosphere. In particular, a focus of TREX is to reach the collisionless regime where electron pressure anisotropy can develop unimpeded by Coulomb collisions. Table 2.1 lists the plasma parameters the Drive Cylinder is able to attain, which lie in the necessary range to reach the kinetic regime.

In addition to reaching the milestone of satisfying Eq. 2.2, it is also desirable to operate

at a system size on the order of $\lambda \simeq 10$, allowing the ion fluid to partake in the reconnection process [97]. These conditions are achieved by driving the plasma with a large reconnection electric field E_{rec}, maximizing the rate by which magnetic flux is forced through the reconnection region. In conjunction, increasing the length of the reconnection current layer L_{cs} will directly increase S, as seen in Eq. 2.1. The relative position of TREX in the reconnection phase diagram is plotted in Fig. 2.1. Using the Drive Cylinder, coordinates (λ, S) are plotted from multiple plasma discharges, and the shaded red region represents the theoretical upper and lower limits of possible Drive Cylinder (λ, S) values. Both the shaded area and values based on measurements extend into the region defined by Eq. 2.2. This corresponds to an increase in both S and E_{rec} from the previous TREX configuration (shown in the shaded blue region in Fig. 2.1); the methods by which these improvements were achieved will be discussed in Sections 2.2.1 and 2.2.2, respectively.

2.2 Drive Cylinder Design

The Drive Cylinder, shown in Fig. 2.2(a,3), expands upon the 4-coil setup [70] by elongating the system with 12 drive coils and introducing a cylinder constructed from electrically isolated sheets of aluminum. In the new configuration, both coils and cylinder have a radius of 0.6m. The design of this system is in part informed by the original TREX setup, which consisted of 3 to 4 single loop coils, resulting in normalized reconnection rates between $\alpha = E_{rec}/(v_A B_{rec}) \approx 0.1$ to 0.5 and a Lundquist of $S \approx 10^3$ to 10^4. Here, B_{rec} is the magnetic field upstream of the reconnection layer [70, 37].

In Fig. 2.3 a cartoon is given for the magnetic field geometry produced when plasma is present. This field configuration is generated from the combination of a steady Helmholtz (HH) field and a rapid energization of the Drive Cylinder. In this plot, the coloring of the flux contours distinguishes between regions of magnetic fields relative to the reconnection current layer. The Drive Cylinder field lines, shown in yellow, are upstream of the recon-

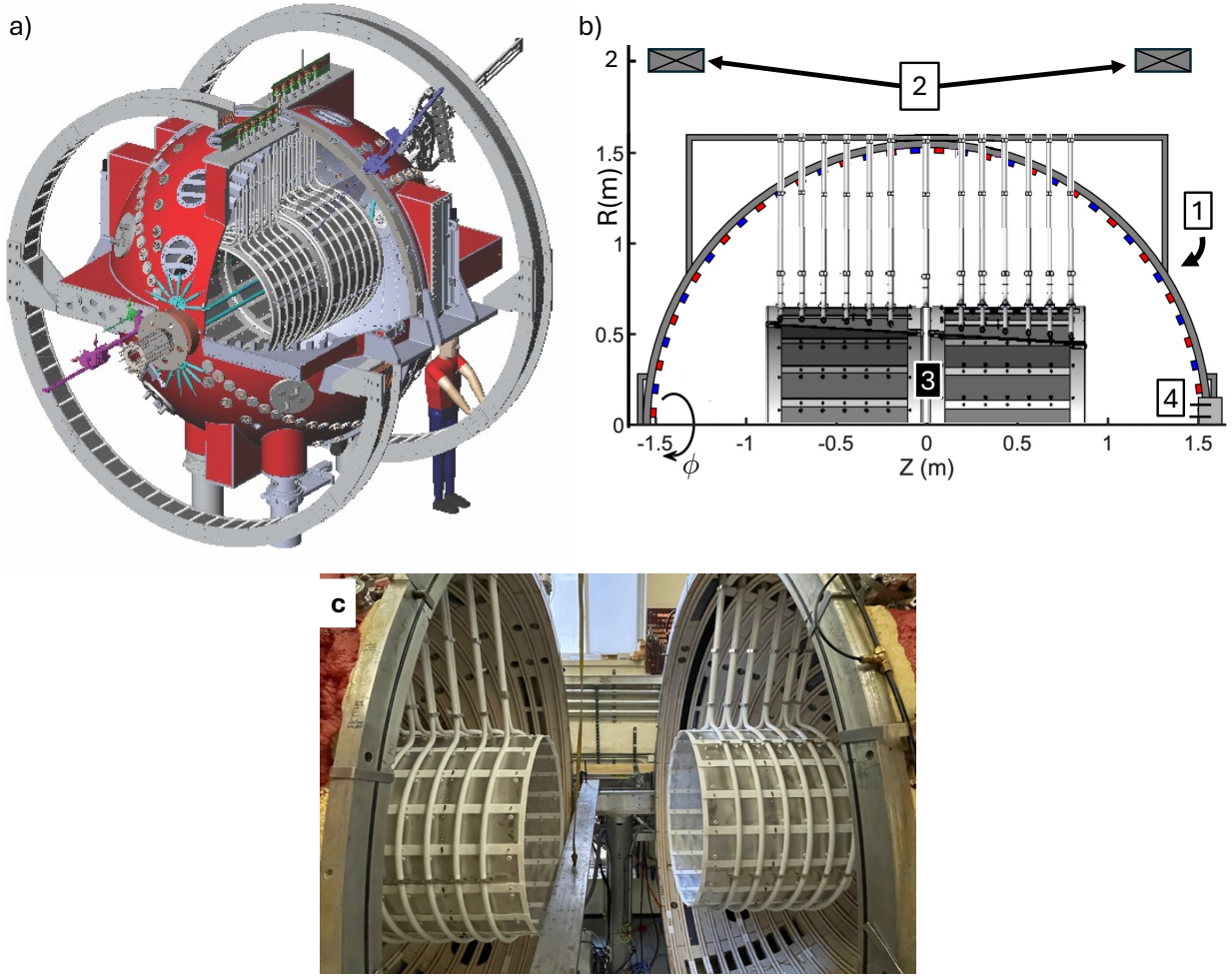

Figure 2.2: Panels (a) and (b) are CAD renders of the TREX Drive Cylinder inside the BRB vacuum vessel, where (b) is a slice of the cylindrically symmetric system shown in (a). The primary hardware components used are (1) BRB 3 m vacuum vessel, (2) 4 m Helmholtz (HH) coil, (3) Drive Cylinder coil system, and (4) plasma washer guns. (c) is an image of the Drive Cylinder installed in BRB, where the white drive coils and cylindrical shell are visible.

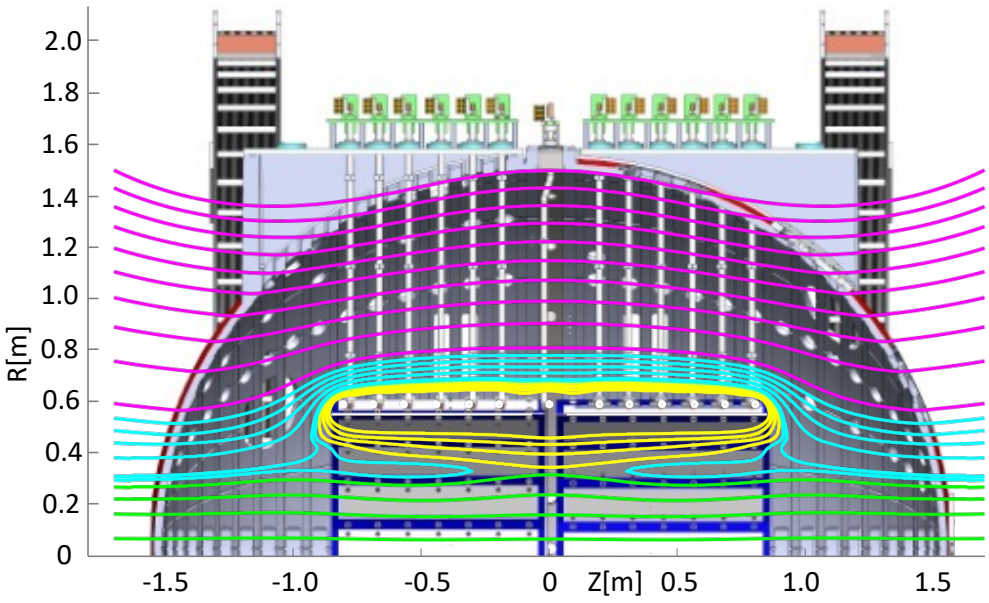

Figure 2.3: 3D render of the experimental setup overlayed by TREX's theoretical magnetic geometry in the presence of plasma. The contour colors differentiate the regions of flux relative to the reconnection current layer. Yellow is the flux from the Drive Cylinder upstream of the current layer and green is the HH field in the interior of the Drive Cylinder (also upstream of the reconnection layer). The magenta field lines are the HH field exterior of the Drive Cylinder, which do not participate in the reconnection process. Lastly, cyan is the reconnected field downstream of the reconnection layer.

nection current sheet, and the green fields lines designate the HH field in the interior of the Drive Cylinder, which are also upstream of the reconnection layer and anti-parallel to the yellow Drive Cylinder field lines. The cyan region are the reconnected field lines downstream of the reconnection current sheet, and lastly the magenta lines represent the magnetic flux of the HH coils that does do not participate in reconnection. These lines initially begin exterior and remain exterior to the cylinder during the full reconnection cycle.

A circuit diagram of the Drive Cylinder and pulsed power supply is shown in Fig. 2.4(a). This system allows the current to peak in ~12μs, which can be seen in the time trace of the measured vacuum B_z plot shown in Fig. 2.4(b). The time trace of the magnetic field is indicative of the current through the drive coils due to the relationship $B \propto I$, which is a result of Ampère's Law. Fig. 2.4(b) is the time integrated plot from a $\dot{B}$ probe located at R

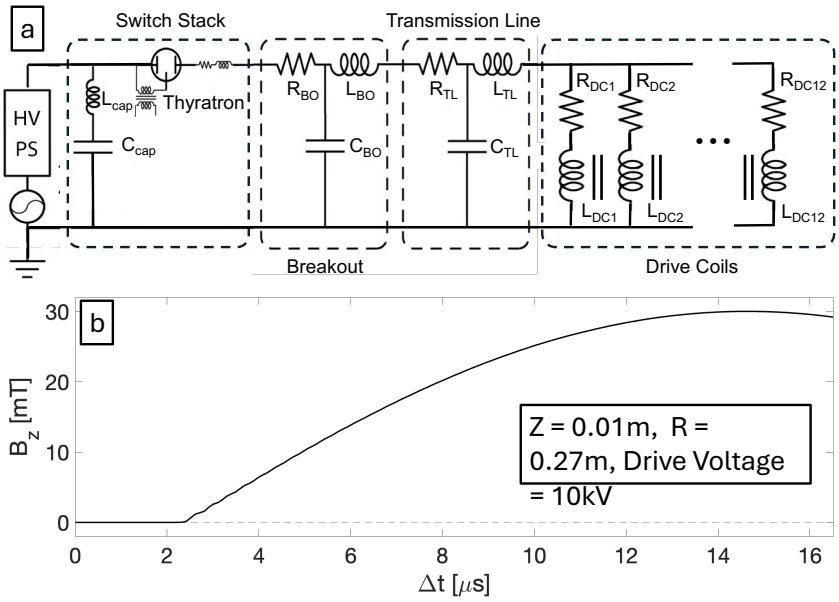

Figure 2.4: (a) is a circuit diagram of the pulsed power supply and Drive Cylinder system. The pulsed power supply capacitor bank consists of 5 $\times$14μF capacitors such that $C_{cap} =$ 70μF with an inductance of $L_{cap} =$ 20nH. The Drive Cylinder is modeled as 12 inductively connected drive coils with an equivalent inductance of $L_{DC} =$ 445nH. Plot (b) is a time trace of the vacuum B_z field measured with a $\dot{B}$ probe. Since $B \propto I$, the induced current profile applied to the Drive Cylinder can be inferred, showing the peak current occurs in ~12μs, which corresponds to when B_z is maximum.

= 0.27m and Z = 0.01m with the drive voltage set to 10kV. The ability of the Drive Cylinder system to generate this rapid rise in B_z is a primary reason the collisionless kinetic regime is reached.

2.2.1 Extending L_{cs} and Forming a Uniform Magnetic Field

The system size of the Drive Cylinder was increased by extending the distance spanned by the 12 drive coils, resulting in a current sheet twice the length of the 4-coil setup. Beyond this, the addition of the cylindrical shell has a twofold effect. First, the shell reduces the "private flux" from the individual coils, which increases the efficiency of the Drive Cylinder; this is further discussed in Section 2.2.2. Second, a uniform field is generated inside the Drive Cylinder parallel to the Z-axis, allowing the reconnection current sheet to develop from a more uniform magnetic geometry. These design features form the field configuration

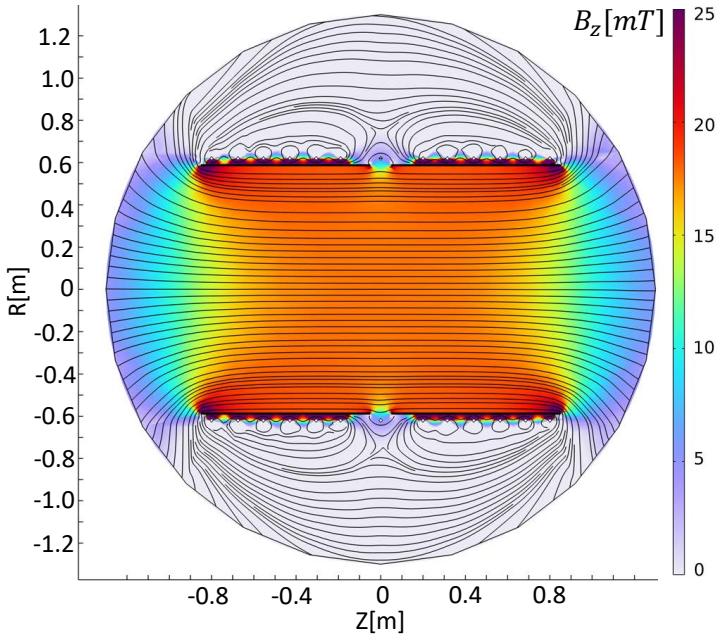

Figure 2.5: A COMSOL model of the B_z vacuum field in the RZ plane overlayed with toroidal flux contours.

shown in Fig. 2.5, where the B_z vacuum field generated by the Drive Cylinder is plotted using COMSOL. COMSOL is a finite-element solver that uses Maxwell's equations, in conjunction with the Drive Cylinder's 3D CAD renders and material properties, to generate 3D models of the vacuum magnetic and electric fields. The effectiveness of shielding B_r is demonstrated in Fig. 2.6, also a COMSOL render, which shows a minimal presence of B_r in the region $r < R_{cyl}$, where R_{cyl} is the radius of the Drive Cylinder. For generating these fields the cylinder was made from 20 electrically isolated sheets of aluminum, as shown in Fig. 2.7.

To illustrate the design motivation for separate sheets of aluminum, a hypothetical Drive Cylinder consisting of a continuous aluminum cylinder with no cuts and 12 drive coils is examined. Due to the component of the electric field parallel to the surface of the continuous cylinder vanishing, it is clear that V_{loop} for any path around the cylinder must also vanish. It then follows directly from Faraday's law that at short time scales (were the resistivity of aluminum can be ignored), any rapid change in the B_z magnetic fields is

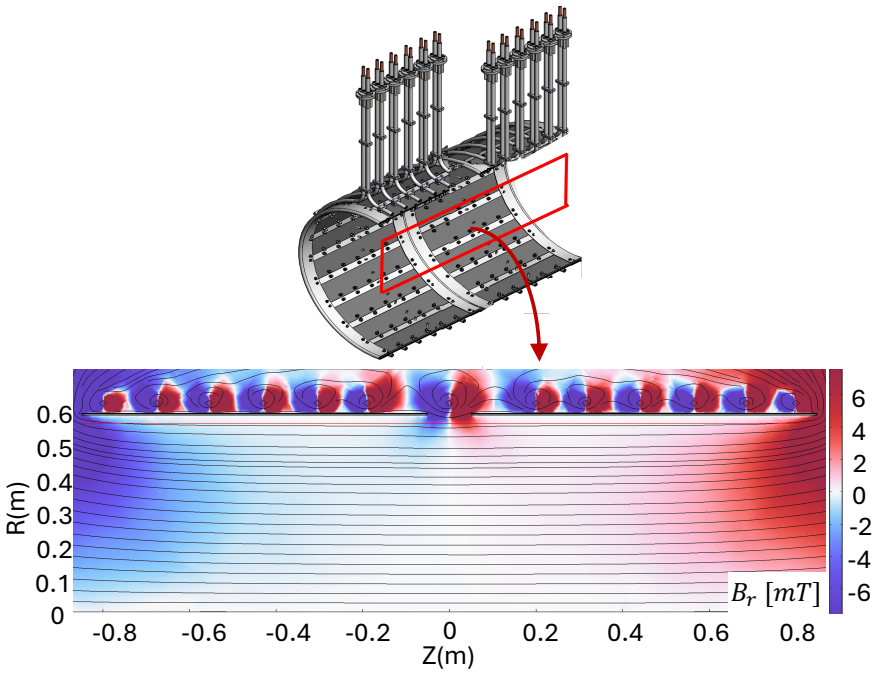

Figure 2.6: B_r vacuum fields modeled using COMSOL in the region indicated in the 3D render. The effective shielding of B_r is evident in the interior of the Drive Cylinder where, $R < 0.6$m.

shielded from entering the interior of the cylinder. Similarly, rapid changes in B_r are also blocked.

To allow B_z to pass unimpeded while continuing to shield B_r, the hypothetical cylinder can be cut along the surface parallel to the Z-axis. Using the same reasoning as the continuous cylinder, B_r remains shielded by the conducting aluminum sheet. Meanwhile, the cut in the cylinder strongly affects B_z. This can be analyzed using an Ampèrian loop in the RZ plane, which gives

$$\oint B_z \, dz = \mu_0 \iint [J_{coils} + \delta(r - R_{cyl}) K_{cyl}] \, dr \, dz, \tag{2.3}$$

where the closed loop path is chosen such that the B_r portion is small. In Eq. 2.3 the enclosed currents J_{coils} and K_{cyl} are from the drive coils and induced surface current on the cylinder, respectively. An illustration of these currents is shown in Fig. 2.8. With the cut cylinder being a single sheet with its ends overlapping, one row of eddy currents

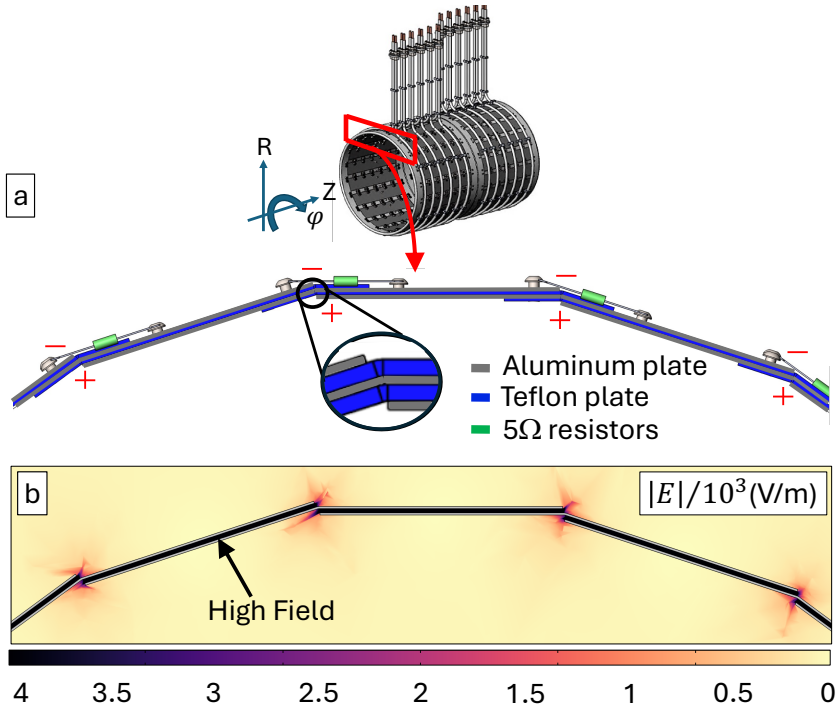

Figure 2.7: (a) is a section of the cylinder showing the separate sheets of aluminum (grey) and Teflon (blue). Resistors, shown in green, are used to evenly distribute the potential difference that builds up between the plates (near the $\pm$ signs) over the circumference of the cylinder. This voltage difference is evident in (b) where a COMSOL render of |E| is plotted in the same region as (a). The color range is saturated between the plates of the Drive Cylinder, which is indicated by the high field label

shown in the side view of Fig. 2.8 will extend the circumference of the cylinder. Due to equal amounts of current flowing in the $\pm\hat{\phi}$ direction, $\int\int [\delta(r - R_{cyl})K_{cyl}]\ dr\ dz = 0$, which reduces Eq. 2.3 to $\oint B_z\ dz = \int\int J_{coils}\ dr\ dz$. Therefore, $\oint B_z\ dz$ is unaffected by the cylinder, hence the B_z component from J_{coils} must exist in the interior of the cylinder, $r < R_{cyl}$. In the same region, the spacial variations of B_z are related to B_r through $\nabla \cdot \mathbf{B} = 0$, and because B_r is shielded it follows that B_z must be roughly uniform. Therefore, the field induced by the drive coils, parallel to the surface of the cut cylinder, is effectively smoothed after passing through the discontinuous aluminum cylinder.

Improving upon the idea of a single cut altering the induced loop current, 20 insulated plates of aluminum were used to form the cylinder, which effectively divides the voltage be-

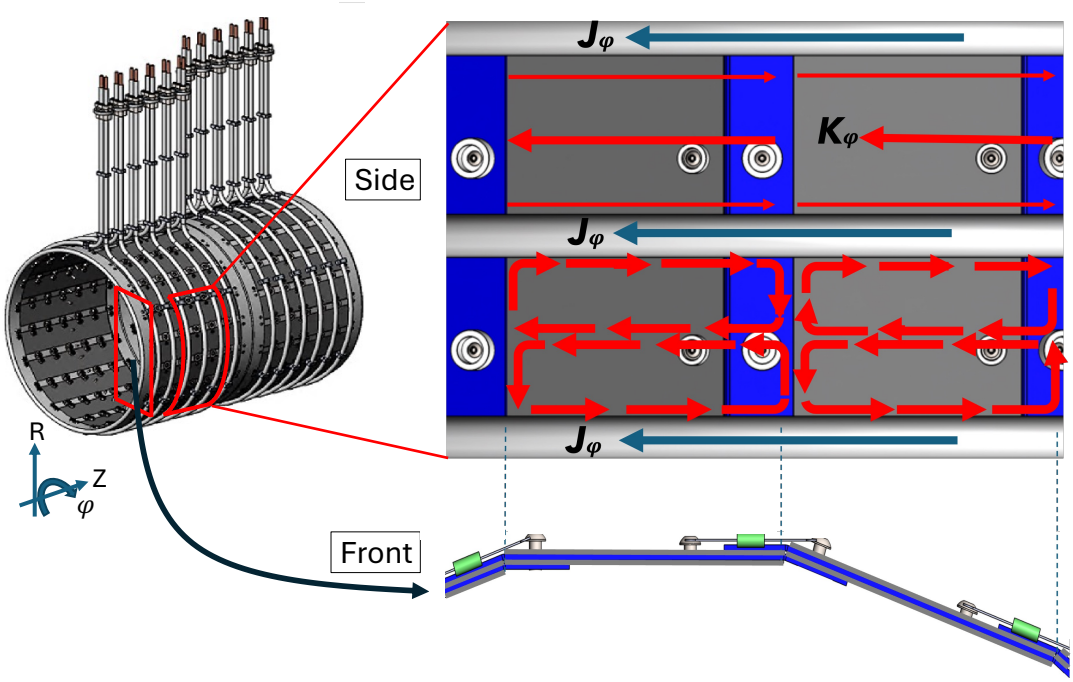

Figure 2.8: 3D CAD render of the Drive Cylinder showing the sheets of aluminum in the front view and the resulting discrete eddy currents that develop in the side view. An illustration of the eddy currents caused by the magnetic field of the drive coils are shown on the left portion of the side view with the resulting surface current K_ϕ illustrated on the right portion of the side view.

tween overlapping plates. This overlap is shown in Fig. 2.7(a), and illustrates the cylinder's ability to create a continuous surface shielding B_r, while still being composed of individual sheets. The primary purpose of dividing the voltage is to reduce the chance of arcing, which is accomplished without affecting the desired field configuration. The build-up of electric fields at the ends of each aluminum plate can be seen in Fig. 2.7(b), where $|E|$ is plotted using COMSOL. In an effort to evenly divide the induced voltage between the plates, a 5 Ω resistor was connected across each aluminum sheet. This resistance was chosen such that a maximum of 100 A of current could flow through the resistor during a 10 kV discharge. With this current being two orders of magnitude less than the current through the drive coils, the fields induced by the drive coils are unaffected while the voltage between each plate is evenly distributed between the 20 gaps.

The geometry of the individual aluminum plates, with a sketch of the eddy currents,

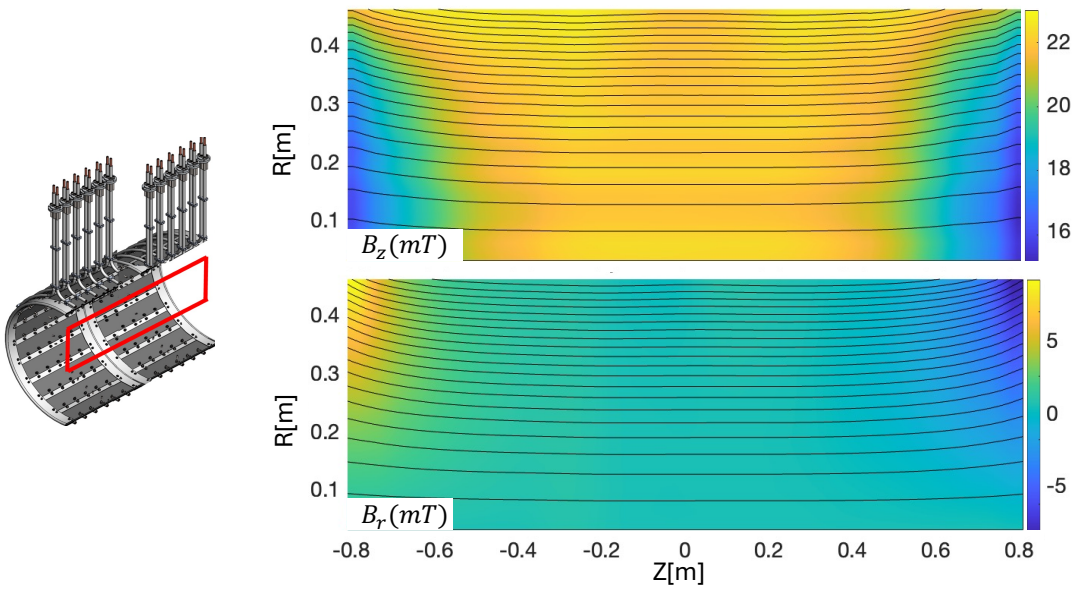

Figure 2.9: Measured vacuum fields from a $\dot{B}$ probe array with toroidal flux contours overlayed onto the B_z and B_r components of the field. The $\dot{B}$ probe array is parallel to the Z-axis, extends the length of the Drive Cylinder, and is fixed at a single radial coordinate value (this value can be changed between shots). Both plots where generated from 12 separate discharge events, each measured at a different radial position evenly spaced between $0 < R < 0.46$m.

is given in Fig. 2.8. The discrete surface current, K_ϕ, shown in the right portion of the side view of Fig. 2.8, arises from the superposition of the eddy current loops displayed on the left portion of the side view. From these discrete surface currents, Fig. 2.9 shows the measured vacuum fields for $0 < R < 0.46$m. These plots were recorded from a collection of 12 discharge events measured with a B-dot probe array that extends the length of the cylinder. For each discharge the probe array was positioned at a different radial location; the combination of these measurements produce Fig. 2.9.

The relevance of this magnetic field configuration to the time scale of the experiment was determined by calculating the resistive diffusion time through the aluminum plates of B_r using COMSOL. The results are shown in the top of Fig. 2.10, where five different Z locations along $R = 0.56$ m are examined. The diffusion of B_r at $R = 0.56$ m is shown in the pseudocolor plot in Fig. 2.10(a). Oscillation in the direction and strength of B_r is indicative of the coil field, shown in Fig. 2.6, diffusing through the aluminum sheets. The data at each

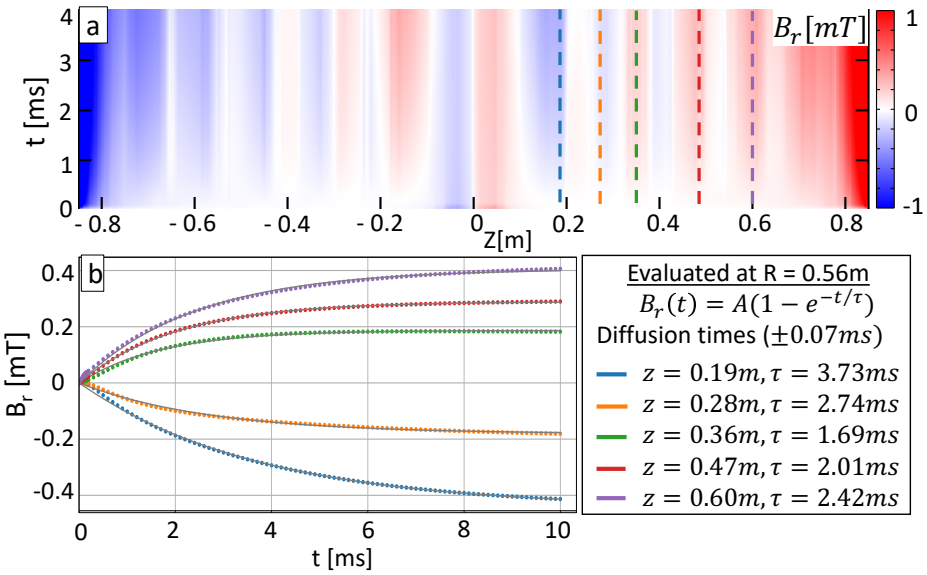

Figure 2.10: Plot (a) is a pseudocolor plot of $B_r(t, z)$ modeled from COMSOL at R = 0.56m. To determine the magnetic diffusion characteristics, a 10μs voltage pulse was applied to the drive coils with their conductivity set such that the current did not dissipate over 10ms. Plot (b) is exponential fits of B(t) at specific values of Z indicated in the legend for the associated diffusion times τ.

Z location was fit to an exponential curve, as shown in Fig. 2.10(b). The fits, listed in the legend of Fig. 2.10, give diffusion times between 3.7 ms and 1.7 ms. The variation in these times is attributed to differences in the current pattern induced in the aluminum plates, which can be understood as a superposition of variable sized eddies. Because the diffusion time scales like (eddy size)^2, the smaller eddies diffuse (dissipate) away much faster than the larger eddies, causing the variation shown in Fig. 2.10. The resulting diffusion time range is two orders of magnitude greater than the time scale of the reconnection process, demonstrating the Drive Cylinder effectively shields B_r for the duration of the experiment.

2.2.2 Driving Electron Fluid Through the Reconnection Region with Increased E_{rec}

To enhance the value of S and satisfy the condition set by Eq. 2.2, it is important to optimize the reconnection electric field, E_{rec}. With this in mind, a cylinder generates a higher

loop voltage than discrete coils, which is a primary motivation for the Drive Cylinder design. This feature is exemplified by comparing the efficiency V_{loop}/V_{cap} of the 4-coils to the Drive Cylinder, where $V_{loop} = \oint E_\phi r d\phi$ in the region $r < R_{cyl}$, and V_{cap} is the capacitor bank voltage applied to the drive coils. The higher efficiency of the Drive Cylinder generates a higher reconnection electric field from $E_\phi(r = R_{separatrix}) = E_{rec}$, which in turn increases S (the separatrix is the radial position of the reconnection current sheet). The relationship between E_{rec} and S is found by using the normalized reconnection rate [80], $\alpha = E_{rec}/(v_A B_{rec})$, to express B_{rec} in terms of E_{rec}, giving

$$B_{rec} = \frac{(\mu_0 m_i n)^{1/4}}{\alpha}\sqrt{E_{rec}}. \tag{2.4}$$

Writing Eq. 2.1 as $S = \mu_0 L_{cs} B_{rec}/(\eta\sqrt{\mu_0 m_i n})$, and substituting Eq. 2.4 into this expression gives

$$S = \frac{\mu_0^{3/4} L_{cs}}{\eta \alpha^{1/2} (m_i n)^{1/4}}\sqrt{E_{rec}}. \tag{2.5}$$

This equation for S outlines how increasing L_{cs} and E_{rec} in the upgraded Drive Cylinder design allowed it to reach higher Lundquist number values, as shown in Fig. 2.1 and Section 2.1.1.

The rise in E_{rec} can be attributed to two characteristics of the Drive Cylinder: an increase in the efficiency and a smaller drive coil radius. The physical interpretation for the increased efficiency, resulting in a rise in E_{rec}, can be understood by examining the "private flux" in the region $0.5\,m < r < 0.7\,m$. The term private flux refers to the flux contours a single coil generates, which are distinct from the flux contours encircling multiple coils. Private flux can be seen in Fig. 2.5 and 2.6, above $R = 0.6\,m$, originating from each coil and extending upward to ~0.7 m, where the flux contours begin to merge. In contrast, below $R = 0.6\,m$ the individual flux contours combine to form a single flux contour just below the cylinder surface. This results in less magnetic flux being present between the cylinder surface and the drive coils. The reduction in flux contours minimizes the difference between the loop

voltage and drive coil voltage. Compared to a drive scheme based on discrete coils, this illustrates the enhanced efficiency of the cylindrical configuration.

The correlation between the private flux and the efficiency of the system is seen by examining the ratio V_{loop}/V_{cyl}, where V_{cyl} is the loop voltage at the Drive Cylinder surface, and V_{loop} is examined at $R = 0.5\,m$. Using the flux function ψ, defined in Appendix A.2.1 and expressed in terms of B_z as

$$\int \mathbf{B}\cdot d\mathbf{a} = 2\pi \int_0^r r' B_z(r', z)\, dr' = 2\pi\psi, \tag{2.6}$$

leads to an equation for V_{loop} by invoking Faraday's Law,

$$V_{loop} = \oint \mathbf{E}\cdot\, d\mathbf{l} = -\frac{\partial}{\partial t}\int \mathbf{B}\cdot d\mathbf{a}. \tag{2.7}$$

Combining Eq. 2.6 and 2.7 gives

$$V_{loop} = -2\pi\frac{\partial\psi}{\partial t}. \tag{2.8}$$

Using MATLAB to model the magnetic fields and associated flux for the Drive Cylinder, the value of V_{loop} was calculated from Eq. 2.8. The Drive Cylinder efficiency was then determined to be,

$$\frac{V_{loop}}{V_{cyl}} = \frac{V(R = 0.5\,m)}{V(R = 0.55\,m)} = 0.81. \tag{2.9}$$

A similar model and calculation was performed for the 4-coil system, which gave

$$\frac{V_{loop}}{V_{coils}} = \frac{V(R = 0.5\,m)}{V(R = 0.93\,m)} = 0.19, \tag{2.10}$$

where the radius of the 4-coils are $R = 0.93\,m$. Comparing these results shows the Drive Cylinder has a factor of ~4 increase in efficiency. With this understanding, the higher efficiency of the Drive Cylinder is derived from an increased number of coils in conjunction

	4-Coils	Drive Cylinder
Self-Inductance	1900	445
Capacitor	240	20
Breakout	-	11
Trans. Line	175	39
Switch	-	60

Table 2.2: Inductance values for components of the Drive Cylinder and 4-coil TREX systems. All values are in nH. The self-inductance row refers to the inductance of only the 4-coil and Drive Cylinder, respectively; these values were calculated by modeling the systems in MATLAB.

with the aluminum sheets. Both the aluminum sheets and the increased number of coils reduce the private flux, which lowers the inductance of the Drive Cylinder. Extrapolating upon this, the most efficient design for this geometry would be a cylinder formed from two sheets with a current applied directly to the sheets; the two sheets would replicate an infinite number of discrete coils and eliminate all private flux. Due to engineering limitations, such as high voltage connections through vacuum ports and a large inductance generated from a single current source, the 12 coil system was chosen in lieu of two aluminum sheets.

The second characteristic that increased E_{rec} is the 30% decrease in the drive coil radius. From Faraday's law in a toroidally symmetric system, E_{rec} can be expressed as [70]

$$E_{rec} = -\frac{1}{2\pi R}\frac{\partial \psi}{\partial t}. \tag{2.11}$$

Substituting $\partial\psi/\partial t$ from Eq. 2.8 into Eq. 2.11

$$E_{rec} = \frac{V_{loop}}{4\pi^2 R}. \tag{2.12}$$

From Eq. 2.12 it is clear a decrease in R will increase E_{rec}. Due to obvious physical constraints, the benefits of this characteristic is limited to the desired size of the observation region.

The improved efficiency, that is shown in Eq. 2.9, required a redesign of the transmission

lines connecting the capacitor bank to the cylinder. This was accomplished by reducing the self-inductance of the full transmission circuit compared to the self-inductance of the Drive Cylinder. Using Newton's notation for $\dot{I} = dI/dt$, the relationship between the voltage and self-inductance is $V = \dot{I}L$, such that

$$\frac{V_{cyl}}{V_{cap}} = \frac{\dot{I}L_{cyl}}{\dot{I}L_{tot}} = \frac{L_{cyl}}{L_{cyl} + L_{circ}}. \tag{2.13}$$

Here L_{circ} is the self-inductance of all elements in the circuit except the Drive Cylinder, and L_{cyl} is the Drive Cylinder self-inductance. For the drive coils to receive the largest voltage, the condition $L_{circ} \ll L_{cyl}$ must be met. Table 2.2 shows the improvements made to the system, which were accomplished in the following way. A lower inductance capacitor bank with a thyratron switch replaced the 4-coil capacitor bank that used a higher inductance ignitron switch. In addition, the 5 transmission lines used for each coil, all 15.25 m long, were replaced with 6 transmission lines for each coil, all 6.62 m long. These changes resulted in $L_{circ} \simeq L_{cyl}/5$, and an efficiency of

$$\frac{V_{cyl}}{V_{cap}} = 0.774. \tag{2.14}$$

Combining the results from Eqs. 2.9 and 2.14 gives an efficiency for the Drive Cylinder system of $V_{loop}/V_{cap} = 0.63$. Both the rise in efficiency and the decrease in radius effectively increased the reconnection electric field by a factor of ~9 over the 4-coil system.

2.3 Controlling the Formation of X-points and O-points

With the addition of a middle coil between the two halves of the Drive Cylinder, magnetic flux can be injected at $Z = 0$, increasing the magnetic pressure at this location. Magnetic flux passes more freely into the Drive Cylinder due to a gap of ~0.1 m between the two halves of the cylinder, as shown in Fig. 2.11(a). The gap, introduced for ease of diagnostic

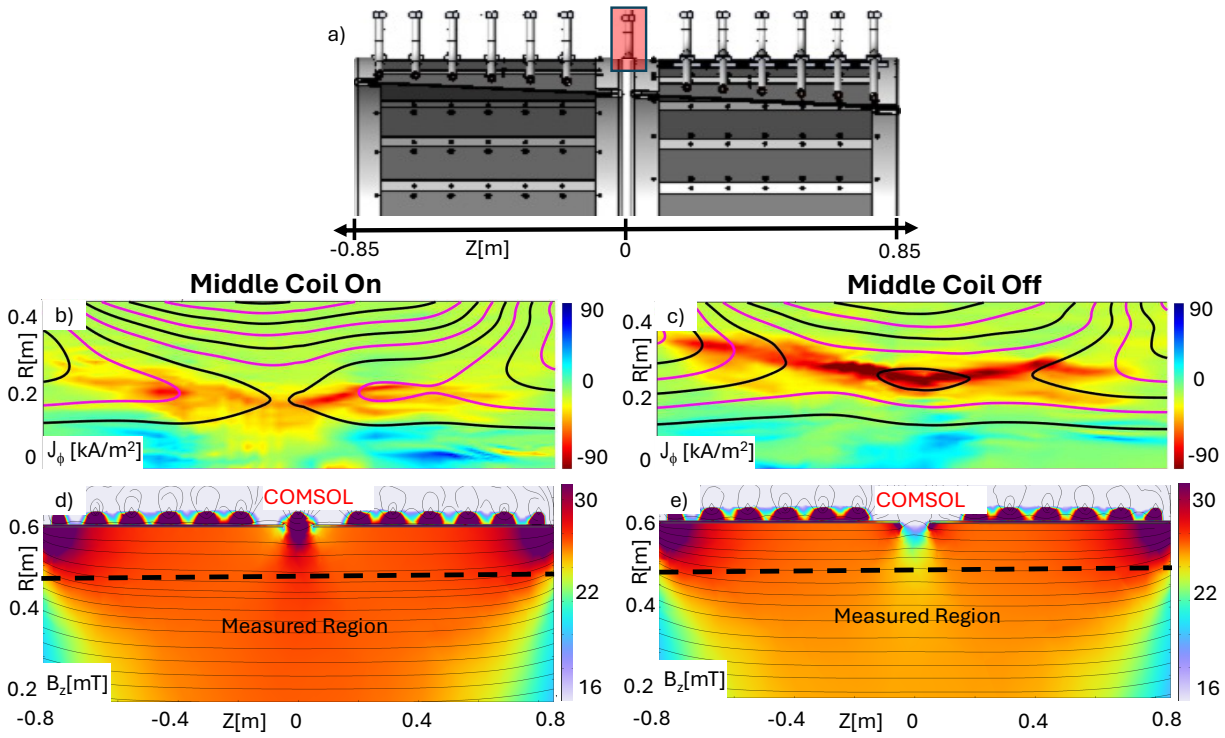

Figure 2.11: (a) shows the region in the Drive Cylinder where the following plots are located; the referenced middle coil is indicated in red. Plots (b) and (c) are measured using the same $\dot{B}$ probe array discussed in Fig. 2.9. Plots (d) and (e) show the vacuum field on and off, respectively. The region below the dotted lines of (d) and (e) illustrate the maximum range of the $\dot{B}$ probe array. The formation of (b) X-points and (c) O-points was achieved using the configurations shown in (d) and (e).

access to the reconnection region, allows some stray B_r to enter the interior of the cylinder, altering the anti-parallel field configuration. Variation in the vacuum field configuration with the middle coil on or off was rendered using COMSOL, and is shown in Fig. 2.11(d) and (e). Due to the limited radial range of the $\dot{B}$ array, used to measure the field of the Drive Cylinder along the Z-axis, measurements are limited to $R_{max} = 0.46$ m as indicated by the dotted lines in Figs. 2.11(d) and (e). Using vacuum field measurements from the $\dot{B}$ array, only a difference of ~2% are observed between the middle coil on or off. Despite this small difference, the observed reconnection dynamics are altered: an O-point forms with the middle coil off as shown in Fig. 2.11(c), and an X-point is induced when the middle coil is on, Fig. 2.11(b). The black and magenta contour lines of Fig. 2.11(b) and (c) are lines of

constant flux which map to the in-plane magnetic field lines; the lines' colors alternate for clarity.

2.4 Summary and Conclusion

The Terrestrial Reconnection EXperiment has been significantly upgraded with the new Drive Cylinder's ability to reach the kinetic regime, as illustrated in Fig. 2.1. Using a similar voltage range as past setups, the higher efficiency of the Drive Cylinder produces a reconnection electric field up to 900 V/m, driving the electron fluid through the diffusion region on a time scale less than the electron-ion collisions time scale. In addition, the design of the Drive Cylinder allows the manipulation of plasma dynamics within its interior by altering the configuration of the magnetic field. These configurations range from a uniform field along the Z-axis, which allows the reconnection layer to develop with minimum magnetic field perturbations, to a direct injection of magnetic flux at the midplane of the cylinder, allowing the formation of X-points and O-points. With these capabilities, the Drive Cylinder will study regimes of reconnection relevant to Earth's magnetosphere, and explore the electron diffusion region where the role of electron pressure anisotropy is believed to influence the reconnection process.

Further Discussion

What follows are extended sections beyond the paper, discussing preliminary studies of electron heating, further upgrades to the Drive Cylinder, and diamagnetic suppression of magnetic reconnection.

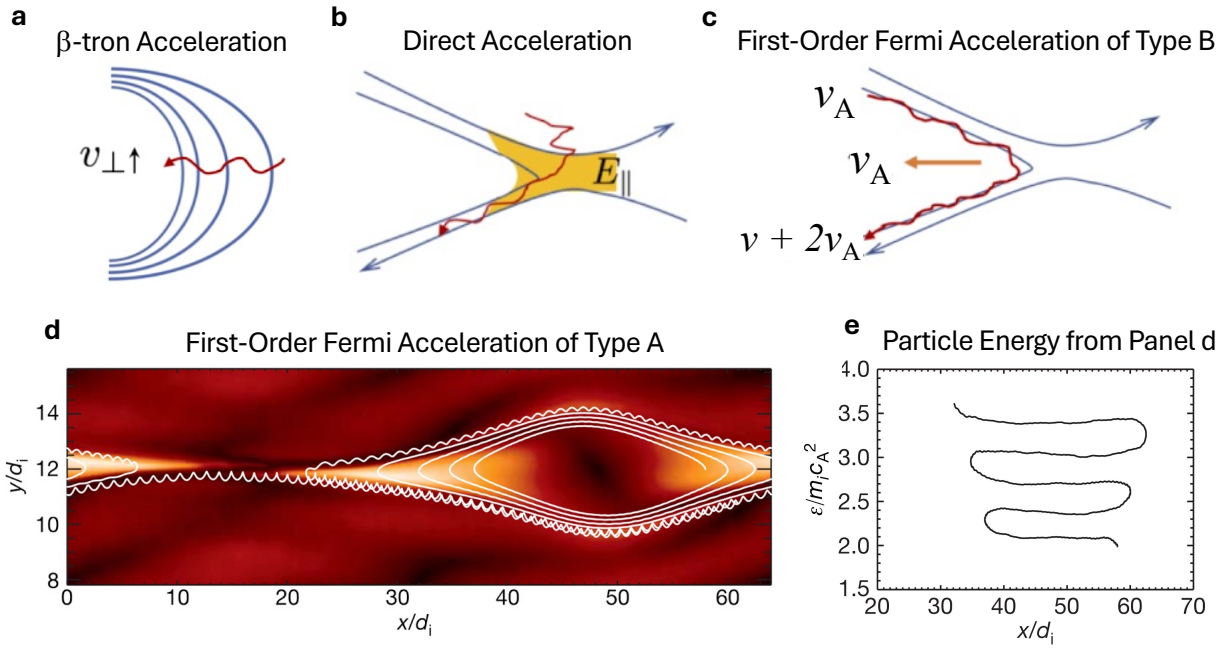

Figure 2.12: Panel (a) shows betatron acceleration increasing (decreasing) $v_\perp$ in the presence of an increasing (decreasing) magnetic field. Direct acceleration is depicted in panel (b) by an electric field component parallel to the magnetic field. Fermi acceleration of type B is shown in panel (c) where the curved magnetic field drifts at the Alfveǹ speed, v_A. Panels a – c reproduced from [67]. Panel d shows is an example of Fermi acceleration of type A where an electron orbit is shown in white. Panel (e) illustrates the energy boost given to the electron as the magnetic island is compressed and the electron orbit length is reduced, adapted from [18].

2.5 Island Coalescence as a Mechanism for Electron Heating

Spacecraft observations have shown that magnetic reconnection can accelerate particles to very high non-thermal energies [67] (and references there in). The same mechanisms responsible for producing these energetic particles also contribute to heating the bulk plasma. Using the low-collisionality plasma generated by the Drive Cylinder, heating processes that are normally obscured by resistive diffusion can now be studied in a laboratory setting. The primary mechanisms that contribute to particle heating in the reconnection region are: betatron acceleration, which occurs when the magnetic field strength increases

while the magnetic moment is conserved; direct acceleration by parallel electric fields (see Sec. 1.2.6); and first-order Fermi acceleration, which can be classified as type A or type B [65, 2, 12, 54]. When the parallel action is conserved, type A Fermi acceleration occurs as the bounce orbit of a trapped electron shortens, while type B results from the tension force of a dynamically evolving curved magnetic field [65]. Examples of each mechanism are shown in Fig. 2.12(a–d).

Historically, it was believed the dominant mechanism that energized thermal electrons occurred along the X-line through direct acceleration by the out-of-plane reconnection electric field. However, theoretical studies [18, 27, 62] and spacecraft observations [67] have since revised this picture, highlighting an adiabatic framework in which the in-plane parallel electric field plays a central role. The parallel electric field has been shown to seed a population of trapped thermal electrons by increasing their parallel velocity [24]. These electrons, initially energized by $\Phi_{\parallel}$, subsequently experience enhanced betatron and Fermi acceleration, since the energization rates of both processes scale approximately with electron energy.

It is our goal to form a multi X-point configuration such that multiple magnetic islands form and coalesce. With the merging of these islands thermal electrons, with $v_{||} \gg v_{\perp}$, are able to reflect many times relative to the convection speed of the magnetic field. This process will conserve the parallel action, $J = \int v_{||}\, dl$, while boosting $v_{||}$.

2.5.1 Perturbing the Uniform Background Field: Perturbation and Push-Coil Upgrades

Generating a multi X-point field configuration within the reconnection current layer required altering the uniform field configuration of the Drive Cylinder. Two types of coils were added to achieve this; three-turn perturbation coils shown in Fig. 2.13 whose fields diffuse through the Drive Cylinder, and single turn push coils shown in Fig. 2.14 that produce a magnetic barrier at the ends of the Drive Cylinder.

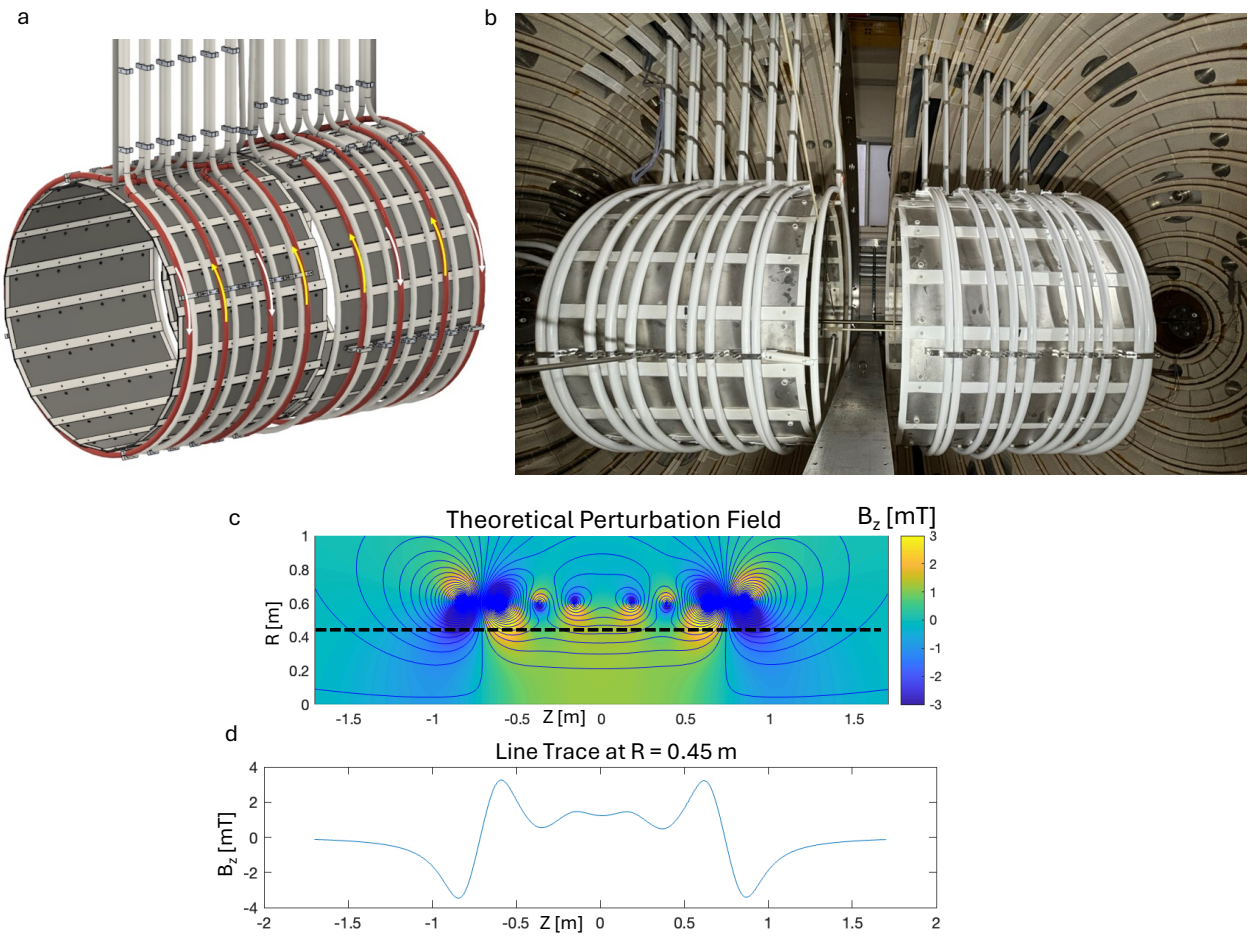

Figure 2.13: Highlighted in red, panel **a** shows a CAD render of the perturbation coils added to the exterior of the Drive Cylinder with the arrows indicating the current direction. Panel **b** is the Drive Cylinder installed with the additional perturbation coils. Panel **c** and **d** is the theoretical field for the perturbation coil configuration used to form the islands in Fig. 2.15.

For the fields from the perturbation coils to penetrate the shell of the Drive Cylinder each coil is powered by a Pulse Forming Network (PFN) . Each PFN produces a constant current output (<5 % ripple) up to 1 kA at 100 V over a 10 ms interval [69], providing sufficient time (>4 ms, as described in Fig. 2.10) for the field to diffuse through the cylinder before the drive coils are energized. Due to the magnetic pickup coils measuring field changes on the order of a μs, it was necessary to add the ms changes of the perturbation coils to the measured data using theoretically calculated fields; a representative theoretical

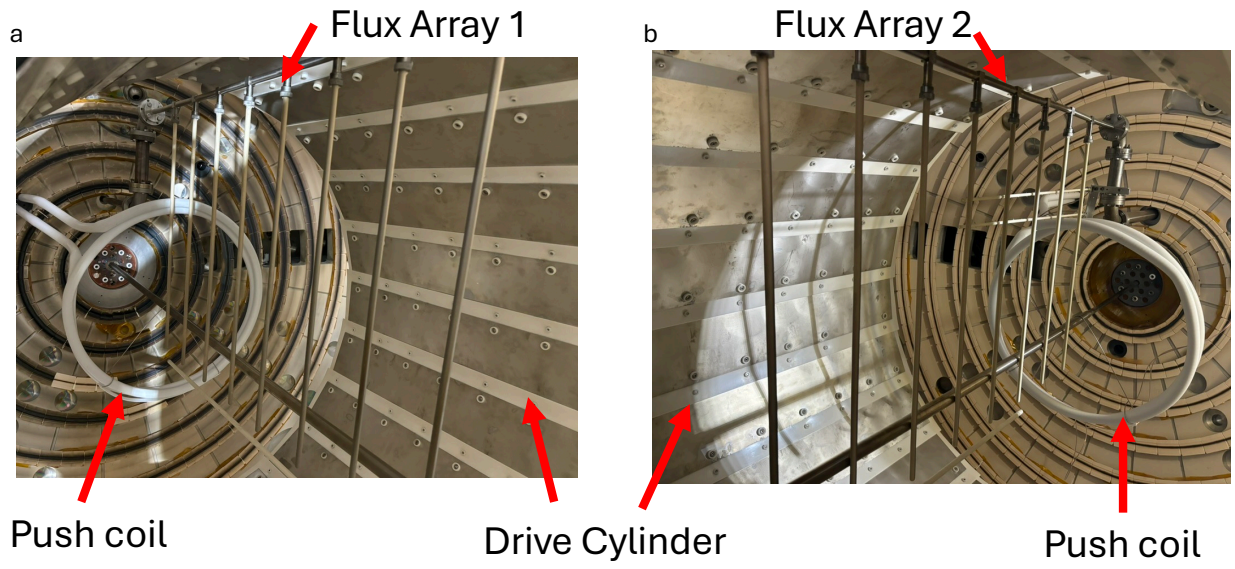

Figure 2.14: Panels **a** and **b** show the push coils installed on each end of the Drive Cylinder. Both coils are 15cm from the edge of the Drive Cylinder.

field is shown in Fig. 2.13(c,d).

Under many conditions, rather than coalesce, the islands seeded by the perturbation coils diverged along the z-axis. To suppress this effect, push coils were installed approximately 0.5 m from the ends of the cylinder. These coils formed magnetic barriers that prevented the magnetic islands from moving toward the cylinder ends. Wired in parallel, the single turn push coils were powered by a 1 mF capacitor bank set at a maximum of 5 kV with a peak current of 30 kA.

2.5.2 Merging Magnetic FRC Islands

The successful creation and merging of magnetic islands is shown in Fig. 2.15, where the white and black lines are flux contours and the red line is the $B_z = 0$ contour. Though merging islands were observed, repeatable conditions were not achieved. Possible reasons for the lack of reproducibility may be from impurities in the plasma due to degrading plasma guns and an increased population of neutrals. These suspicion are due to islands forming, as shown in Fig. 2.15 top panel, but ceasing to merge immediately after the

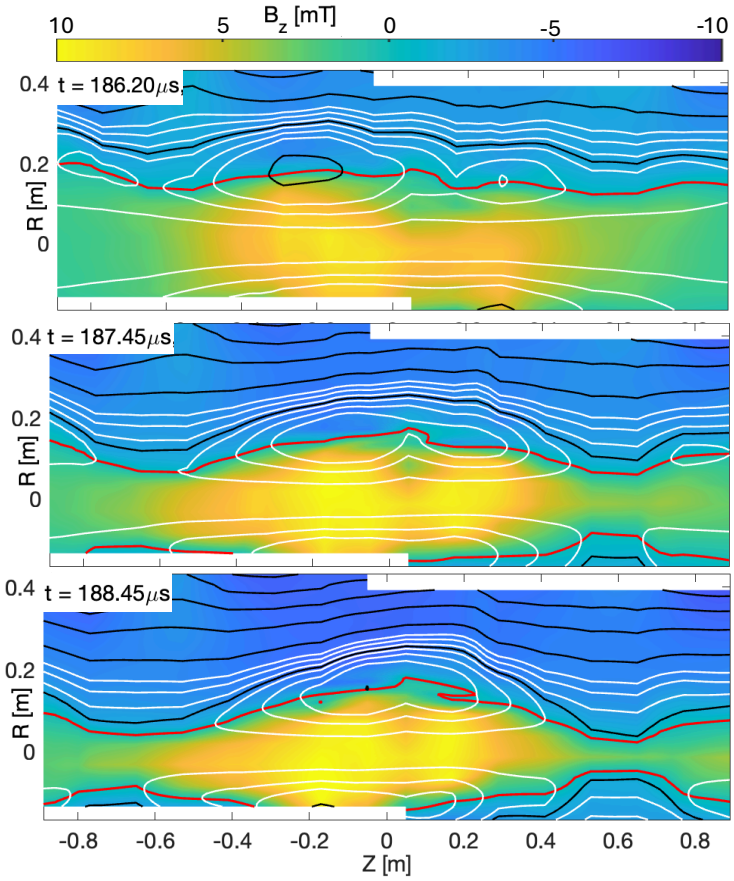

Figure 2.15: In each panel, the white and black lines show magnetic flux contours, with the red lines indicating $B_z = 0$. The top panel at $t = 186.20\,\mu s$ shows the formation of two magnetic islands, which coalesce over the $\sim 2\mu s$ interval shown in the bottom two panels. Further confirmation of the formation and merging of these islands is seen in the distinct yellow high field regions below each flux tube. The merger of these high field regions over the $\sim 2\mu s$ correlates with the merging of the flux tubes.

cryogenic pumps were regenerated. Additionally, inspection of the plasma guns post run campaign revealed extensive damage to both the guns and their mounting hardware . Due to these issues, it was not possible to complete the investigation of islands merging, since temperature and density measurements were not attained.

Future work will alter the perturbation coil configuration, reducing them to a single coil for each half of the Drive Cylinder. It is believed this simpler configuration will facilitate the creation of an X-point in each half of the cylinder. In addition, the plasma guns have been updated with new puff valves, which will improve their performance by reducing

the internal degradation that has been observed. The plasma gun upgrades are further discussed in Appendix A.5.

2.6 Diamagnetic Suppression of Magnetic Reconnection

Simulations [95] and magnetopause spacecraft observations [76] have demonstrated that the rate of reconnection is suppressed in systems with both guide field and density gradients across the reconnection current layer. This effect is due to the resulting diamagnetic drift,

$$\mathbf{v}_* = -\sum_{j=1}^{2} \frac{1}{n q_i} \frac{\nabla p_j \times \mathbf{B}}{B^2} = \mathbf{v}_{*\mathbf{i}} + \mathbf{v}_{*\mathbf{e}}, \tag{2.15}$$

where q_i is the charge of the species, n is the number density, and $p_j = nT_j$ is the species scalar pressure. When the density gradient is parallel to the width of the current layer and an out-of-plane guide field is present, $\mathbf{v}_*$ is in the direction that traverses the length of the current layer. A gradient in the guide field is necessary, otherwise $\nabla p = 0$ and hence $\mathbf{v}_* = 0$. This is due to

$$\mathbf{J} \times \mathbf{B} \simeq \nabla p, \tag{2.16}$$

which can be found by adding the electron and ion equations of motion for a collisionless plasma, where the inertial term is dropped as its effects are considered small and quasi-neutrality eliminates the electric field term. Replacing $J = 1/\mu_0 \nabla \times \mathbf{B}$ and using the vector identity, $(\nabla \times \mathbf{B}) \times \mathbf{B} = (\mathbf{B} \cdot \nabla)\mathbf{B} - (1/2)\nabla B^2$, equation 2.16 can be written as

$$\frac{1}{\mu_0}(\mathbf{B} \cdot \nabla)\mathbf{B} - \frac{1}{2}\nabla B^2 = \nabla p. \tag{2.17}$$

Since the only nonzero component of $\mathbf{B}$ near the X-point is the guide field, this relation states that if $\nabla_\phi B = 0$ then $\nabla p = 0$, where ϕ is the guide field component .

Under the conditions that support diamagnetic drift, the X-point convects in the ion

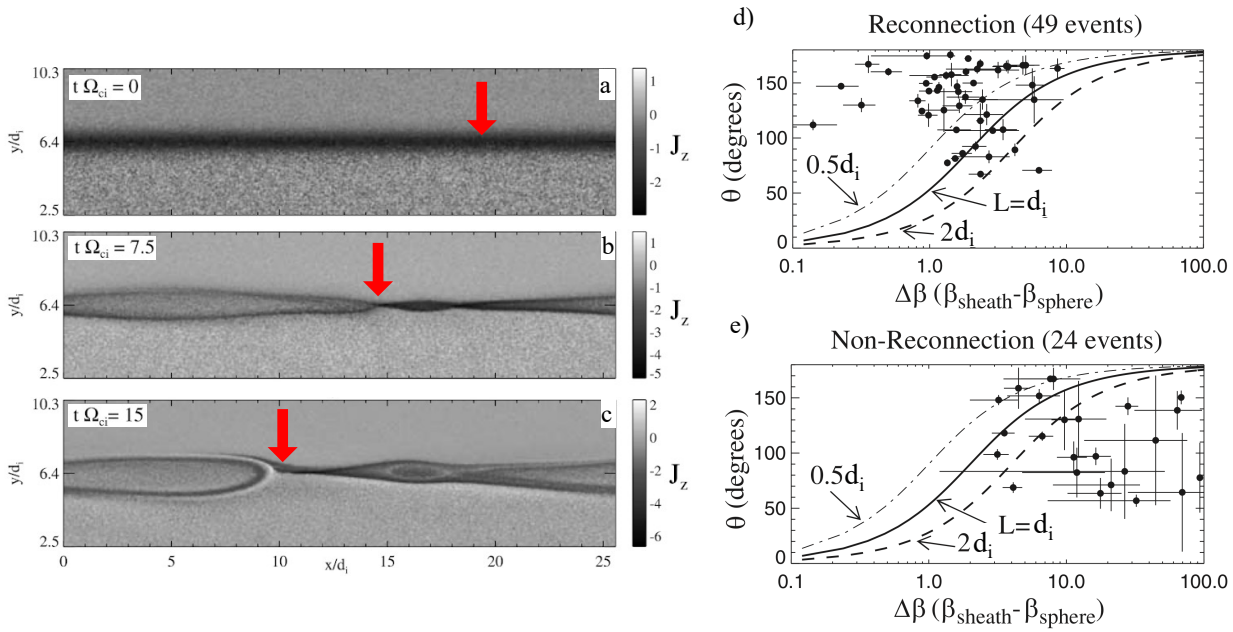

Figure 2.16: Panels a–d, adapted from [95], show the out of plane current density in the presence of a guide field in a 2.5D kinetic simulation. The drift of the X-point is illustrated by the red arrows. In Panels e and f, the dot-dashed, solid, and dashed lines are plots of equation 2.18 with $L_p/d_i = 0.5, 1, 2$, respectively. The data, reproduced from [76], are measurements from magnetopause crossings of the THEMIS spacecraft, showing consistent observations with predicted values from equation 2.18.

rest frame with a speed $|\mathbf{v}_*|$. If the drift velocity of the X-point exceeds the Alfvenìc outflow velocity reconnection is suppressed, which is due to the magnetic tension's inability to eject field lines from the X-point region. The suppression condition for reconnection is then $v_* \geqslant v_A$, which can be written as a condition in $\beta = 2n\mu_0(T_i + T_e)/B^2$ [94]:

$$\Delta\beta \geqslant \frac{2L_p}{d_i}\tan(\theta/2) \quad , \tag{2.18}$$

where L_p/d_i is the width of the plasma pressure gradient across the current sheet in units of the ion skin depth, d_i, and θ is the shear angle between the components of the reconnecting fields. Here, $\Delta\beta$ represents the difference in β across the reconnection layer.

Simulations and spacecraft observation near Earth's magnetopause give typical values of $L_p/d_i \simeq 1$ [1, 22]. It can also be seen from equation 2.18 that when $\theta = \pi$, for anti-

parallel reconnection, diamagnetic suppression does not occur since the requirement is $\Delta\beta > \infty$. This is due to diamagnetic drift velocity having no component in the plane of the reconnection layer. For guide fields on the order of the in-plane reconnecting field, and typical values of $L_p/d_i \simeq 1$, the threshold for suppression of reconnection is $\Delta\beta \gtrsim 1$.

The dynamics of diamagnetic suppression of magnetic reconnection were first captured in 2.5D PIC simulations, shown in Fig. 2.16(a–d) [95], which demonstrated that the X-point drifts as reconnection is suppressed. Furthermore, THEMIS spacecraft observations of reconnection dynamics, obtained during magnetopause crossings, show strong correlation with the theoretical predictions of equation 2.18, as illustrated in Fig. 2.16(e,f). Here, the dot-dashed, solid, and dashed lines correspond to equation 2.18 evaluated for $L_p/d_i = 0.5,\ 1,$ and 2, respectively. Diamagnetic suppression is expected only when $\Delta\beta$ exceeds these curves, which is consistent with the behavior shown in the figures.

2.6.1 Diamagnetic Suppression Experimental Setup

Altering the setup shown in Fig. 2.2, diamagnetic suppression was initiated in the Drive Cylinder by installing a toroidal field (TF) coil along its central axis (red line in Fig. 2.17(a)). The TF coil generates an out-of-plane guide field, $B_{\phi 1}$. Due to the $1/r$ decreases in the TF coil field strength, the guide field strengthens as the reconnection layer moves radially inward. In addition, the anti-parallel fields produced by the Helmholtz (HH) coil and the Drive Cylinder create an asymmetric field configuration, as illustrated in Fig. 2.17(b).

Measurements of the magnetic field dynamics within the Drive Cylinder region shown in Fig. 2.17(c,d) were performed using Flux Arrays 1 and 2, which are B-dot probe arrays described in Appendix A.2. Each array provides a time-resolved measurement of dB_z/dt over a 0.6×0.84 m plane. The current density is then found in terms of the flux function ψ, with assumption of cylindrical symmetry ($\partial/\partial\phi = 0$). The procedures for calculating ψ and $J_\phi(\psi)$ are detailed in Appendices A.2.1 and A.2.2, respectively. From these measurements, the temporal evolution of the reconnection current layer with its corresponding X-point

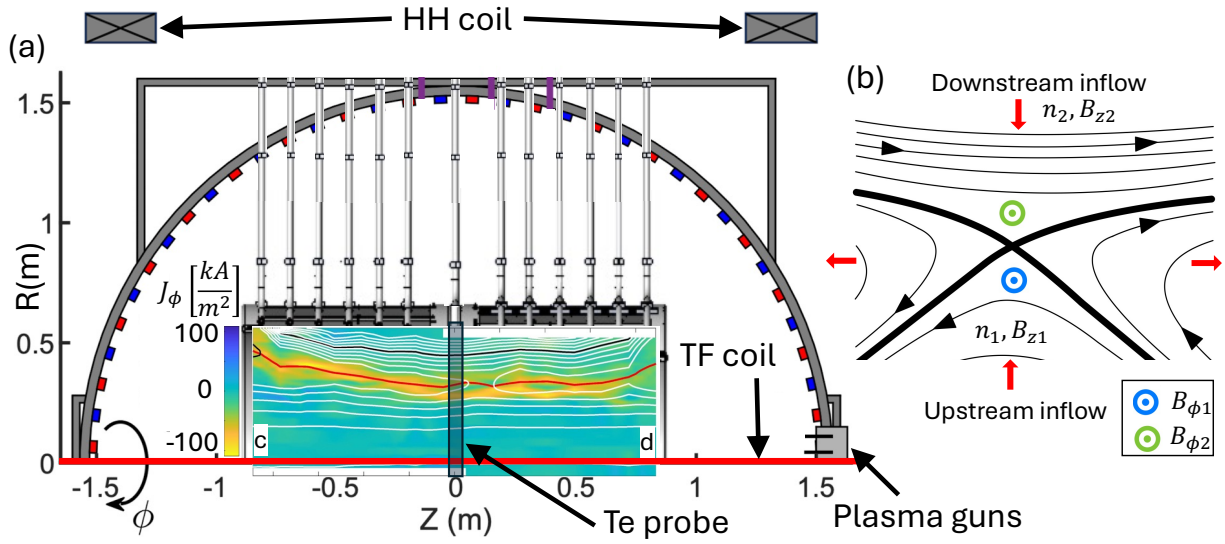

Figure 2.17: Panel (a) shows the experimental setup for investigating diamagnetic suppression using the Drive Cylinder inside the BRB vacuum vessel. Inset panels (c) and (d) show the current density as measured by Flux Arrays 1 and 2 respectively. Panel (b) is a representative sketch of the different regions of asymmetric reconnection that occurs within the Drive Cylinder.

location, are determined for a single discharge event.

The density gradient required for diamagnetic drift forms naturally from the theta-pinch equilibrium established prior to energizing the Drive Cylinder. In this state, the radial plasma pressure is balanced by magnetic pressure. Since the plasma guns are located at a radial position of approximately 0.1 m, most of the injected plasma remains at small radii, frozen-in to the field lines it first encounters. This pressure gradient was measured using a T_e probe along the radial line indicated by the shaded box in Fig. 2.17a. The corresponding density and electron temperature measurements are shown in Fig. 2.18(a,b). The X-line indicated in panel (a) corresponds to the $B_z = 0$ contour, and the shock line occurs just before the magnetic pile-up as discussed in [70]. The density gradient across the X-line is clearly apparent, which completes the necessary requirements for a diamagnetic drift velocity to be present.

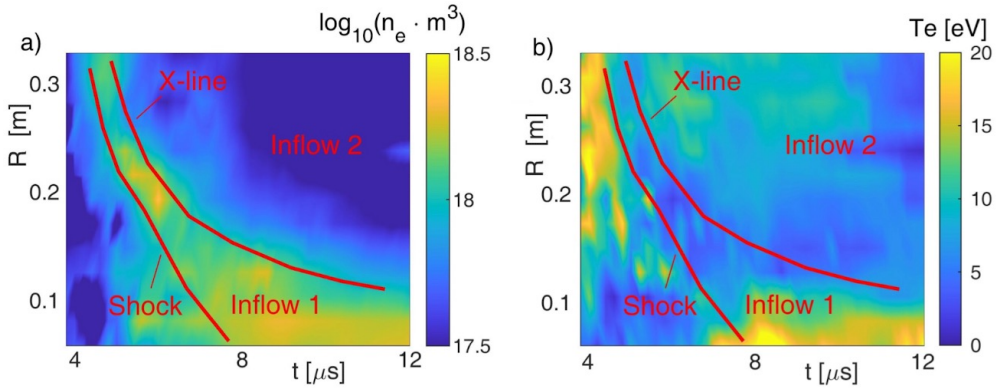

Figure 2.18: Using the 16-tip Langmuir T_e probe, panels (a) and (b) show density and electron temperature measurements from a radial scan in the shaded region of Fig. 2.17(a). Theses plots were created by J. Egedal and C. Kuchta.

2.6.2 Preliminary Observation of Diamagnetic Suppression

The goal of this section is to demonstrate that suppression conditions exist in the Drive Cylinder that are relevant to spacecraft observations and simulation runs. Future work will aim to diagnose the effects of these conditions on the reconnection rate. In Fig. 2.19, column 1, each panel shows a different discharge event 5 μs after the Drive Cylinder is energized. The three rows correspond to different TF coil currents, $I_{TF}/kA = \{5.7, 0, -7.9\}$. At this early time, the influence of the resulting B_ϕ field is minimal due to its reduced value at the current layer's large radial position. As a result, the guide-field effect is weak, and the X-point locations are similar for $t = 5\,\mu s$.

In the second column of panels, corresponding to $t = 10\,\mu s$, the current layers have moved into a region of stronger guide field, where a diamagnetic drift velocity becomes evident. The direction of this drift depends on the sign of B_ϕ, which determines the advection direction of the X-point. In row one, where $I_{TF} = 5.7\,kA$, the X-point shifts toward the positive Z-direction. In contrast, in row two, with $I_{TF} = 0\,kA$, the diamagnetic effect is suppressed, allowing multiple X-points to develop, potentially leading to the onset of the plasmoid instability. Finally, in row three, the current polarity is reversed ($I_{TF} = -7.9\,kA$), causing the X-point to shift toward the negative Z-direction. The reduced

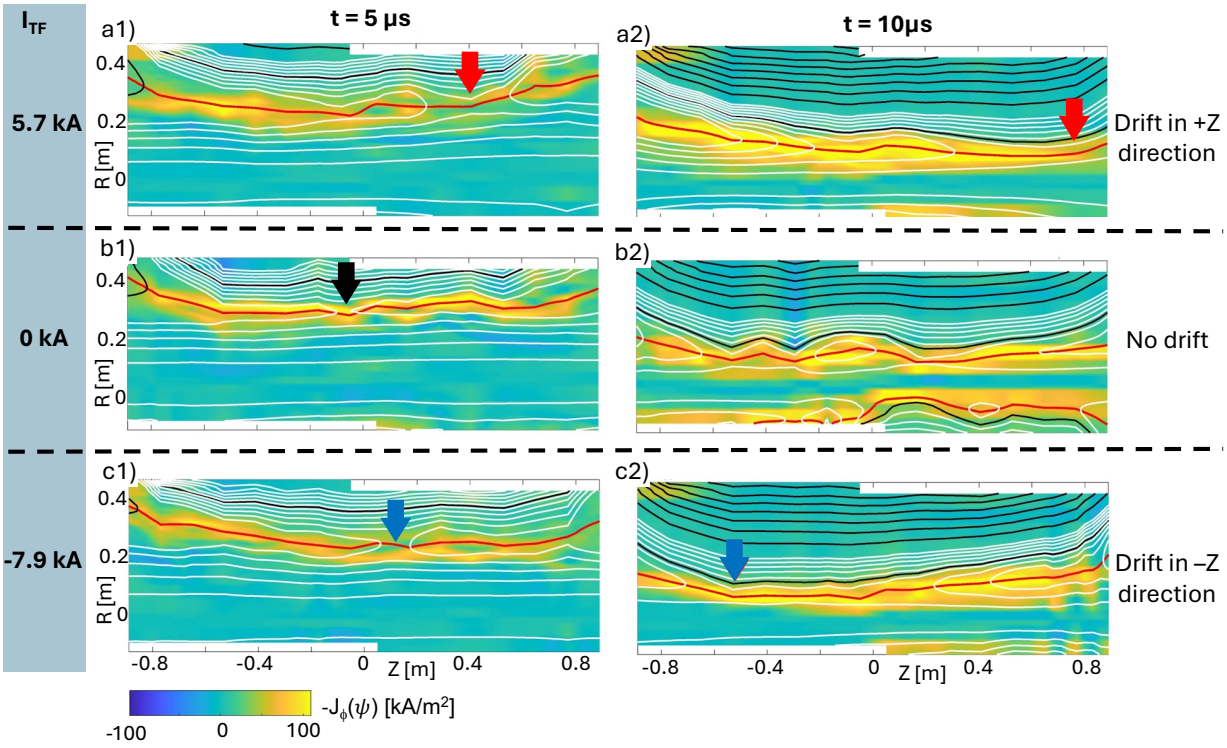

Figure 2.19: Color contour plots of the current density, $J_\phi(\psi)$, are shown together with magnetic field line contours (white and black lines). Each row, from top to bottom, corresponds to a TF coil current of $I_{TF}/kA = \{5.7, 0, -7.9\}$. The two columns represent times of 5 and 10 μs, allowing the drift of the X-point location to be observed. Comparing rows one and three, the reversal in the polarity of I_{TF} changes the direction of the diamagnetic drift velocity and, consequently, the direction of the X-point motion. Row two illustrates that removal of the guide field suppresses the X-point drift entirely, with the formation of multiple X-points indicating the development of a plasmoid instability.

X-point drift observed between $I_{TF}/kA = \{5.7, -7.9\}$ is likely due to an asymmetry in plasma density along the Z-axis. It is anticipated that the addition of a second plasma gun at the negative Z position will mitigate this asymmetry. Qualitatively, these dynamics exhibit strong similarity to the PIC simulation results shown in Fig. 2.16(a–d). Future work will include a quantitative analysis of the reconnection rate to more directly attribute the observed changes to diamagnetic drift effects.

A further demonstration of the effect diamagnetic suppression has on reconnection can be seen by examining the suppression condition stated by equation 2.18. The density and electron temperature measurements for calculating $\Delta\beta$ were determined by a radial scan

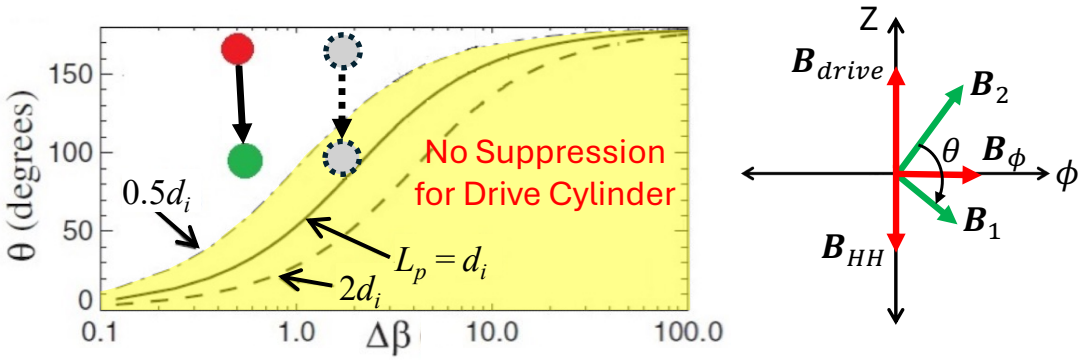

Figure 2.20: The left panel shows equation 2.18 plotted for $L/d_i = 0.5, 1$, and 2 using dot–dashed, solid, and dashed curves, respectively. The yellow region indicates the suppression threshold for the Drive Cylinder at the appropriate value $L/d_i = 0.5$. Red and green dots mark the change in shear angle as the guide field increases when the X-point moves radially inward from $t = 5$ to 10 μs, as shown in rows 1 and 3 of Fig. 2.19. Gray dots denote projected values of $\Delta\beta$ for future runs. The right panel illustrates the out-of-plane coordinate system used to calculate the shear angle θ, where $\mathbf{B}_1$ is the upstream and $\mathbf{B}_2$ is the downstream fields shown in Fig. 2.17(b), $\mathbf{B}_{drive}$ is the Drive Cylinder field, and $\mathbf{B}_{HH}$ is the Helmholtz field.

of the Te probe, the results are shown in Fig. 2.18. Approximating the total temperature as constant across the current layer, with the understanding that $T_e > T_i$ for our experiment gives, $T \simeq T_e \simeq T_e + T_I \simeq 10\,\text{eV}$. Additionally, if we assume anti-parallel reconnection, the reconnection field is $B_{rec} \simeq 4\,\text{mT}$. With these approximations, β can be written as

$$\beta_k = \left(\frac{2\mu_0 T}{B_{rec}^2}\right) n_k = (2.5^{-19}\,\text{m}^3) n_k, \tag{2.19}$$

where the subscript $k = \{1, 2\}$ distinguishes between the inflow regions on either side of the current layer, as shown in Fig. 2.17(b). In region 1 the density is $n_1 \simeq 2 \times 10^{18}$, giving $\beta_1 \simeq 0.5$. For region 2, the density is $n_2 \simeq 1 \times 10^{17}$, and $\beta_2 \simeq 0.03$. Which gives a plasma beta across the current layer of $\Delta\beta \simeq 0.5$.

Since the change in $\Delta\beta$ occurs over the same spatial region as L_p/d_i [94], and with $d_i \simeq 0.2\,\text{m}$, we find $L_p/d_i = \Delta\beta \simeq 0.5$. Using equation 2.18, this value defines the yellow suppression region shown in the left panel of Fig. 2.20. Comparing this to the discharge events in Fig. 2.19, the red and green points represent the change in shear angle that

occurs as the current layer moves radially inward from $t = 5$ to $10\,\mu s$, respectively. The definition of the shear angle for this system is illustrated in the right panel of Fig. 2.20. As noted earlier, the initial high shear angle (red point) arises from the low B_ϕ value at larger radii, resulting in nearly anti-parallel reconnection. As B_ϕ increases, the shear angle correspondingly increases, reaching a maximum value of $\theta \simeq 90^\circ$.

A future investigation will change $\Delta\beta$ in two ways, such that the projected gray dots in Fig. 2.20 are measured. First, the density will be increased by a factor of 2 by adding a second plasma gun to the opposite pole of the BRB vessel, increasing the density in region 1. Second, reducing the Helmholtz field will lower the field in the downstream region effectively reducing β_1. Both of these changes will allow us to vary $\Delta\beta$ such that a set of parameters can be found that satisfy the suppressed criterion.

3 TOPOLOGICAL BIFURCATION OF A MINI-MAGNETOSPHERE TRIGGERS FAST MAGNETIC RECONNECTION

Can a min-magnetopause be created from the exhaust of a reconnection event? What is the mechanism in the system that causes reconnection to rapidly increase? Is this mechanism unique to this experiment, or can it be applied to broader 3D systems?

While advances in the onset of 2D magnetic reconnection have revealed mechanisms such as the plasmoid instability[91, 57], the physical process required to transition to fast reconnection in fully 3D systems remains an open question[79, 100, 44]. Contrary to 2D reconnection, which occurs at well-defined X-points between antiparallel magnetic fields, 3D reconnection takes place across extended regions, as discussed in section 1.3. The diversity of reconnection sites, coupled with the intrinsic complexity of 3D magnetic topologies, heightens the difficulty of determining a trigger mechanism. Nevertheless, there is growing theoretical[78] and numerical[14, 100, 53] evidence that highlights the presence of reconnection phenomena that are inherently 3D. Experimental investigations, however, have been hindered by the challenge of obtaining volumetric, time-resolved measurements of the evolving magnetic field structures [17, 4].

What follows is a description of the direct observations of fast 3D magnetic reconnection triggered by a topological bifurcation[83] of the magnetic skeletal structure in a laboratory mini-magnetosphere. Magnetic volumetric measurements reveal that the rotation of the background magnetic field drives separatrix surfaces of the dipole topology toward one another. The crossing of these separatrices culminates in a bifurcation of the skeletal structure through the spontaneous formation of new null points and a reconfiguration of the separator. The topological transition coincides with a sharp rise in the reconnection electric field and a normalized reconnection rate approaching values characteristic of electron-only reconnection. The experimental observation reveals an effective pathway

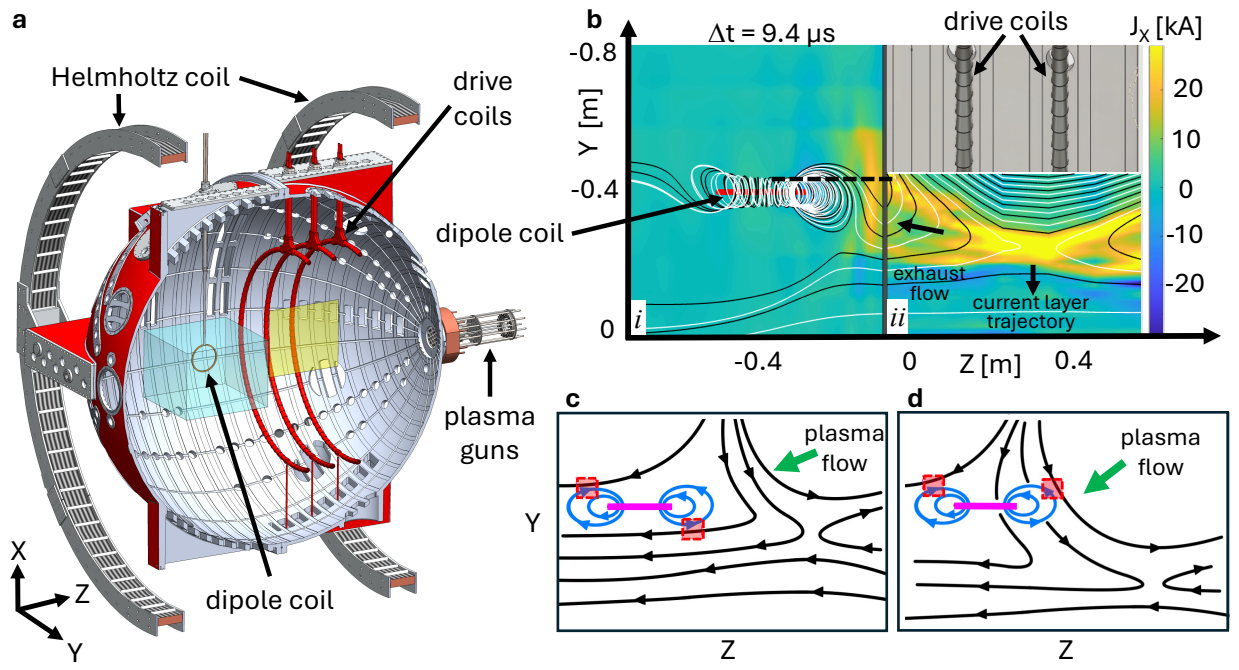

Figure 3.1: Panel **a** is a CAD render of the experimental system, which includes the 3 m radius BRB vacuum vessel, six plasma washer guns, a 12 turn 0.12 m radius physical dipole, three single turn 0.93 m radius drive coils, and an external 4 m Helmholtz coil. The blue shaded box (0.60 x 0.84 x 0.70) m is the volume scanned by Flux Array 2 and the yellow plane (0.6 x 0.48) m is the area measured by Flux Array 1. Panel **b** is a slice of the YZ mid-plane with the J_X current density from the blue and yellow regions of panel **a** plotted in ***i*** and ***ii***, respectively. Utilizing the rotational symmetry in the drive coil region, the yellow plane of plot **a** was rotated into the YZ mid-plane, generating plot ***ii***. Measurements from the Langmuir probe were taken along the black dashed line indicated in panel ***i***. Panels **c** and **d** show schematic representations of the dipole field (blue) and the background field (black), plotted separately. The red boxes indicate the expected locations of magnetic null points if the two fields were superimposed. By comparing panels **c** and **d**, the motion of the windward null is attributed to the change in direction of the background field caused by the inward movement of the reconnection current layer generated by the drive coils.

to fast 3D reconnection via a topological bifurcation, underscoring the importance of full-volumetric diagnostics for uncovering reconnection onset physics in both astrophysical and laboratory plasmas.

3.1 Experimental Setup

Using the Big Red Ball (BRB) device at the Wisconsin Plasma Physics Laboratory (WiPPL) [32], a mini-magnetosphere impacted by an external plasma is realized by embedding a 0.12 m radius physical dipole into the exhaust of the otherwise cylindrically symmetric TREX magnetic reconnection experiment [70]. The experimental geometry is shown in Fig. 3.1, where the out-of-plane current component J_x is plotted in panel **b**. Streamlines from the dipole region (panel **i**) and the Alfvénic wind generated by the TREX reconnection current layer (panel **ii**), illustrate the interaction between the reconnection outflow and the embedded dipole.

Significantly, the radial motion of the current layer causes the associated magnetic field reversal to sweep past the dipole, dynamically altering the angle between the background and dipole magnetic fields; this is a parameter that to our knowledge has yet to be systematically investigated in previous magnetopause experiments [86] or simulations [16]. The evolving background field can be compared to the interplanetary magnetic field (IMF) angle changing, which increases the probability of magnetic sub-storms [48]. Recently, Kelvin Helmholtz instabilities far upstream of Earth have been proposed as a mechanism for rapid modulation of the IMF, enhancing the storms in the Earth's magnetosphere [66].

The changes in the background field are illustrated in Fig. 3.1(**c**,**d**), where the separate fields of the dipole (blue) and background field (black) are overlayed with the locations of the resulting magnetic nulls (red boxes). The motion of the current layer from panel **c** to **d**, whose trajectory is shown in **b**, leads to a rapid local reorientation of the background field near the windward side of the dipole, as shown in Section 3.3.1, initiating a topological bifurcation. The resulting configuration aligns the dipole null with the dominant plasma flow direction, as set by the total current trajectory and reconnection exhaust, indicated in Fig. 3.1(**ii**).

When the dipole is positioned in the path of the Alfvénic wind (i.e. the TREX reconnection exhaust), an out-of-plane current J_x is induced, forming a magnetopause with

a normalized scale length $L/d_i \approx 1$, where $d_i = c/\omega_i$ is the ion skin depth, ω_i the ion plasma frequency, and L the distance from the dipole center to the current layer. Fig. 3.2(**a**) identifies the approximate location of the magnetopause from the increased plasma density relative to the dipole edge, giving $L \approx 0.25\,m$. The plasma density and electron temperature were obtained using a 16-tip Langmuir probe (described in section A.4) scanned along the dashed line in Fig. 3.1(**b**), with the resulting measurements given in Table 2.1 and Fig. 3.2(**a**,**b**). In normalized terms, the system geometry is comparable to a lunar or cometary magnetopause[71], much smaller than the Earth's magnetopause, for which $L/d_i \approx 600$. Observed features, such as a density pileup at the bow and Alfvènic and sonic Mach numbers near unity, indicate a sub-critical regime in which no bow shock forms.

Plasma Parameters		
Density	$n\ [m^{-3}]$	(1-30)$\times 10^{17}$
Electron Temperature	$T_e\ [eV]$	3-30
Ion Skin Depth	$d_i\ [m]$	0.25
Ion Larmour Radius	$r_L\ [m]$	0.16
Dipole Magnetic Moment	$M\ [kA\ m^2]$	~6
Flow Velocity	$v_{flow}\ [km/s]$	~36
Alfvén velocity	$v_A\ [km/s]$	20 - 40
Sound Speed	$v_S\ [km/s]$	25 - 60
Magnetopause Distance	$L\ [m]$	~0.25
Dimensionless Parameters		
Plasma Beta	β	~1
Lundquist Number	S	10^3
Mach Number	M_S	~1
Alfvén Mach Number	M_A	~1
Hall Parameter	L/d_i	~1

Table 3.1: Summary of plasma parameters measured with the Langmuir probe and Flux Array 2. Measurements collected during a 25 μs interval starting from energization of drive coils.

The evolution of the magnetic field configuration was measured using two arrays of B-dot coils, as described in Sections A.1 and A.2. The yellow shaded region in Fig. 3.1(**a**) indicates the area covered by Flux Array 1, an array composed of 96 pick-up coils that only measure dB_z/dt. The blue shaded region in Fig. 3.1(**a**) denotes the volume scanned by

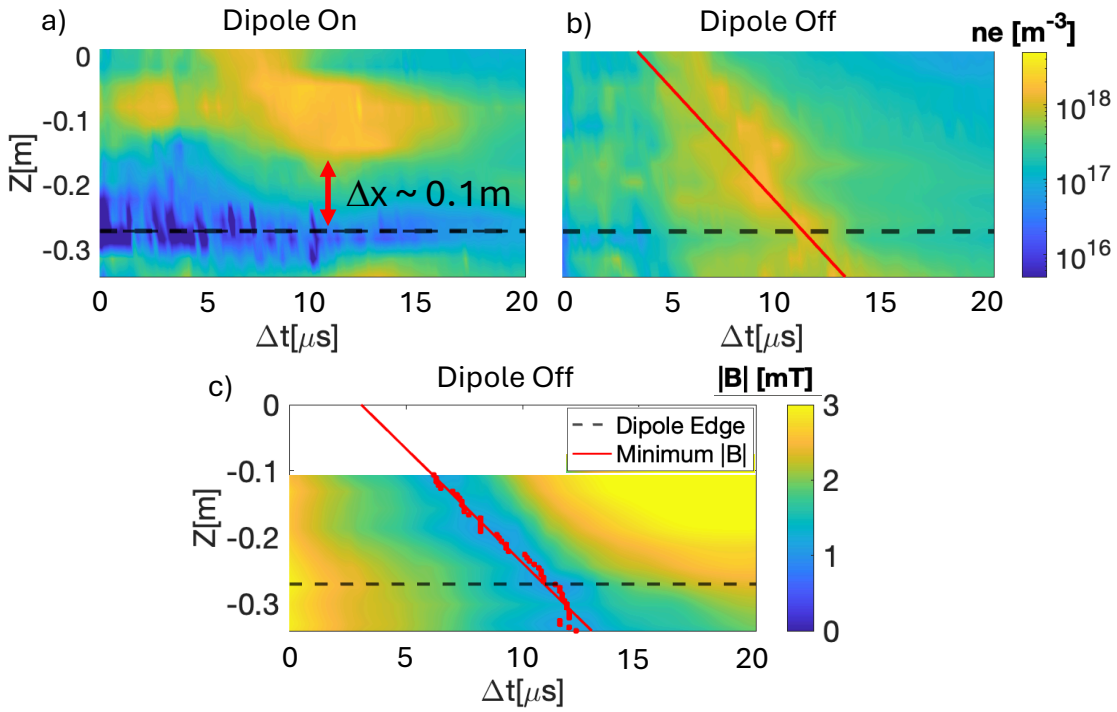

Figure 3.2: Using the Te probe, panels (a) and (b) show plasma density measurements with the dipole on and off, respectively. The rise in plasma density on the windward side indicates the location of the magnetopause current layer, approximately 0.1 m from the dipole edge. Panel (c) shows magnetic field measurements along the same path measured by the Te probe. The slope of the minimum B line provides a value for the plasma flow velocity, while the

Flux Array 2, which consists of 256 coils measuring all components of $d\mathbf{B}/dt$.

The time evolution of the magnetic field was reconstructed by scanning Flux Array 2 along the Z-axis in 0.03 m increments across 24 separate discharge events. Each discharge began with the activation of the plasma guns, followed by the energization of the dipole. The subsequent drive coils' energization coincides with the peak dipole current, defining $\Delta t = 0$. By scanning Flux Array 2 along the Z-axis a volumetric map of $d\mathbf{B}/dt$ was generated, providing high spatial and temporal resolution of the evolving magnetic field.

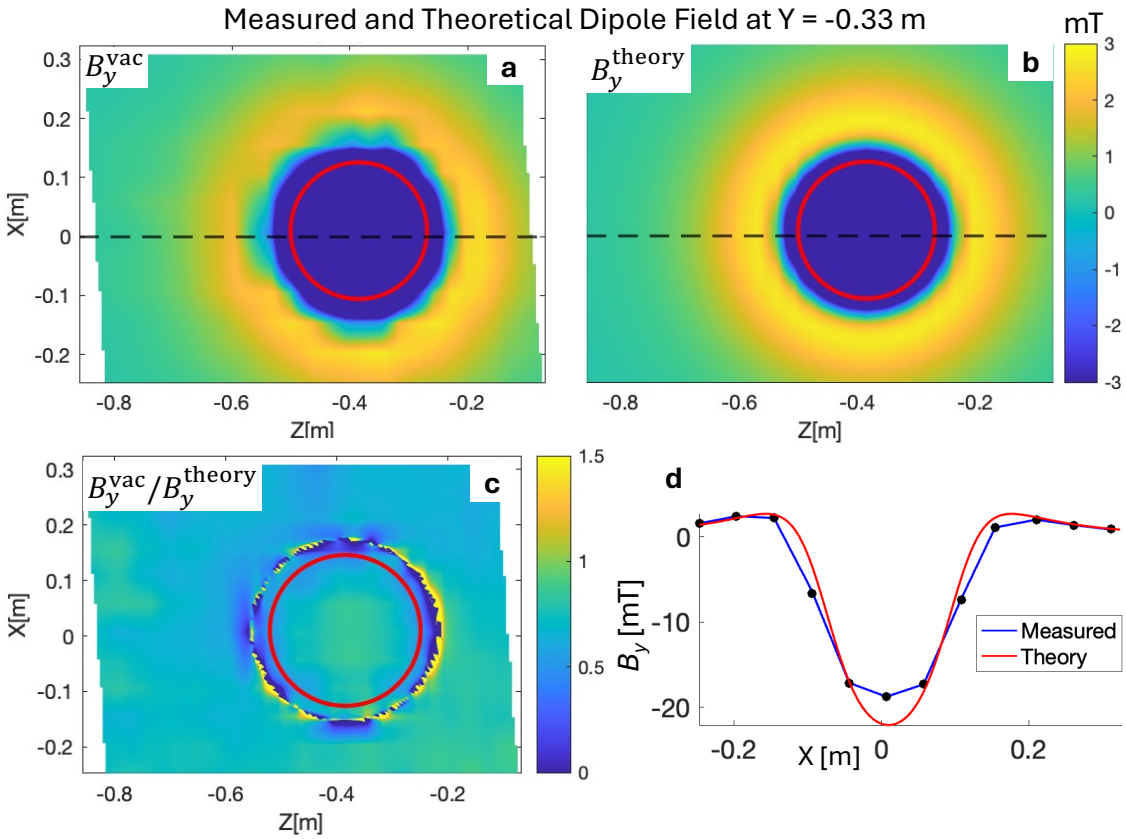

Figure 3.3: Panel **a** is a slice at the Y = 0.33 m plane using the measured data from Flux Array 2, and panel **b** is the same plane using the theoretical dipole data scaled by the dipole current, with the red circle indicating the dipole location. By using the plane Y = 0.33 m, which is offset from the location of the dipole at Y = 0.39 m, direct measurements from Flux Array 2 can be compared to the theoretical data. Panel **c** demonstrates the ratio of the two data sets is near unity. Panel **d** is a line trace along the dashed line in **a** and **b**, showing the spatial alignment of the data sets. These scaling and alignment techniques were repeated for the YZ and XY plane, and all components of **B**.

3.2 Increasing the Spatial Resolution of B

Magnetic fields interpolated onto a sub-centimeter grid were obtained by replacing the measured vacuum field, $\mathbf{B}_{\text{vac}}$, with a high-resolution theoretical field, $\mathbf{B}_{\text{theory}}$. A comparison between the measured and theoretical vacuum fields in the XZ plane is shown in Fig. 3.3. Their agreement is highlighted in panels **c**–**d**, where the ratio of the fields in panel **c** remains close to unity, except where the fields transition through zero. At these locations, the theoretical field vanishes causing the ratio to diverge. The line trace in panel **d** demonstrates

good spacial agreement between the two datasets.

Using $\mathbf{B}_{vac}$ and $\mathbf{B}_{theory}$, the vacuum removed field, $\mathbf{B}_{vr}$, was found from

$$\mathbf{B}_{vr} = \mathbf{B}_{wp} - \left(\frac{I_{wp}}{I_{vac}}\right)\mathbf{B}_{vac} \quad ,$$

where $\mathbf{B}_{wp}$ is the magnetic field with plasma present. The scaling factor, I_{wp}/I_{vac}, (which is the dipole current with plasma present divided by the dipole current in vacuum) accounts for the induced field produced by the dipole due to the energization of the drive coils. $\mathbf{B}_{vr}$ is mainly caused by the currents in the plasma without the sharp variations of the dipole coil. By isolating this component it can be accurately interpolated to high spatial resolution. The theoretical dipole field, $\mathbf{B}_{theory}$, is calculated using Biot-Savart's law and then added separately with arbitrary high spatial resolution.

The reconstructed magnetic field, $\mathbf{B}_{ta}$, is then

$$\mathbf{B}_{ta} = \mathbf{B}_{vr} + \langle I_{wp} \rangle_z \mathbf{B}_{theory} \quad ,$$

where $\langle I_{wp} \rangle_z$ is the dipole current as a function of time, recorded with plasma present and averaged over all plasma discharges.

3.3 Dipole Skeletal Structure

A powerful analysis method for interpreting 3D magnetic field configurations is defining the topological or skeletal structure [83]. This structure consists of: separatrix surfaces that divide distinct magnetic flux domains; magnetic null points where the magnetic field vanishes; and separators (or X-lines), continuous lines connecting nulls and arising from the intersection of separatrix surfaces [46].

The magnetic skeletal structure is revealed by initiating streamlines throughout the measured domain and categorizing them into three classes:

1. **Open field lines** ($N = 0$)**:** Field lines that do not pass through the dipole.

2. **Passing field lines** ($N = 1$)**:** Field lines that pass through the dipole once.

3. **Looped field lines** ($N > 1$)**:** Field lines that loop around the dipole, passing through the dipole multiple times.

These classes of field lines were identified using two complementary methods. The first utilizes a full volumetric classification of magnetic field line connectivity within the measured domain. Each point was grouped into one of three categories based on the number of times its associated streamline crossed the dipole plane: zero ($N = 0$), once ($N = 1$), or more than once ($N > 1$). The resulting transition boundaries between these regions form separatrix surfaces. In Fig. 3.4(**a**), the shaded blue region indicates field lines that intersect the dipole plane, with the solid blue line marking the $N = 1$ transition. The procedure was repeated by identifying streamlines in the direction anti-parallel with **B**, Fig. 3.4(**b**), yielding the red $N = 1$ boundary. The combination of both boundaries delineates all four separatrix surfaces, shown in panel **c**. This method offers a straightforward approach to locating the magnetic separator and its associated null points, but does not distinguish between the four separatrix surfaces.

The second method isolates each separatrix surface individually by restricting the search to specific spatial paths (elliptical arcs or radial lines). As shown in Fig. 3.4(**d**), the $N = 0$ surface is determined by iteratively performing a binary search along elliptical arcs, distinguishing between streamlines that do or do not intersect the dipole plane. Similarly, the transition between $N = 1$ and $N > 1$ is resolved along radial lines, Fig. 3.4(**e**), where the transition point is bracketed between streamlines that loop around the dipole multiple times and those that pass through the dipole plane once. In the example, streamline 5 (red line) marks the final iteration, yielding the boundary between the $N > 1$ (red line) and $N = 1$ (black line) regions. To fully resolve the separatrix surfaces, both searches were iterated 40 times, revealing the surfaces outlined by the black and yellow lines in

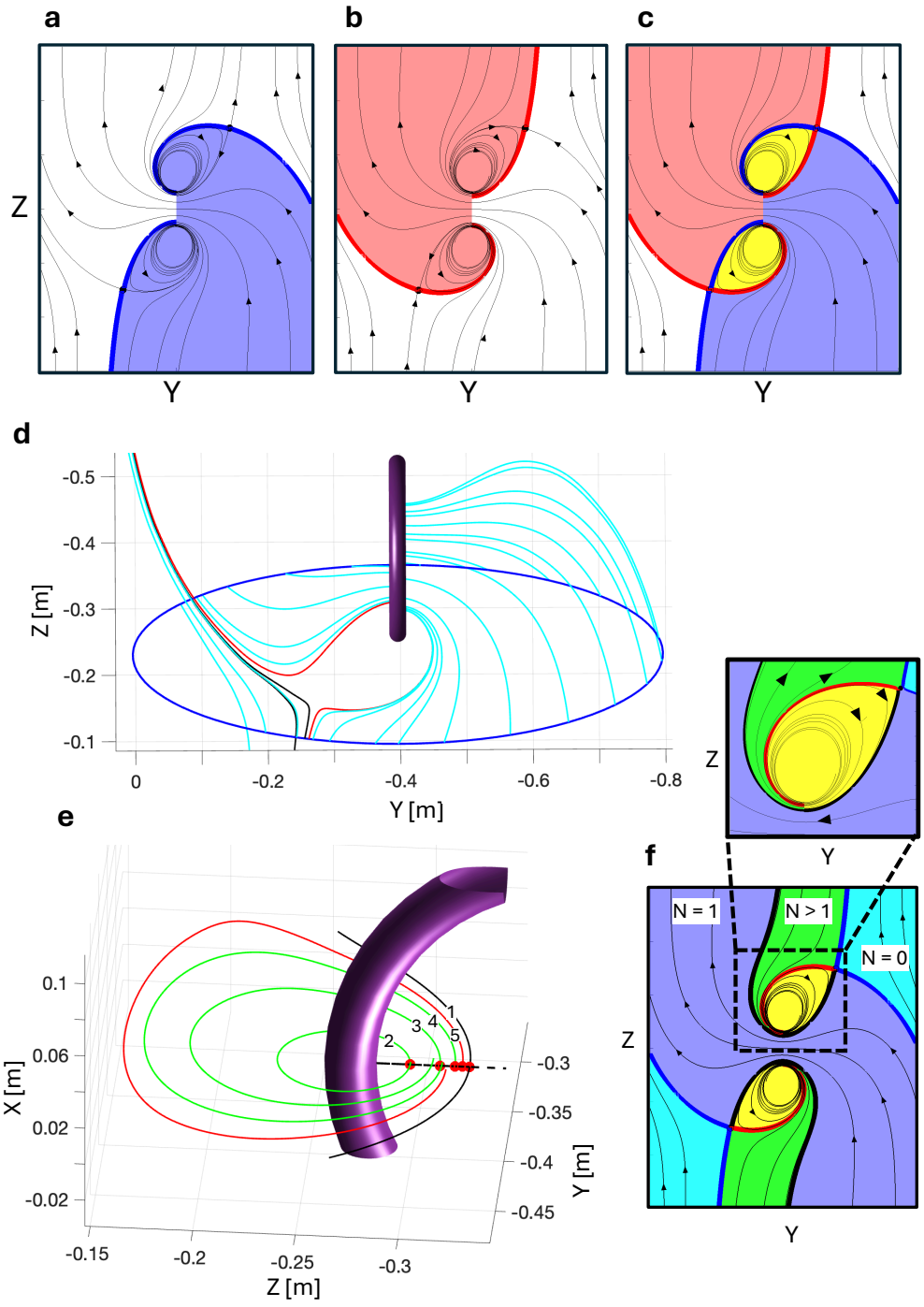

Figure 3.4: Panel **a**–**c** define the N = 1 transition by initiating streamlines in the entire measured domain. Panel **a** used streamlines parallel to **B**, while panel **b** used streamlines anti-parallel to **B**. Combining these gives the complete skeletal structure shown in panel **c**. Panels **d**–**f** describe a second binary method that distinguishes each separatrix surface. This second method is used two different ways as shown in **d** and **e**. Panel **d** shows how the N = 0 surface is identifying by initiating streamlines along an elliptical curve. Panel **e** shows the binary search along a radial line inside the dipole plane that finds the boundary between N = 1 field lines and N > 1 field lines, where the numbers identify the iteration within the search.

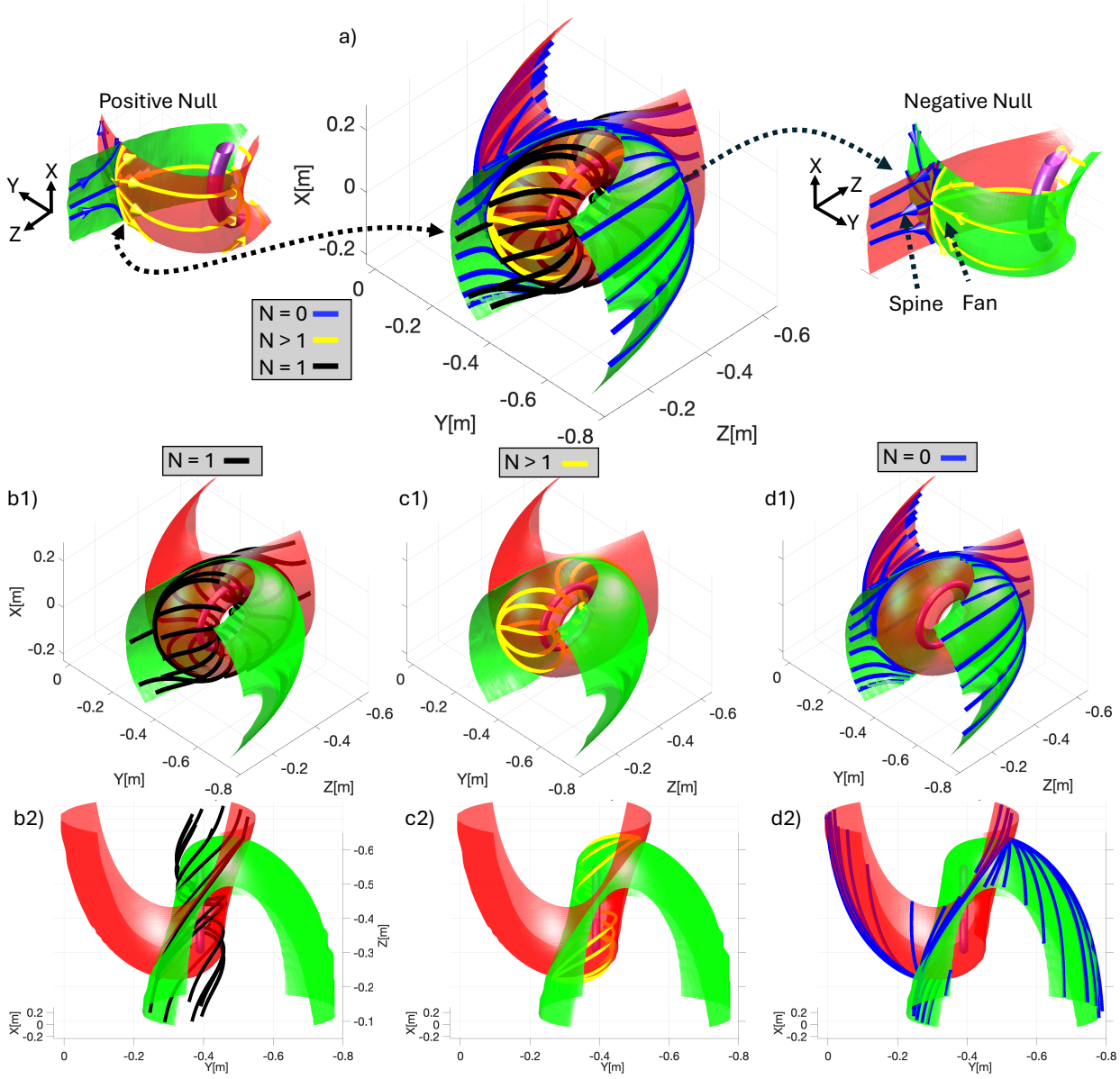

Figure 3.5: All separatrix surfaces of the min-magnetopause are differentiated, with every panel showing the red and green N = 1 transition surfaces, as described in Fig. 3.4(a–c). The complete skeletal structure is given in panel (a), with the left and right inset panels detailing the positive and negative null structures. The distinct separatrix surface are illustrated by two different view angles in rows 1 and 2, with panels (b –c) identifying the blue, black and yellow lines for the N = 0, N = 1, and N >1 separatrices, respectively.

Fig. 3.5(columns **b**, **c**). The inset panel of Fig. 3.4**f** shows how the $N > 1$ surface is defined by the looped portion of the streamline starting from the dipole plane. This last looped line defines the separatrix surface, distinguishing the green $N > 1$ region from the yellow $N > 1$ region (inset panel of Fig. 3.4**f**), and completing the X-point geometry. The 3D separatrix surfaces are then found by repeating the elliptical and radial path searches at different toroidal angles around the dipole center.

These methods yield the complete skeletal structure shown in Fig. 3.5**a**, with the inset panels identifying the positive and negative null configurations. Comparing the two null structures, one is able to see how the separatrix surfaces that the spine and fan field lines lie on interchange between the positive and negative nulls. In addition, the separator is identified by the intersection of the red and green surfaces, with the null points identified by the point along the separator where the component of **B** vanishes.

3.3.1 Bifurcation of the Dipole Skeletal Structure

Schematic Model

Before analyzing the dynamics of the more complicated 3D magnetic structures recorded in the experiment, we first elucidate the expected topologies through simplified prescribed fields shown in Fig. 3.6(rows **a**,**b**). Here, a vacuum dipole field is superimposed with an idealized reconnection field. The latter is constructed from a translationally symmetric vector potential,

$$A_x(x, y, z) = \gamma(\sigma z_p^2 - y_p^2) \quad ,$$

where $\sigma = 0.2$ sets the opening angle of the X-point geometry, and $\gamma = 5.2 \times 10^{-2}\,\mathrm{T/m}$ is a scaling factor. The reconnection layer's orientation and position are defined by the

constants θ, ΔY, and ΔZ in the rotated coordinates

$$z_{\text{layer}} = z\cos\theta - y\sin\theta - \Delta Z \quad ,$$

$$y_{\text{layer}} = -z\sin\theta + y\cos\theta - \Delta Y \quad .$$

The corresponding X-point field configuration is then given by $\mathbf{B} = \nabla \times \mathbf{A}$. Combining the idealized reconnection layer field with the vacuum dipole field yields the skeletal structure with the red and green separatrix surfaces, the separator traced by a black dashed line, and magnetic nulls marked by white (positive) and blue (negative) stars, as shown in Fig. 3.6.

The evolution of this system shows the reconnection layer propagate toward the center of the vessel, with the associated magnetic field reversal modifying the angle between the background and dipole fields. A simplified illustration of this process is shown in Fig. 3.6, with row **a** depicting a 3D rendering and row **b** showing the associated mid-plane slice. These schematics describe the interaction between the reconnection layer separatrices (dashed red line) and the dipole separatrix surfaces (green and red lines), offering a conceptual view for a domain larger than that diagnosed in the experiment.

The initial motion of the reconnection current layer toward $Y = 0$ drives the green dipole separatrix surface toward the red surface over the range $\Delta Y = 0.3\,\text{m}$ to $\Delta Y = -0.03\,\text{m}$, where ΔY denotes the displacement of the reconnection X-point from the dipole plane located at $Y = 0.39\,\text{m}$. By $\Delta Y = -0.06\,\text{m}$, the windward side of the dipole becomes embedded within the reconnection exhaust, where the local background field is parallel to the dipole moment. In contrast, the angle between the background and dipole fields on the leeward side remains largely unchanged. Once the background field surpasses the angle parallel to the dipole moment, the magnetic null on the windward side inverts from positive to negative. The inversion births a positive-negative null pair, Fig. 3.6(**a3**), constituting a topological bifurcation that conserves the topological degree [36]. Further movement of the layer causes the background field to rotate beyond the dipole moment direction, driving

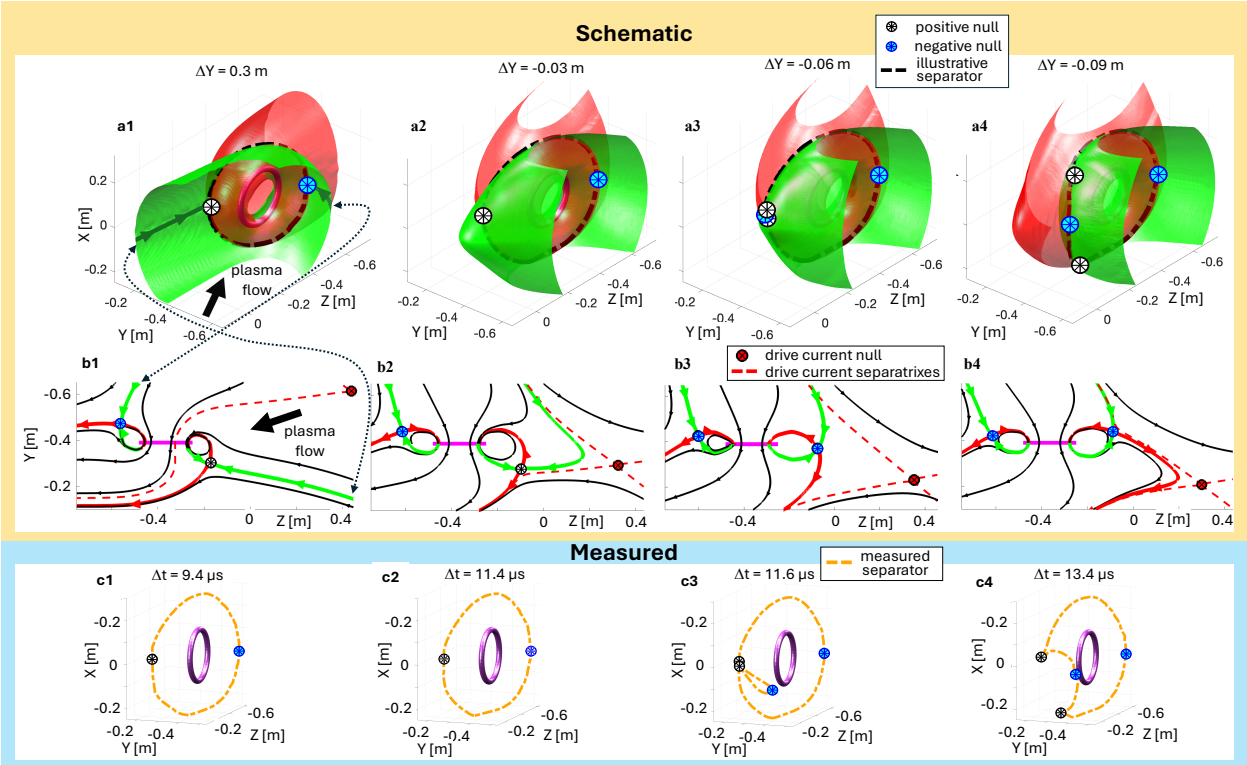

Figure 3.6: Rows **a** and **b** illustrate the dynamics of the expected separator with an idealized reconnection current layer at various displacements, ΔY, from the dipole plane ($Y = 0.39\,\mathrm{m}$). In row **a**, the green and red surfaces represent the separatrices that define the dipole topology. Row **b** shows the YZ mid-plane of row **a** with corresponding field lines and the idealized reconnection separatrices (red dashed line). As ΔY decreases from $-0.3\,\mathrm{m}$ to $-0.03\,\mathrm{m}$, the background magnetic field rotates, driving the green separatrix toward the red separatrix. This leads to a bifurcation in the magnetic topology and the formation of new nulls in **a3** and **b3**. The motion of the windward null point (panels **b2** through **b4**) causes the null point geometry to align with the direction of the dominant flux flow **b4**. Notably, the illustrative separator (row **a**, black dashed line) smoothly evolves, while the measured separator (row **c**) spontaneously changes its shape to the elongated form in panel **c3** (orange dashed line). The immediate elongation arises from the magnetic topology's sensitivity to small changes in the magnetic field, as discussed further in section 3.3.1.

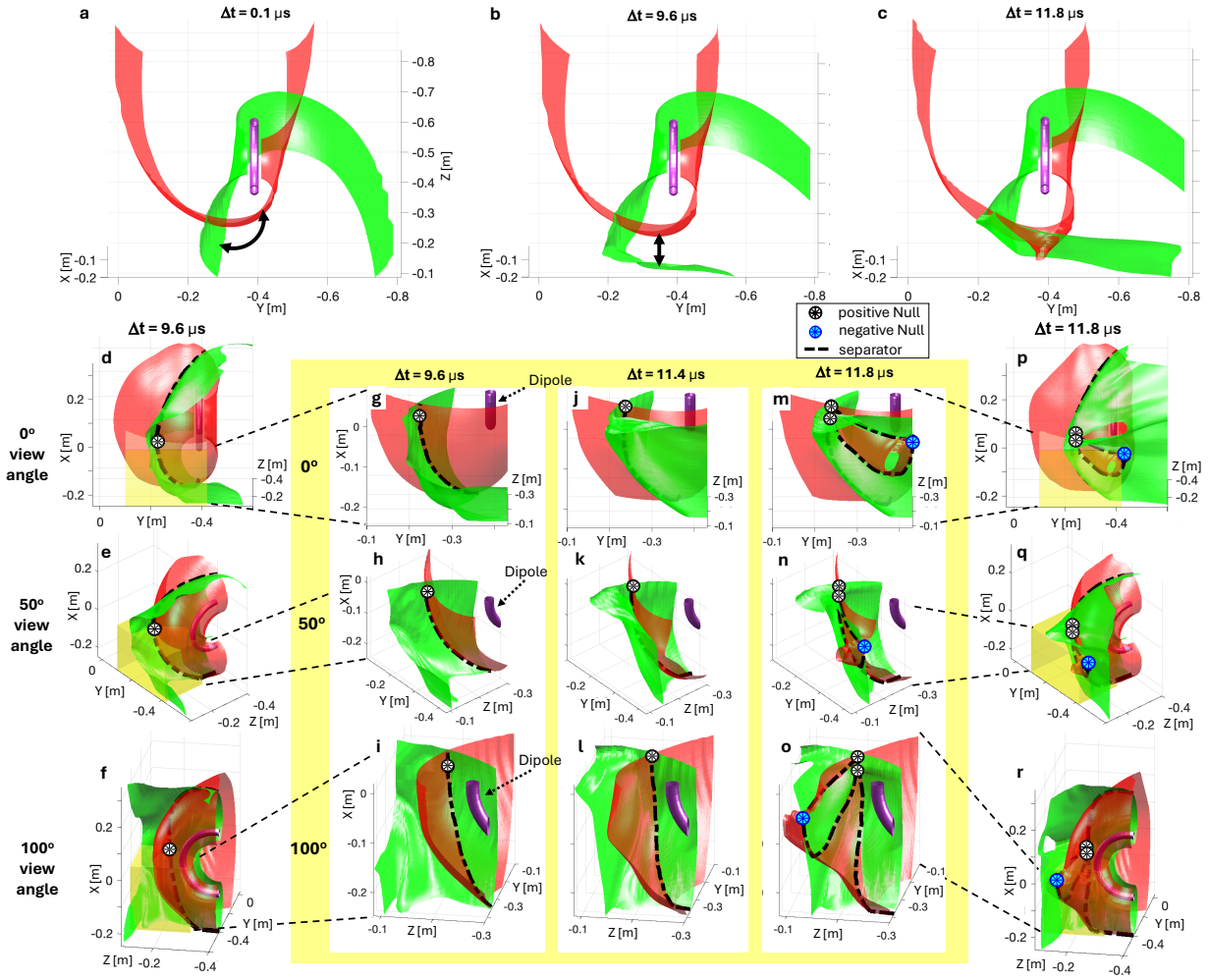

Figure 3.7: Similar to row **a** of Fig. 3.6, panels **a** and **b** show separatrix surfaces being driven toward one another, with there subsequent crossing in panel **c**. Panels **g**–**o** present a zoomed-in view of the yellow region in panels **d**–**f** and **p**–**r**, with each row corresponding to a different viewing angle. The surfaces move due to a combination of plasma pressure and the change in angle between the dipole and background magnetic field. The intersection of the surfaces, shown in panels **m**–**o**, leads to a bifurcation in the magnetic topology. The bifurcation, occurring at $\Delta t = 11.8\,\mu s$, increases the number of magnetic nulls in the skeletal structure from two to four, with the emergence of two new nulls visible in panels **m**–**q** (marked by white and blue stars). Concurrent with null formation, the bifurcation adds an entirely new section to the separator (black dashed line), as evident from the change in the separator's shape between the $\Delta t = 11.4,\mu s$ and $\Delta t = 11.8,\mu s$ columns.

the negative nulls toward the leeward side, Fig. 3.6(**a4**).

Measured Bifurcation

A comparison between the schematic and measured separators, during the bifurcation process, is shown in Fig. 3.6(row **a**, **c**). In the schematic version, panel **a3**, new nulls form near the original null. In contrast the measured separator, panel **c3**, spontaneously forms a new null $\sim 0.2\,\mathrm{m}$ from the original null. This difference arises from large portions of separatrices being driven toward one another, shown in Fig. 3.7. The converging of these surfaces forms a broad area of magnetic topological instability, contrary to the local region formed in the schematic version.

A detailed analysis of the experimentally observed bifurcation process is presented in Fig. 3.7, where panels **a** – **c** show the green separatrix surface being driven toward the red separatrix. In the panels of the yellow region, the convergence of the separatrix surfaces is shown as a time sequence for three different perspectives. As the surfaces approach each other, an unstable magnetic configuration emerges, in which a small magnetic perturbation can trigger a topological transition in the system's skeletal structure [84]. The resulting bifurcation creates two additional magnetic nulls that extend the separator, allowing reconnection to initiate over a larger spatial extent. Such large-scale reconfigurations may be important for triggering rapid 3D reconnection in natural and laboratory plasmas.

3.4 Mapping the Separator to the Dipole Plane

By a similar approach applied to evaluating the reconnected flux in active regions on the sun [56], the reconnected flux crossing the separator was measured using the relatively constant magnetic field in the dipole plane. This was accomplished by mapping the separator's position onto the dipole plane, as illustrated in Fig. 3.8(**a**). Here, black lines represent magnetic field lines on the $N = 1$ separatrix, and the magenta line, which forms

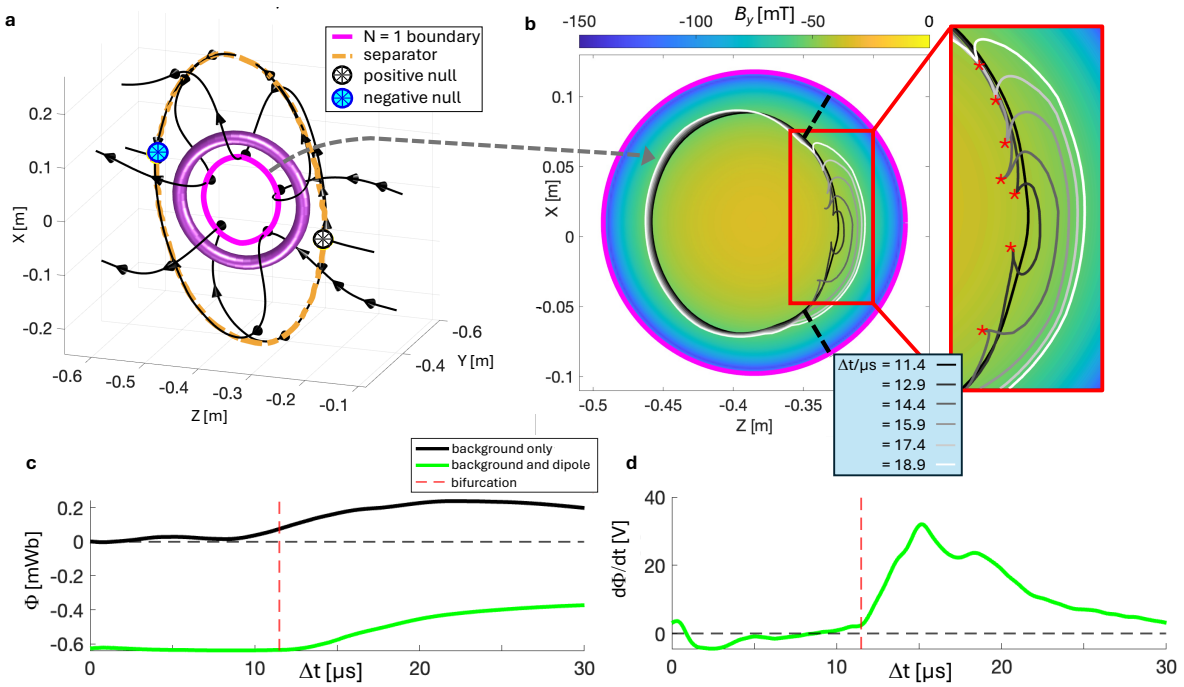

Figure 3.8: Panel **a** shows the N = 1 field lines mapped from the separator (dashed orange line) to the dipole plane to form the N = 1 boundary (magenta line). Panel **b** shows the evolution of the N = 1 boundary in the dipole plane starting just prior to the system bifurcating, $\Delta t = 11.4\,\mu s$. The red stars in the inset panel indicate points that map to the positive nulls that form after the bifurcation. Panels **c** and **d** are plots of the B_y flux, Φ, and it's rate of change, $d\Phi/dt$, with the dipole on (green line) and off (black line). The flux is the integrated B_y field in the area bounded by the N = 1 boundary, the dipole edge (magenta line) and the black dashed lines (as shown in panel **b**). The red dashed lines in panels **c** and **d** mark the moment of bifurcation, revealing a delay in the increase of flux through the dipole plane (green line) when compared to the case with only the background field (black line). Panel **d** further shows that the rise in the flux rate of change coincides with the bifurcation event.

the N = 1 boundary, marks their intersection with the dipole plane. Since the black N = 1 field lines trace back to the separator (orange dashed line), the motion of the N = 1 boundary reflects the motion of the separator. This evolution is depicted in Fig. 3.8(**b**) using gray-scale lines that represent different points in time of the N = 1 boundary. The emergence of a bulge, in conjunction with the cusp-like features (indicated by red stars), corresponds to the reshaping of the separator and the birth of new null points, respectively.

A further demonstration of the connection between the N = 1 boundary and the

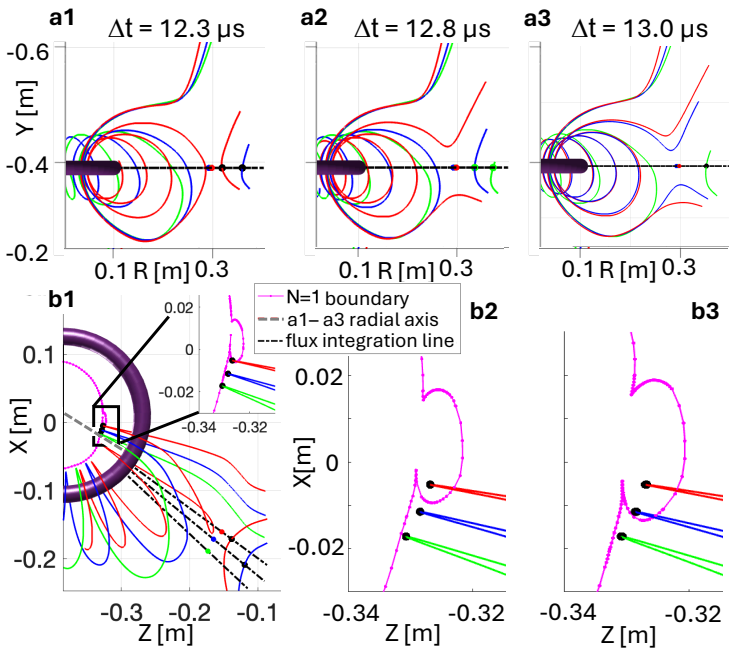

Figure 3.9: These panels illustrate how changes in field line connectivity at the X-point map to the dipole plane, allowing flux changes along the separator to be measured in the dipole plane. At $\Delta t = 12.3\,\mu s$, column 1 panels, streamlines are initiated at fixed points in the dipole plane at radii greater than the $N = 1$ boundary, as shown in the inset view of panel **b1**. The radial axis of row **a** is indicated by the gray dashed line originating at the dipole center in panel **b1**. Panel **a1** shows all inflow field lines starting in the dipole plane are looped. From $\Delta t = 12.3\,\mu s$ to $12.8\,\mu s$, the topology of the red field line changes from an in-flowing looped field line to an out-flowing passing field line. Within the dipole plane, this transition corresponds to the fixed starting point shown in **b2** transitioning to a radius less than the $N = 1$ boundary. The panels in column 3 show the same transition for the blue field line.

separator is seen in Fig. 3.9, where panel **b** shows streamlines initiated from fixed points within the dipole plane. These streamlines begin at radii greater than the $N = 1$ boundary, allowing changes in field line connectivity to be tracked relative to this evolving boundary. As time progresses from $\Delta t = 12.3$ to $\Delta t = 12.8\,\mu s$, the $N = 1$ boundary expands outward, eventually encompassing the fixed point of the red streamline. This corresponds to a transition in the field line's topology from a looped $N > 1$ configuration to a passing $N = 1$ configuration. This transition in the dipole plane correlates to a connectivity change at the X-point, depicted in the panels of row **a**. Combining the views of rows **a** and **b** highlights

the direct relationship between field line connectivity at the X-line and the $N = 1$ boundary.

3.5 Measuring the Global Reconnection Rate

Having established that changes in field line connectivity at the separator map to the dipole plane, Faraday's law can be invoked to evaluate the global reconnection electric field along the separator as

$$\oint E_{rec}\, dl = -\frac{d\Phi}{dt} \quad , \tag{3.1}$$

where $\Phi = \int \mathbf{B} \cdot d\mathbf{a}$ is the magnetic flux enclosed in Fig. 3.8(**b**) by the $N = 1$ boundary (grayscale lines), the edge of the dipole (magenta line), and the two radial black dashed lines. The term E_{rec} refers to the component of the inductive electric field along the separator [87, 40].

By restricting the flux integration domain to the region bounded by the two black lines in Fig. 3.8(**b**), the effect of the dipole current varying ~15% over the 25 μs duration of the experiment was minimized. This ensures that the calculated change in flux primarily reflects the reconnection associated with the motion of the N=1 boundary, rather than the varying dipole strength.

The reconnected flux and global reconnection rate, calculated from equation 3.1, are plotted in Fig. 3.8(**c**, **d**), respectively. In these plots, the green lines correspond to measurements with the dipole on while the black line is from measurements with the dipole off. A comparison of these conditions demonstrates that the dipole causes a delay in the rise of flux flowing through the dipole plane. This delay is attributed to a magnetic flux pile-up that generates an accumulation of magnetic energy prior to the onset of reconnection. The associated rapid increase in $d\Phi/dt$, occurring at 11.5 μs, can be seen in panel **d**, and correlates with the bifurcation process described in Fig. 3.7, which is marked by the vertical red dashed line in Fig. 3.8(**c**, **d**).

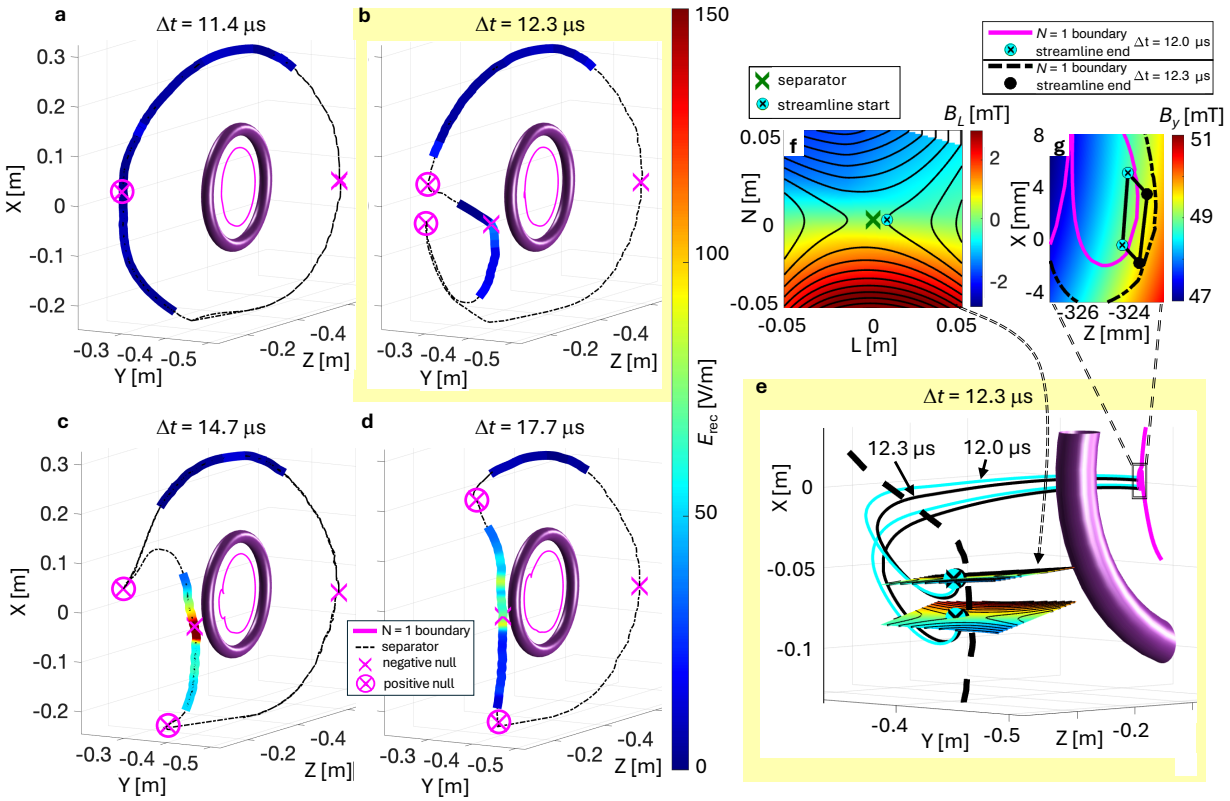

Figure 3.10: The evolution of the separator is shown in **a**–**d**, with colored sections indicating the magnitude of E_{rec}. Prior to the bifurcation (panel **a**), E_{rec} is approximately 5 V/m, and the windward side of the dipole contains a single positive null. After the bifurcation (panels **b**–**d**), the reconnection rate rapidly increases to approximately 200 V/m near the newly formed negative null (panel **c**). The procedure for calculating E_{rec} is illustrated in panels **e** and **f**. By selecting planes perpendicular to the separator (panel **f**) the geometry of the reconnection magnetic field is determined. The coordinate system used in panel **f** follows the convention employed in spacecraft data: L is aligned with the B_{rec} direction, N corresponds to the plasma inflow direction, and M is along the separator [15]. Using two planes separated by a distance l, streamlines are initialized 5 mm from the X-point in the outflow region at the time $\Delta t = 12.0\,\mu s$ (cyan lines in panel **e**). The inset view of panel **g** shows the intersection point field lines make with the dipole plane relative to the $N = 1$ boundary (magenta and black dashed lines). Repeating this process at a later time $\Delta t = 12.3\,\mu s$ yields the black streamlines in panel **e** and their corresponding intersection points in panel **g**. The area δa swept out by the motion of the separator over the time interval $\delta t = 0.3\,\mu s$ forms the tetrahedron in panel **g** (black lines). Due to the magnetic field in the dipole plane remaining constant over δt, the rate of change of magnetic flux, $d\Phi/dt$, is determined by equation 3.3 using the flux through the tetrahedron at $\Delta t = 12.3\,\mu s$. Dividing $d\Phi/dt$ by the separation l between the planes gives the value of E_{rec} along the separator at $\Delta t = 12.3\,\mu s$.

3.6 Fast Reconnection Triggered by Null Point Bifurcation

Fast 2D magnetic reconnection is characterized by an inflow velocity of magnetic flux into the diffusion region, v_{in}, that approaches a significant fraction of the Alfvén speed, $v_A = B_{rec}/\sqrt{\mu_0 m_i n}$, where B_{rec} is the reconnecting magnetic field, m_i is the ion mass, and n is the plasma number density. Fast reconnection is typically quantified by the normalized reconnection rate, $\alpha = v_{in}/v_{out}$, when values reach $0.01 < \alpha$ [3, 90]. Furthermore, a normalized reconnection rate much larger than 0.1 is common in kinetic simulation and experiment [55, 38] of electron-only configurations [75]. Using Faraday's law, α can be equivalently expressed as

$$\alpha = \frac{E_{rec}}{v_A B_{rec}} \quad . \tag{3.2}$$

Unlike the global reconnection rate defined in Eq. 3.1, determining α requires evaluating local values of E_{rec} along the separator. This process is illustrated in Fig. 3.10(**e**–**g**), where planes perpendicular to the separator, Fig. 3.10(**f**), identify the local reconnecting magnetic field geometry. Streamlines are initialized in the outflow region 5 mm from the X-point such that their trajectories pass through the dipole plane. Figure 3.10(**e**) shows the mapping at two time intervals: cyan lines represent $\Delta t = 12.0\,\mu s$, and black lines represent $\Delta t = 12.3\,\mu s$. The intersections with the dipole plane in Fig. 3.10(**g**) form a tetrahedron, which represents the area, δa, swept out by the separator over the time $\delta t = 0.3\,\mu s$, from which the local reconnection electric field is inferred.

Due to the magnetic field in the dipole plane remaining approximately constant over the time δt, the change in magnetic flux $d\Phi/dt$ crossing the separator is calculated using the flux through the tetrahedron in Fig. 3.10(**g**). This follows by taking the time derivative of the magnetic flux, Φ, giving

$$\frac{d\Phi}{dt} = \int \frac{d\mathbf{B}}{dt} \cdot d\mathbf{a} + \int \mathbf{B} \cdot (\mathbf{v} \times d\mathbf{l}) \quad , \tag{3.3}$$

where $|\mathbf{v} \times d\mathbf{l}| \approx \delta a/\delta t$ is the area, δa, swept out by the separator in the time δt. In the dipole plane, the first term on the right side of equation 3.3 is approximately zero, reducing it to

$$\frac{d\Phi}{dt} \approx \frac{B_y^{in}\delta a}{\delta t} \tag{3.4}$$

where B_y^{in} is the field enclosed by the area δa. The reconnection electric field along the line segment, l, between the planes is then, $E_{rec} = \frac{d\Phi}{dt}/l$. This process was repeated for multiple line segments along the separator, generating a collection of area segments that follow the shape of the $N = 1$ boundary.

Fig. 3.10(**a**–**d**) shows the separator at different time points overlayed with values of E_{rec}, which correlates the bifurcation process to the reconnection electric field. Just prior to bifurcation, at $\Delta t = 11.4\,\mu s$, $E_{rec} \approx 5\,V/m$ then rises sharply to approximately $200\,V/m$ over a $3.3\,\mu s$ interval. The location of the peak value of E_{rec} is near the newly formed negative null point.

Δt [μs]	E_{rec} [V/m]	α
11.1 - 11.4	2 - 10	0.01 - 0.4
12.0 - 12.3	0.7 - 40	0.3 - 3
14.3 - 14.7	30 - 260	0.4 - 11
17.3 - 17.7	10 - 90	0.5 - 3

Table 3.2: Calculated values associated with Fig. 3.10(**a**–**d**), showing the range of normalized reconnection rates (α) along the separator during each corresponding time interval. Where E_{rec} and α have an approximate 30% and 50% error, respectively.

Using the local values of E_{rec}, the corresponding normalized reconnection rate, defined in Eq. 3.2, was estimated through a local 2D-like analysis. With the same planes used in the E_{rec} calculation, the reconnection geometry shown in Fig 3.10(**f**) enables the reconnection magnetic field to be estimated from the inflow magnetic field. This estimate gives $B_{rec} \approx 1.3\,mT$. The local Alfvén speed, measured with a Langmuir probe along the trajectory shown in Fig. 3.1, was in the range $v_A \approx 20$–$40\,km/s$. The resulting normalized reconnection rates for Fig. 3.10(**a**-**d**) are presented in Table 3.2. These values of α reach up to 11 (with an

experimental uncertainty of about 50%), which are two orders of magnitude greater than the established ion-coupled reconnection value of $\alpha \approx 0.1$. Thus, the onset of reconnection is consistent with electron-only dynamics, as expected at the present spatial scale ($\lesssim 1 d_i$).

3.7 Relating the Volumetric Current Density to E_{rec}

This system can be further characterized by relating the evolution of the current density to the reconnection electric field. Previous experiments [29] have observed a link between the reconnection electric field and the rate of change of the current density parallel to the separator, J_M. This relationship can be shown by combining Ampere's law, $\nabla \times \mathbf{B} = \mu_0 \mathbf{J}$, and Faraday's law, $\nabla \times \mathbf{E} = -\frac{\partial \mathbf{B}}{\partial t}$, which gives

$$\nabla \times (\nabla \times \mathbf{E}) = \mu_0 \frac{\partial \mathbf{J}}{\partial t}. \tag{3.5}$$

Using the vector identity $\nabla \times (\nabla \times \mathbf{E}) = \nabla(\nabla \cdot \mathbf{E}) - \nabla^2 \mathbf{E}$, and the assumption of quasineutrality (which means $\nabla \cdot \mathbf{E} = 0$), reduces equation 3.5 to

$$\nabla^2 \mathbf{E} = -\mu_0 \frac{\partial \mathbf{J}}{\partial t} \tag{3.6}$$

Solving for the E_{rec} component of equation 3.6 with the Green's function, $\nabla^2 \left(\frac{1}{|\mathbf{x} - \mathbf{x}'|} \right) = -4\pi \delta(\mathbf{x} - \mathbf{x}')$, and assuming the spatial and time dependence of the current density are independent, such that $J_M(\mathbf{x}, t) = J_M(\mathbf{x}) f(t)$, gives

$$E_{rec}(\mathbf{x}, t) = \frac{\mu_0}{4\pi} \frac{\partial f(t)}{\partial t} \int \frac{J_M(\mathbf{x}')}{|\mathbf{x} - \mathbf{x}'|} \, d^3\mathbf{x}'. \tag{3.7}$$

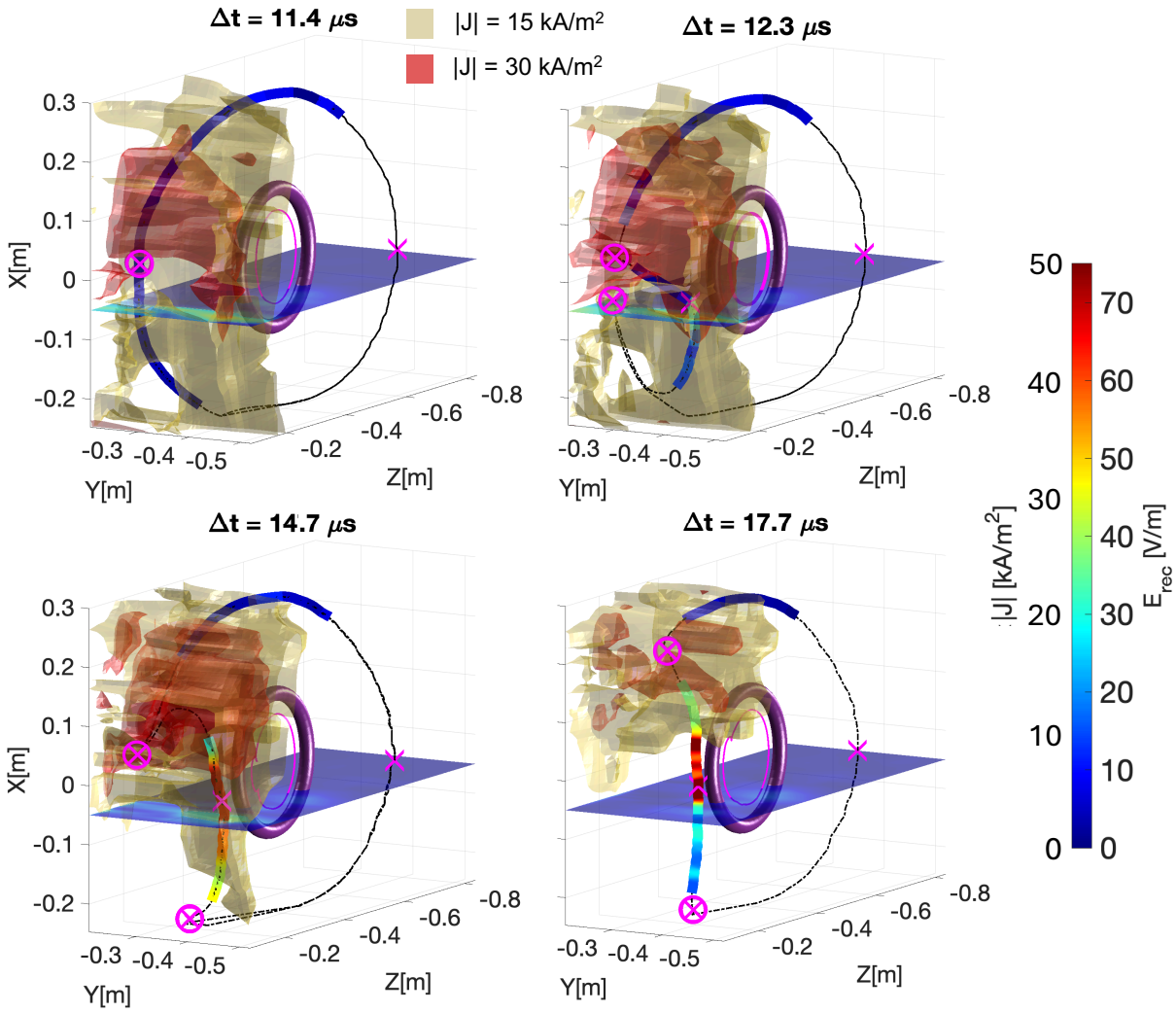

Figure 3.11: Isosurface of current density ($|\mathbf{J}| = \{15, 30\}\,\mathrm{kA/m^2}$), red and yellow surfaces respectively, with the reconnection electric field, $\mathbf{E}_{\mathrm{rec}}$, measured along the separator. $|\mathbf{J}|$ is also plotted as the color scale in the plane. Note the change in color scale of $\mathbf{E}_{\mathrm{rec}}$ as compared to Fig. 3.10.

Furthermore, when J_M changes in time with its spatial profile remaining near constant, an expression for its scalar strength can be written as

$$E_{rec} = \gamma J_M \frac{\partial f(t)}{\partial t} = \gamma \frac{\partial J_M}{\partial t}, \tag{3.8}$$

where γ is a constant.

The expected behavior predicted by equation 3.8 is observed when the evolution of

the current density is compared with the measured reconnection electric field. Owing to the 3D nature of the system, the spatial structure of the changing current density can be obtained by examining its iso-surfaces at $|\mathbf{J}| = \{15, 30\}\,\mathrm{kA/m^2}$, as shown in Fig. 3.11. These plots reveal an enhanced current density structure on the windward side of the magnetosphere, consistent with the formation of a magnetopause-like boundary. As time progresses, the current-density isosurfaces condense along the evolving separator, as seen at $\Delta t = 14.7\,\mu s$, and subsequently weaken by $\Delta t = 17.7\,\mu s$. In parallel with this evolution, E_{rec} initially increases in magnitude at $\Delta t = 12.3\,\mu s$ and remains elevated as the current density evolves between $\Delta t = 14.7$ and $17.7\,\mu s$.

This behavior is examined in greater detail in Fig. 3.12, where planes perpendicular to the separator are shown in conjunction with E_{rec} measured along the separator. Panels (a2–d2) illustrate that J_M within these planes dissipates over the time interval during which E_{rec} remains elevated. In these planes, it can be seen that while the magnitude of J_M decreases over time, the overall structure of the current density remains approximately constant, consistent with the assumption of spatial and temporal independence. Additionally, the magnetic tension visibly decreases during this period, as indicated by the X-point angle approaching 90°, suggesting that the system is relaxing from a higher energy state.

Calculation of the resistive heating generated by $\mathbf{J} \cdot \mathbf{E}$ along the separator further reveals details into the energy dissipation of the system. Using the same perpendicular planes employed to find E_{rec}, the corresponding current density component parallel to the separator, J_M, at the intersection point with the plane is used to compute the local power density, $W_M = E_{rec} J_M$. The results are shown in Fig. 3.14(a–d), where Δs denotes the distance along the separator, with $\Delta s = 0$ corresponding to the point closest to the T_e probe, located at $(X, Y) = (-0.02, -0.42)$ with variable Z. These plots show the power density increases immediately following the bifurcation process, indicating a rapid release of magnetic energy within a $\sim 5\,\mu s$ interval.

The T_e probe was positioned near the region of maximum power density, as indicated by

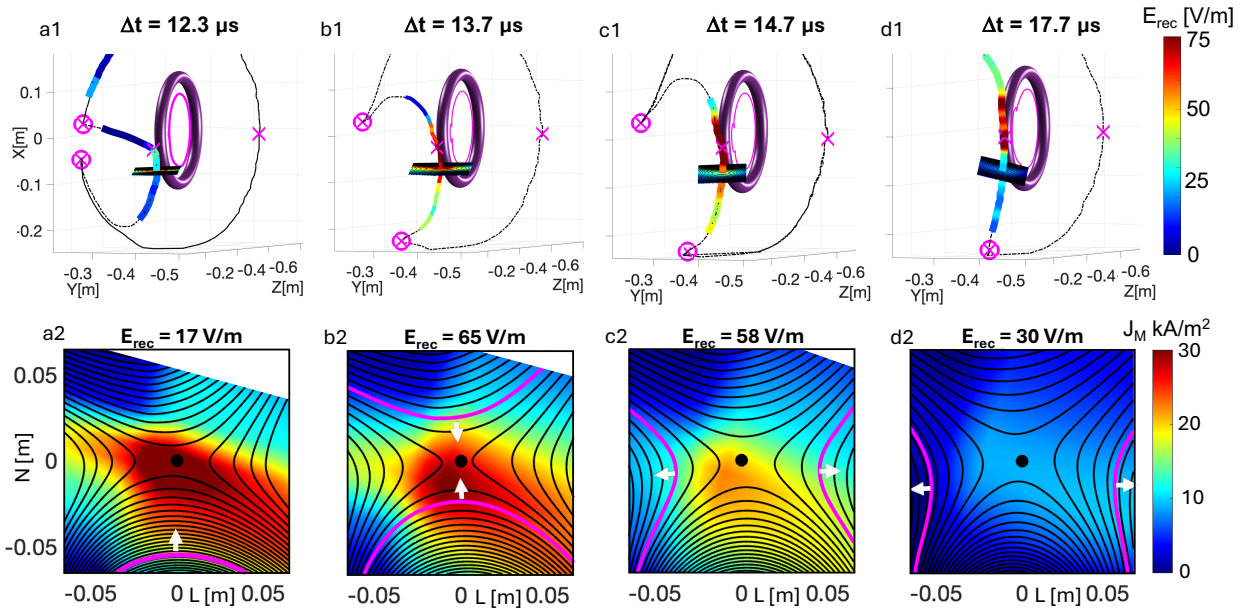

Figure 3.12: Perpendicular planes relative to the separator are shown in the first row. These panels compare the reconnection electric field, E_{rec}, with the current density component, J_M, parallel to the separator, which is plotted in the second row with the corresponding E_{rec} values stated in each title. The magenta contours are a constant flux value shared by each time point, demonstrating the evolution of the flux as reconnection progress over the time range.

minimum distance Δr in Fig. 3.14(a–d). The corresponding electron temperature measurements are presented in panels (e) and (f). The data show that T_e remains approximately constant at $\sim 15\,\text{eV}$ even as the resistive power density increases. This lack of measurable heating suggests that high electron velocity, which equates to a short transit times through the reconnection site, limits the conversion of magnetic energy into local thermal energy in this region. It should be emphasized, however, that the single-point measurement of T_e does not provide sufficient spatial information to draw definitive conclusions about the overall plasma energization. The intent here is to demonstrate that these limited measurements nonetheless correlate with the onset of fast reconnection initiated by a magnetic topological bifurcation.

Additionally, the location of the magnetopause can be identified using the current density **J**, as it coincides with the region of maximum **J** [89]. Using this criterion, Fig. 3.13

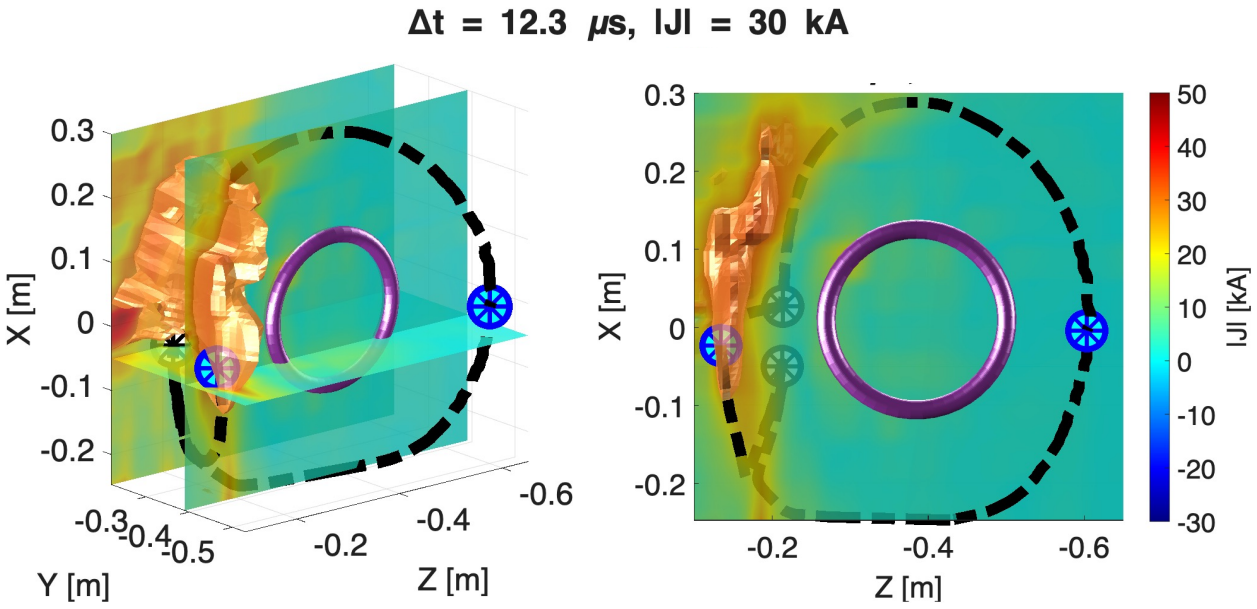

Figure 3.13: Magnetopause location identified by the current density maximum.

shows that the peak current density forms just after the bifurcation event. In this case, the magnetopause lies approximately 0.1 m from the dipole edge, in good agreement with the location inferred from the plasma density profile shown in Fig. 3.2.

3.8 Conclusion

From these experimental results, we propose a 3D mechanism to initiate magnetic reconnection, where a rotating background field drives a topological bifurcation that initiates a rapid onset of fast reconnection. Importantly, this mechanism does not rely on plasma instabilities such as the kink [8] or plasmoid [100] instability, but rather emerges from the geometric evolution of the magnetic topology. As a mechanism of this type has never been observed in 2D reconnection, these findings support the premise that 3D specific reconnection is fundamentally distinct from its 2D counterpart [84, 78, 39].

Given that 3D reconnection underpins energy release in environments ranging from solar flares to planetary magnetospheres, our results point toward topological bifurcation as the trigger mechanism of such explosive events. These observations indicate a new

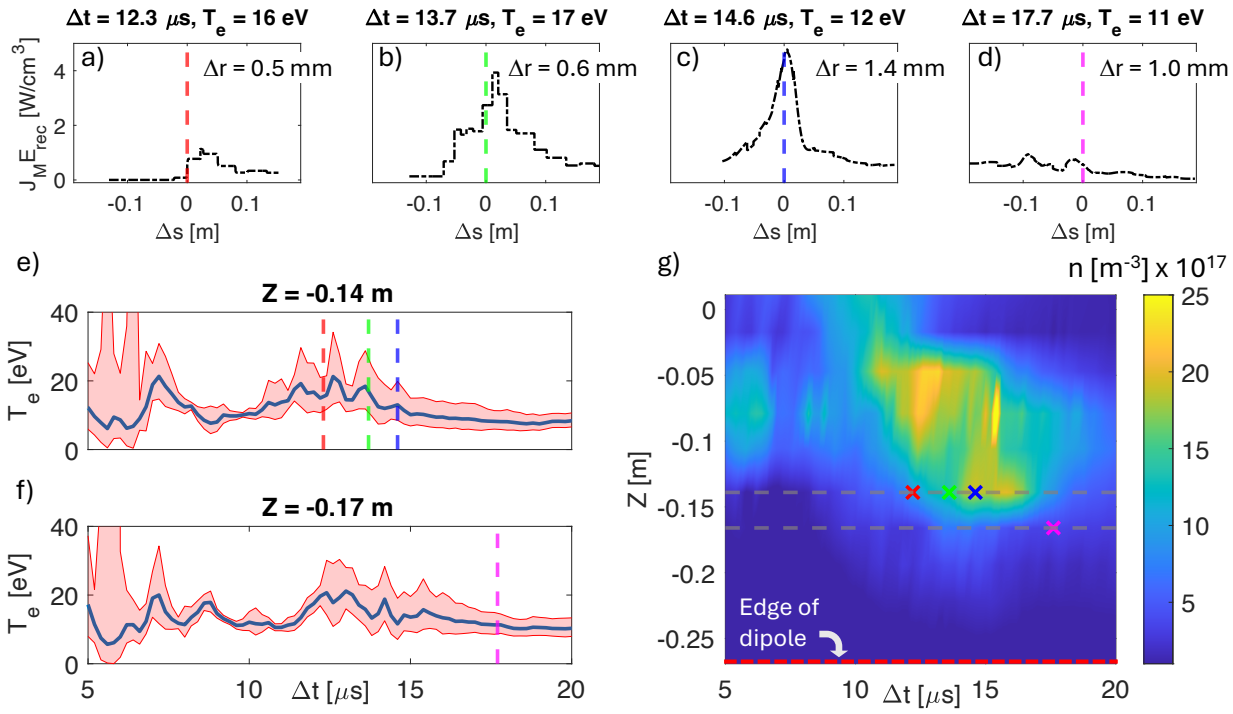

Figure 3.14: Using the measured J_M and E_{rec} profiles along the separator at the specified times, panels (a–d) show the resulting power density $W_M = E_{rec} J_M$. The distance along the separator, Δs, is measured from the point nearest to the T_e probe, while Δr denotes the distance between the closest point and the probe. Panels (e) and (f) are line traces of the T_e data taken at the two locations closest to the separator, with the colored dashed lines corresponding to the times when the separator and T_e probe are in closest proximity. Panel (g) shows the plasma density on the windward side of the dipole, where the edge of the high-density region aligns with the separator position, indicated by the colored x-symbols.

promising direction for both laboratory and spacecraft investigations of reconnection onset, where high resolution 3D mapping of evolving magnetic structures determine the onset of fast reconnection.

A APPENDIX A: DIAGNOSTICS AND PLASMA SOURCE

A.1 B-dot Probe

Changing magnetic fields are measured using pick-up coils, also referred to as B-dot probes (~ 0.01 m in length), constructed from printed circuit boards (PCBs), as shown in Fig. A.1. Each coil, oriented perpendicular to its surface area, measures the time derivative of the magnetic field in three orthogonal directions, $\dot{B}_1$, $\dot{B}_2$, and $\dot{B}_3$. Utilizing the ~ 1 mm width of the PCB, both $\dot{B}_1$ and $\dot{B}_2$ consist of seven loops spirally wound within the internal PCB layers. The $\dot{B}_3$ component uses four loops in total, with two printed on the top and bottom surfaces of the board. The PCB arrays are housed within vacuum-sealed alumina tubes, providing electrical and thermal insulation during the ~ 10 ms plasma exposure time.

Measurement of the changing magnetic field relies on the current induced as time-varying magnetic flux passes through a closed wire loop. The circuit used with the B-dot probes is shown in Fig. A.2. Here, R_1 represents the resistance of the probe wiring, while R_2 and R_s form a voltage divider that ensures the measured voltages at V_1 and V_2 remain within the input limits of the D-TACQ Solutions 2106 digitizers operating at 10 MHz. The resistor $R_p = 100\,\Omega$ is included to maintain a flat frequency response up to 7 MHz. To convert the

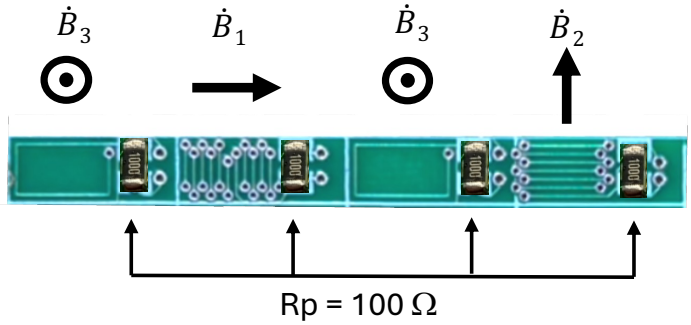

Figure A.1: The image shown is the PCB board with B-dot probes arrange as they are installed in a B-dot array probe.

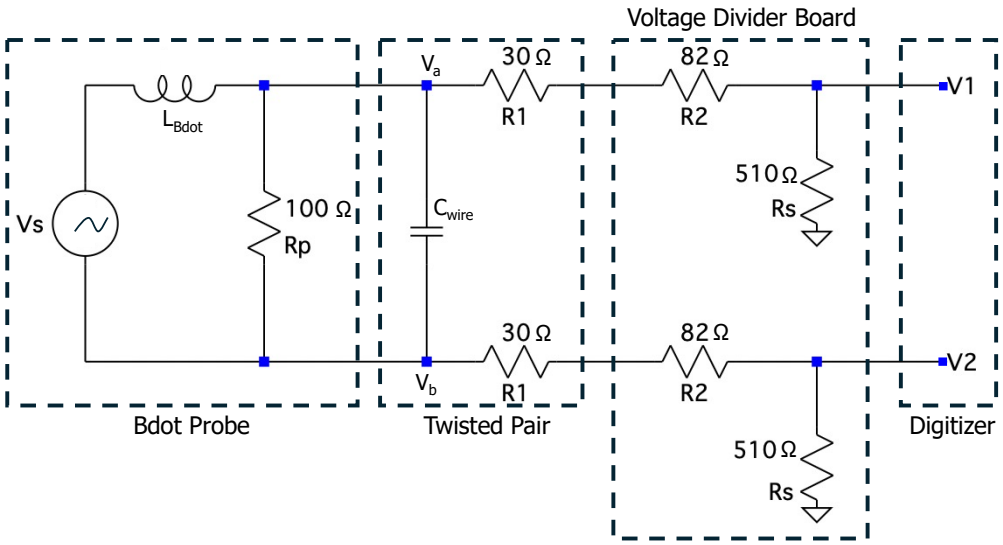

Figure A.2: Circuit diagram of a B-dot coil and its associated voltage divider connections. A difference in voltage between V_1 and V_2 is measured at the digitizer resulting in a signal with less noise.

induced electromotive force (emf), V_ϵ, into a B-dot signal, the following relations are used:

$$V_1 = DV_a, \quad V_2 = DV_b \quad , \tag{A.1}$$

where V_1 and V_2 are given by $D = \frac{Rs}{Rs+R1+R2} = 0.819$, using the values shown in Fig. A.2. From Faraday's law,

$$V_\epsilon = -\int \dot{\mathbf{B}} \cdot \, d\mathbf{A} = -A_i \dot{B}_i. \tag{A.2}$$

The subscript $i = \{1, 2, 3\}$ denotes the separate components of the vector area A_i and $\dot{B}_i$. The right most equality in Eq. A.2 holds for a uniform B-field, which is assumed at the spacial scale of the probes. Relating the emf voltage to the measured voltages, V_1 and V_2, is accomplished by examining the voltage at nodes V_a and V_b, shown in Fig. A.2. This gives,

$$V_\epsilon = V_a - V_b = \frac{1}{D(V_1 - V_2)}. \tag{A.3}$$

Combining Eqs. A.2 and A.3 gives,

$$\dot{B_i} = \frac{V_2 - V_1}{A_i D}. \tag{A.4}$$

After calculating the area A_i for each coil, Eq. A.4 is used to convert the measured voltage signal from the 2106 digitizers to a B-dot Tesla per second value.

A.2 Flux Array 1 and 2

Flux Arrays 1 and 2, shown in Fig. A.3(a), represent the latest generation of B-dot probe arrays developed by the TREX group. Their design enables time-resolved measurements of plasma evolution within the plane of the array throughout a single discharge event. This capability was essential for performing the volumetric scans of the mini-magnetosphere discussed in Chapter 3, and for capturing the temporal evolution of the Drive Cylinder reconnection layer described in Chapter 2. These different experimental arrangements where captured with the modular joint design, which allows the arrays to be oriented in multiple configurations, as illustrated in panel (a) for the Drive Cylinder and panel (b) for the mini-magnetosphere.

Flux Array 1 served as the pathfinder for this design, utilizing only Z-direction PCB pick-up coils, as illustrated in the inset panels of Fig. A.3(a). Specifically, every other Z pick-up coil was used, resulting in 96 probes in total, with 12 $\dot{B}_z$ probes per stick. Flux Array 2 extended this capability, incorporating 12 $\dot{B}_z$ probes,10 $\dot{B}_R$ and 10 $\dot{B}_\phi$ pick-up loops per stick, for a total of 256 B-dot probes. The digitizers operate at a 10 MHz sampling frequency, corresponding to a temporal resolution of 0.1 μs.

The main limitation of the arrays is their relatively low spatial resolution within the measurement plane, due to the 0.12 m separation between sticks and the 0.05 m spacing between probes along each stick. To address this limitation, section A.3 introduces a linear array of pick-up loops, referred to as the *Lightsaber probe*, which provides significantly

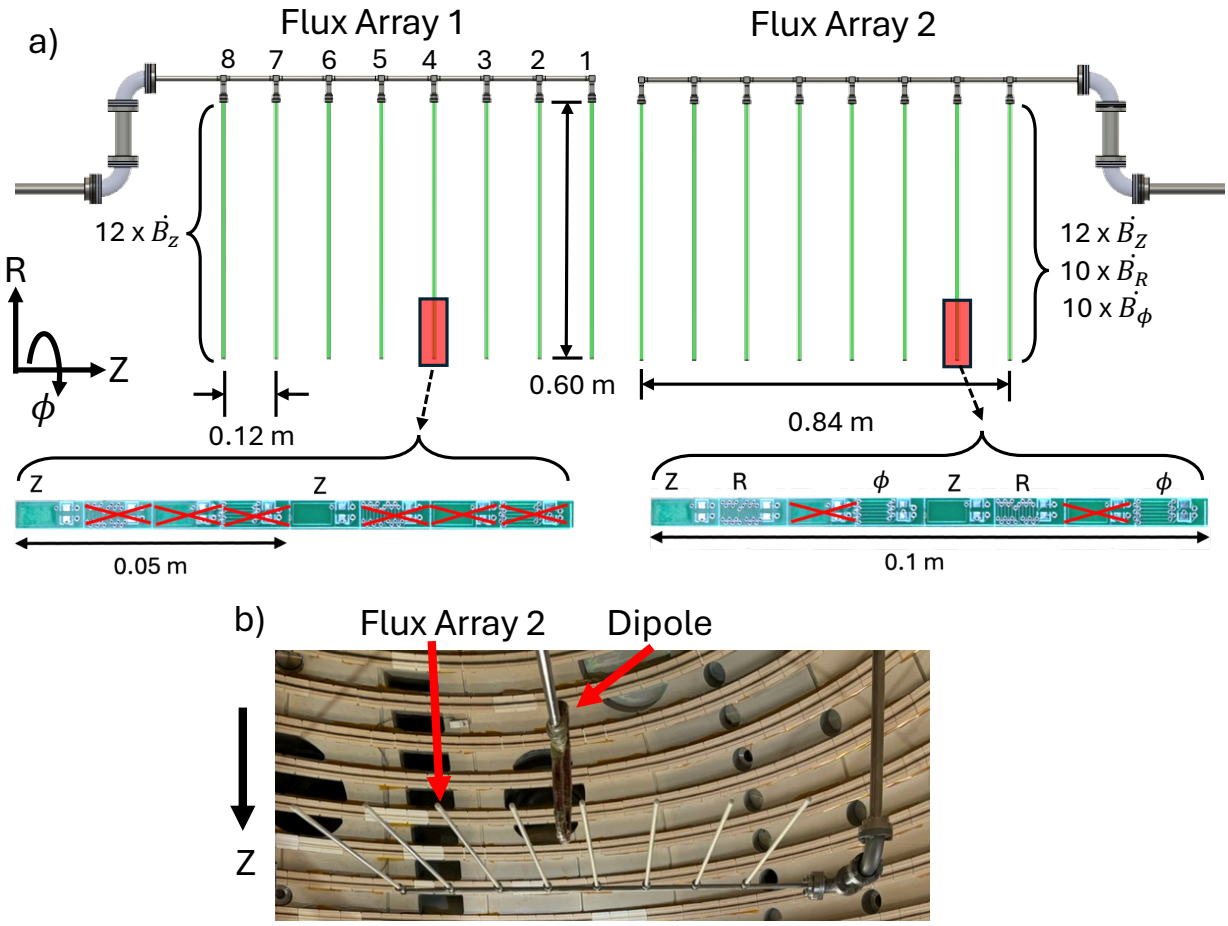

Figure A.3: A CAD render of Flux Array 1 and 2 is shown in Panel (a), with each subplot indicating the PCB pick-up loops utilized in the two Flux Arrays. Panel (b) is an image of Flux Array 2 installed in the mini-magnetosphere configuration. Using the measured B_z signal from single stick, panel (c) demonstrates how the approximate velocity of the reconnection layer, V_{layer} , is determined by the slope of the $B_z = 0$ contour, red line.

higher spatial resolution.

A.2.1 The Scalar Flux Function

The name of these arrays originates from their ability to measure the magnetic flux function in systems with toroidal, or azimuthal, symmetry, such as the Drive Cylinder. This relationship can be demonstrated by starting from $\nabla \cdot \mathbf{B} = 0$ and assuming azimuthal

symmetry, $\partial/\partial\phi = 0$, which gives

$$\frac{\partial}{\partial r}(rB_r) = -\frac{\partial}{\partial z}(rB_z).$$

This expression allows the magnetic field components to be written in terms of a scalar flux function, ψ, as

$$B_r = -\frac{1}{r}\frac{\partial\psi}{\partial z}, \qquad B_z = \frac{1}{r}\frac{\partial\psi}{\partial r}, \tag{A.5}$$

where ψ represents the is the scalar flux function.

From the general relation $\mathbf{B} = \nabla \times \mathbf{A}$ and again assuming $\partial/\partial\phi = 0$, the components of $\mathbf{B}$ can be expressed as

$$B_r = -\frac{\partial A_\phi}{\partial z}, \qquad B_\phi = \frac{\partial A_r}{\partial z} - \frac{\partial A_z}{\partial r}, \qquad B_z = \frac{1}{r}\frac{\partial(rA_\phi)}{\partial r}.$$

By comparing the two expressions for B_r or B_z, we obtain a direct relation between the flux function and the azimuthal component of the vector potential:

$$\psi = rA_\phi. \tag{A.6}$$

Taking the gradient of the flux function gives

$$\nabla\psi = \frac{\partial}{\partial r}\left(rA_\phi\right)\hat{\mathbf{r}} + r\,\frac{\partial A_\phi}{\partial z}\,\hat{\mathbf{z}}.$$

This allows the poloidal magnetic field, $\mathbf{B}_{\text{pol}} = B_r\hat{\mathbf{r}} + B_z\hat{\mathbf{z}}$, to be expressed in terms of the flux function as

$$\mathbf{B}_{\text{pol}} = \frac{1}{r}\,\nabla\psi \times \hat{\boldsymbol{\phi}}. \tag{A.7}$$

It immediately follows that $\mathbf{B}\cdot\nabla\psi = (B_t\hat{\boldsymbol{\phi}} + \mathbf{B}_{\text{pol}})\cdot\nabla = 0$, meaning that surfaces of constant scalar flux function are parallel to magnetic field lines. This allows one to use contours of

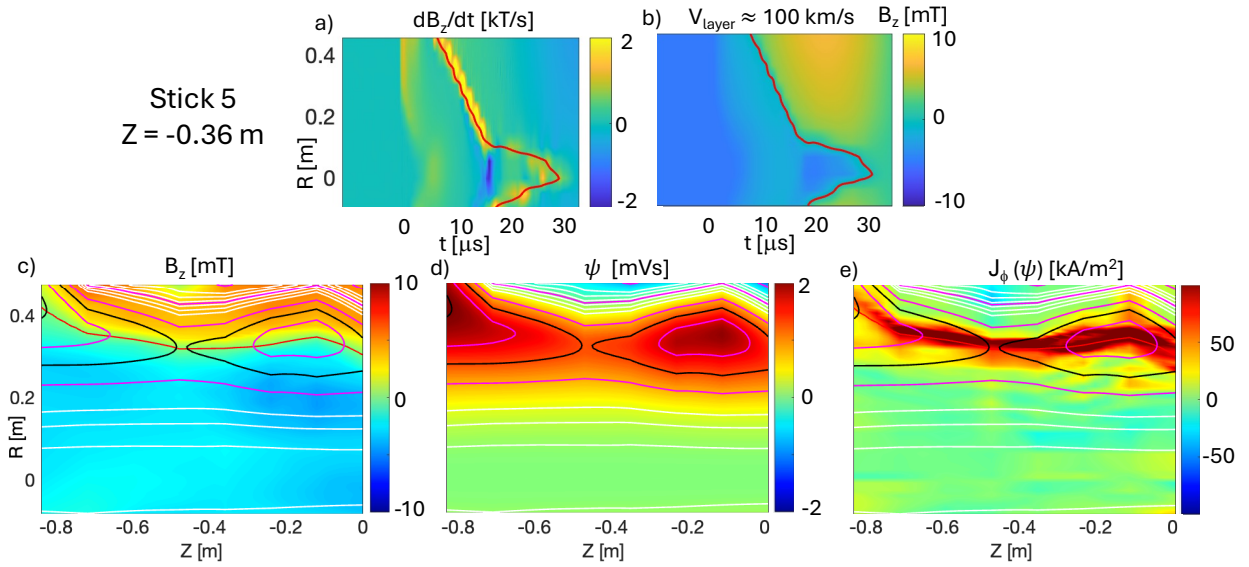

Figure A.4: Measurements from Flux Array 2 positioned in the RZ-plane of the Drive Cylinder, as shown in Fig. 2.17(a)). Panels (a) and (b) are from stick 5, with the radial speed of the reconnection layer being calculated from the slope of the $B_z = 0$ contour. Panels (c–d) show plots B_z, the flux function ψ, and J_ϕ from the plane of the flux array.

constant ψ to represent magnetic field lines in the poloidal plane.

The scalar flux function can be directly related to the poloidal magnetic flux through

$$\Phi_{pol} = \int \mathbf{B}_{pol} \cdot d\mathbf{a} = \int \left(\frac{1}{r} \nabla\psi \times \hat{\boldsymbol{\phi}} \right) \cdot \hat{\mathbf{z}}\, r\, d\phi\, dr = 2\pi \int_0^R \frac{\partial \psi}{\partial r}\, dr,$$

which gives

$$\Phi_{pol}(t, R) = 2\pi \int_0^R B_z(t, r)\, r\, dr = 2\pi\, \psi(t, R). \tag{A.8}$$

Measurements of the poloidal flux are obtained using each probe stick of the flux array, as shown in Fig. A.4(b), where the time-integrated B_z signals from pick-up coils spaced every 0.05 m are plotted for a single stick. Combining the scalar flux functions from all sticks produces the two-dimensional $\psi(t, R, Z)$. A representative example of the measured flux function is shown in panel (d), derived from the integrated field data in panel (c).

A.2.2 Toroidal Current Density

The poloidal current density, J_ϕ, can be expressed in terms of the flux function, which depends only on B_z, the probe component with the highest spatial density and strongest signal. This relationship can be derived starting from Ampér's law,

$$\nabla \times \mathbf{B} = \mu_0 \mathbf{J},$$

and expressing the magnetic field in terms of its toroidal and poloidal components,

$$\mathbf{B} = B_\phi \hat{\boldsymbol{\phi}} + \frac{1}{r} \nabla\psi \times \hat{\boldsymbol{\phi}}.$$

For an azimuthally symmetric system, where $\partial/\partial\phi = 0$, taking the curl of $\mathbf{B}$ gives

$$\nabla \times (B_\phi \hat{\boldsymbol{\phi}}) - \frac{1}{r}\left[\frac{\partial^2}{\partial z^2} + r\,\frac{\partial}{\partial r}\left(\frac{1}{r}\frac{\partial}{\partial r}\right)\right]\psi\,\hat{\boldsymbol{\phi}} = \mu_0 \mathbf{J}. \tag{A.9}$$

The first term on the left-hand side corresponds to the poloidal component of the current density, while the bracketed portion of the second term is the elliptic operator,

$$\nabla^* = \frac{\partial^2}{\partial z^2} + r\,\frac{\partial}{\partial r}\left(\frac{1}{r}\frac{\partial}{\partial r}\right).$$

The toroidal current density can therefore be written as

$$J_\phi = -\frac{1}{\mu_0 r}\nabla^*\psi. \tag{A.10}$$

A representative example of applying equation A.10 using Flux Array 2 is shown in Fig. A.4(e).

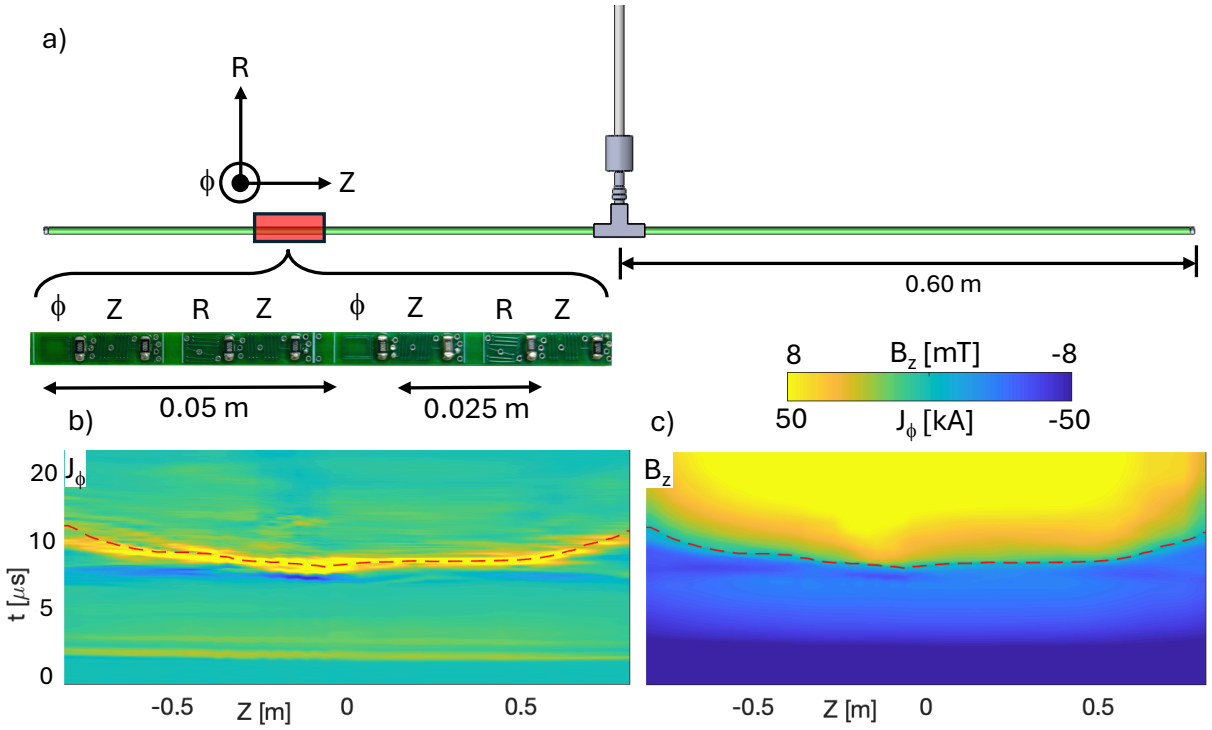

Figure A.5: Panel (a) is a CAD render of the Lightsaber probe where the associated PCB pick-up coil array. Panels (b) and (c) are the toroidal current density, J_ϕ and reconnection magnetic field, B_z, respectively, for a representative Drive Cylinder current layer. These plots show data from single discharge event.

A.3 Lightsaber Probe

The Lightsaber probe, shown in Fig. A.5(a), is a pick-up loop array consisting of 128 B-dot probes. Each half of the array contains 16 $\dot{B}_R$, 16 $\dot{B}_\phi$, and 32 $\dot{B}_Z$ coils, with probe spacings of 0.05 m, 0.05 m, and 0.025 m, respectively. The PCB layout differs slightly from that of the Flux Arrays, with the shapes of the ϕ and Z pick-up loops interchanged. This modification allows a higher density of Z-oriented probes to align with the dominant magnetic field when the long axis of the array is oriented parallel to the Drive Cylinder axis.

In addition to the higher density of $\dot{B}_Z$ probes, the spatial resolution is further enhanced using the *Jogging Method* [68], a technique first applied to spacecraft measurements [104]. This method assumes that the magnetic structure moves uniformly across a fixed probe location with minimal intrinsic evolution. Under this assumption, the time variation

measured by a stationary probe can be interpreted as the spatial variation of the moving structure, allowing temporal data to be mapped to spatial profiles via the structure's velocity. Both the Flux Arrays and the Lightsaber array employ this technique. The Flux Arrays serve two primary roles: first, to confirm that the magnetic features remain quasi-stationary as they traverse the measurement region, and second, to determine the transit velocity of the magnetic structure. A representative measurement of the transit velocity is shown in Fig. A.3(c), where the slope of the $B_Z = 0$ contour indicates the velocity of the reconnection layer. With a sampling rate of 10 MHz and a typical layer velocity of $V_{\text{layer}} \approx 100\,\text{km/s}$, a radial resolution of approximately 1 cm is achieved.

An additional advantage of this technique is its ability to measure the toroidal current density, J_ϕ, within the Drive Cylinder reconnection layer, as shown in Fig. A.5(b). Due to the approximate toroidal symmetry of the Drive Cylinder and the small magnitude of B_r, the toroidal current density is nearly proportional to $\dot{B}_Z$. This follows from the ϕ component of Ampère's law,

$$\frac{\partial B_r}{\partial z} - \frac{\partial B_z}{\partial r} = \mu_0 J_\phi.$$

Using the Jogging Method, the radial derivative can be replaced by a time derivative, $\frac{\partial}{\partial r} \approx \frac{1}{V_{\text{layer}}}\frac{\partial}{\partial t}$, where V_{layer} is the transit velocity of the current layer. Neglecting the small $\frac{\partial B_r}{\partial z}$ term gives

$$J_\phi \approx -\frac{1}{\mu_0 V_{\text{layer}}}\frac{\partial B_z}{\partial t}, \tag{A.11}$$

demonstrating that the toroidal current density can be directly inferred from the time evolution of B_z.

A.4 T_e Probe

TREX employs arrays of electrostatic Langmuir probes to measure the plasma density n, electron temperature T_e, and plasma potential V_p. A Langmuir probe consists of a biased

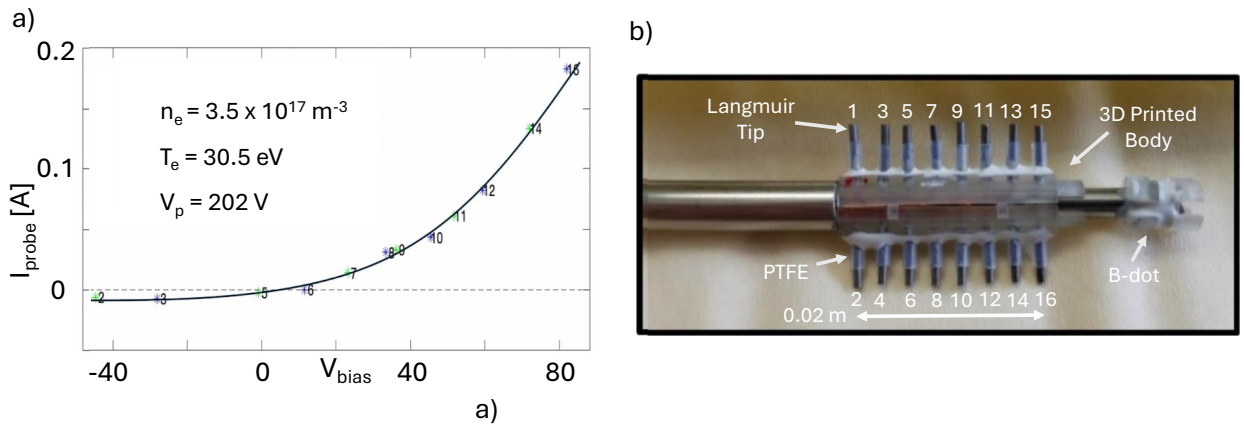

Figure A.6: Panel (d) is a representative I-V curve fit of equation A.12 using the voltage values from each tip just prior to energizing the drive coils. Panel (a) is the 16-tip Langmuir T_e probe. Panel (b) shows the T_e probe circuit diagram.

electrode at potential V_{prb} immersed in a plasma at potential V_p. The resulting voltage difference drives a current, whose characteristics can be used to infer key plasma parameters. The validity of this analysis relies on several simplifying assumptions: (i) the plasma is isotropic with a Maxwellian electron distribution, (ii) the characteristic dimension of the probe is smaller than the Debye length, $\lambda_D = \sqrt{\epsilon_0 T_e/(ne^2)}$, and (iii) the ion temperature is much less than the electron temperature, $T_i < T_e$. Under these conditions, standard Langmuir probe theory applies.

When $V_{prb} < V_p$, the total probe current is given by

$$I_{prb}(V_{prb}) = neA_p \left(\frac{T_e}{m_i}\right)^{1/2} \left[\left(\frac{m_i}{2\pi m_e}\right)^{1/2} \exp\left(\frac{e(V_{prb}-V_p)}{T_e}\right) - \exp\left(\tfrac{1}{2}\right)\right], \qquad (A.12)$$

where A_p is the probe area, with the first and second terms corresponding to the ion and electron contributions, respectively. A complete derivation of Eq. A.12, along with justification of the underlying assumptions, is provided in Ref. [42]. An application of this framework to TREX conditions can be found in Ref. [69]. By fitting the measured current–voltage (I–V) data to Eq. A.12, the parameters n, T_e, and V_p are directly extracted. This technique is illustrated in Fig. 3.2(a), where the numbered stars are measurements

from tips and the exponential curve is fitted to the measured stars using equation A.12.

The conventional approach of sweeping the tip voltage of a Langmuir probe in time is not practical for TREX. This is due to the reconnection layer transiting the experimental region in 20–50 μs. To overcome this limitation, TREX uses a single T_e probe with 16 Langmuir tips (Fig. A.6), each biased to a different potential. This configuration yields a complete I–V characteristic every 0.1 μs using 10 MHz digitizers, providing the temporal resolution necessary to capture the rapidly evolving plasma dynamics.

In addition to the Langmuir probe tips, the Te probe is equipped with a hand-wound B-dot coil assembly that measures all three orthogonal magnetic field components. The primary purpose of these B-dot coils is to provide temporal alignment between the Langmuir probe measurements and the magnetic field data obtained from other B-dot arrays.

A.5 Plasma Gun

The washer gun design was first developed for the Madison Symmetric Torus [31] and, after substantial improvements, is currently employed in the Pegasus experiment as a means of injecting local helicity [5]. For both the Drive Cylinder and mini-magnetosphere experiments, a hexagonal array of six plasma washer guns, shown in Fig. A.7, served as the plasma source. The guns operate by introducing neutral gas into the ionization chamber (Fig. A.7(a1–a5)), which consists of a molybdenum anode and cathode separated by alternating molybdenum and boron nitride washers. The resulting ionized plasma is then expelled into the BRB vacuum vessel at the sound speed. Typical background plasma parameters achieved with this configuration are densities of order 10^{17} m^{-3} and electron temperatures of 3–5 eV.

Each gun is powered by its own pulse-forming network (PFN), specifically designed for this application. These power supplies provide an initial voltage spike exceeding 500 V to initiate breakdown, followed by a sustained current of 1 kA at 100 V for 10 ms. A more

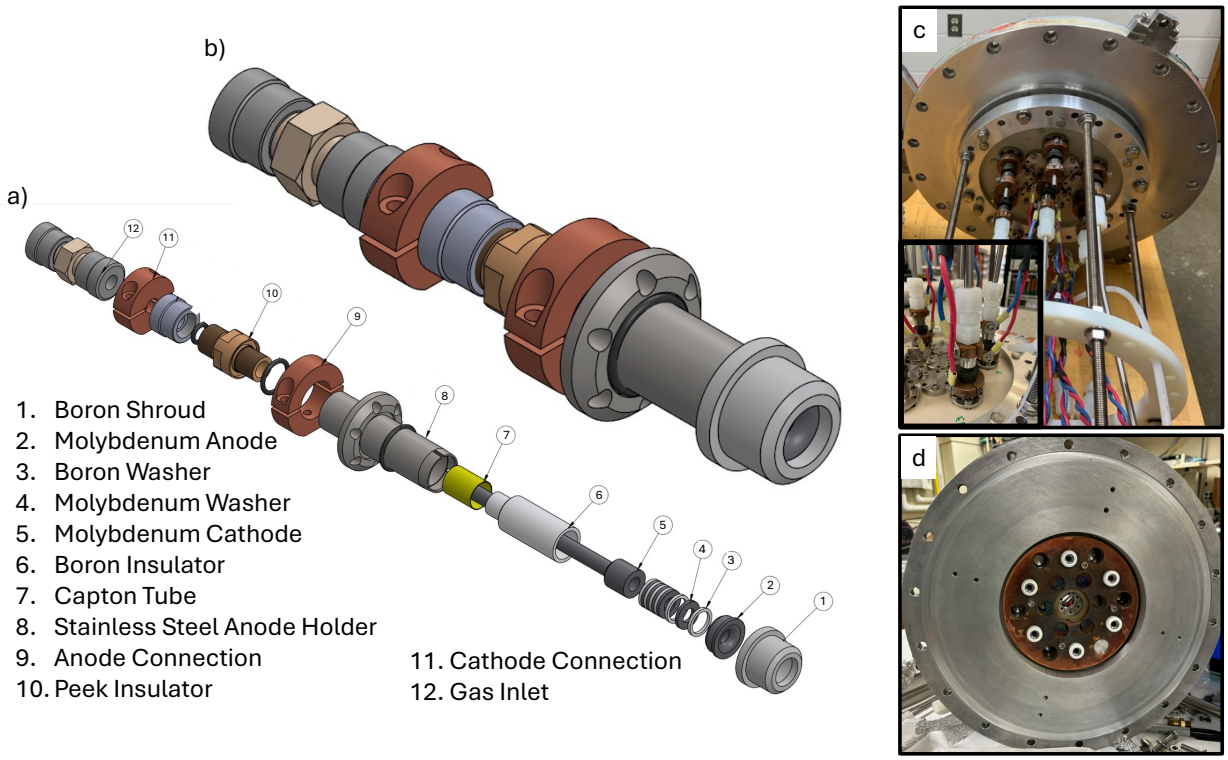

Figure A.7: Panels (a) and (b) are images of the hexagon shaped plasma gun array. Panels (c,d) are CAD renders of a plasma gun, with (d) being an exploded view of the different parts.

detailed description of both the washer guns and their PFNs can be found in Brookhart [7] and Endrizzi [30].

A.6 Snubber

During the first run campaign of the Drive Cylinder, a high-frequency ringing persisted for the first 10 μs following the energization of the drive coils. This oscillation was observed in both the B-dot and T_e probes, with the latter being particularly sensitive to the noise. To mitigate these effects, a coaxial low-inductance RC snubber (shown in Fig. A.8) was installed, which successfully suppressed the high-frequency oscillations.

After a six-month trial-and-error process, that included simulating the system with LT spice, it was determined that the inductance of the snubber played a critical role in

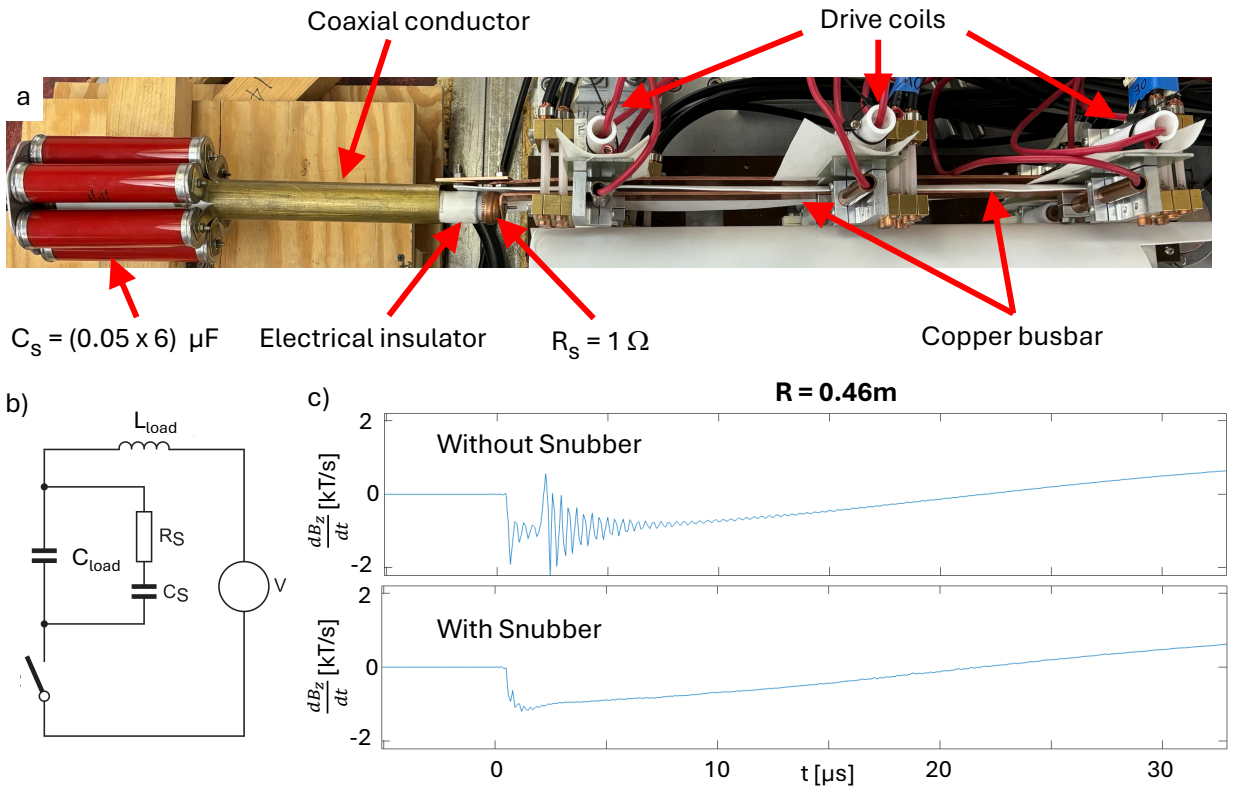

Figure A.8: Panel (a) is an image of the snubber install with the TREX 3 drive coil setup. Panel (b) is a simplified snubber circuit. Pane (c) are time trace plots from a B-dot probe at R = 0.46 m.

its effectiveness. Specifically, connecting a standard RC snubber with high-voltage leads proved ineffective, since the added lead inductance prevented the snubber from functioning as part of the circuit. The coaxial design minimizes inductance by keeping the current return path close to the source, thereby ensuring the snubber can act on the rapid transients responsible for the ringing. In this configuration, the capacitor shunts high-frequency components while the resistor dissipates their energy, successfully damping resonant oscillations in the system.

By suppressing these oscillations, the snubber greatly improved the signal quality of plasma diagnostics, as seen in the B-dot traces of Fig. A.8(c). In particular, the T_e probes, which were previously dominated by high-frequency noise when the current layer transited past them, subsequently produced reliable signals at the critical current transit time.

REFERENCES

[1] Berchem, J., and C. T. Russell. 1982. The thickness of the magnetopause current layer: Isee 1 and 2 observations. *JGR* 87(A4):2108–2114.

[2] Birn, J., A. V. Artemyev, D. N. Baker, M. Echim, M. Hoshino, and L. M. Zelenyi. 2012. Particle acceleration in the magnetotail and aurora. *Space Science Reviews* 173(1): 49–102.

[3] Birn, J., J. F. Drake, M. A. Shay, B. N. Rogers, R. E. Denton, M. Hesse, M. Kuznetsova, Z. W. Ma, A. Bhattacharjee, A. Otto, and P. L. Pritchett. 2001. Geospace environmental modeling (gem) magnetic reconnection challenge. *Journal of Geophysical Research: Space Physics* 106(A3):3715–3719.

[4] Bolaños, S., A. Sladkov, R. Smets, S. N. Chen, A. Grisollet, E. Filippov, J.-L. Henares, V. Nastasa, S. Pikuz, R. Riquier, M. Safronova, A. Severin, M. Starodubtsev, and J. Fuchs. 2022. Laboratory evidence of magnetic reconnection hampered in obliquely interacting flux tubes. *Nature Communications* 13(1):6426.

[5] Bongard, M.W., G.M. Bodner, M.G. Burke, R.J. Fonck, J.L. Pachicano, J.M. Perry, C. Pierren, J.A. Reusch, A.T. Rhodes, N.J. Richner, C. Rodriguez Sanchez, C.E. Schaefer, and J.D. Weberski. 2019. Advancing local helicity injection for non-solenoidal tokamak startup. *Nuclear Fusion* 59(7):076003.

[6] Braginskii, S. 1965. Transport processes in a plasma. *Rev. Plamsa Phys.* 1:205.

[7] Brookhart, Matthew. 2015. Subcritical onse of plasma fluctuations and magnetic self-orginization in a line-tied screw pinch. Phd dissertation, University of Wisconsin Madison.

[8] Browning, P. K., C. Gerrard, A. W. Hood, R. Kevis, and R. A. M. Van der Linden. 2008. Heating the corona by nanoflares: simulations of energy release triggered by a kink instability. *A&A* 485(3):837–848.

[9] Cassak, P. A., and M. A. Shay. 2007. Scaling of asymmetric magnetic reconnection: General theory and collisional simulations. *Physics of Plasmas* 14(10):102114.

[10] Coppi, B., G. Laval, and R. Pellat. 1966. Dynamics of the geomagnetic tail. *Phys. Rev. Lett.* 16:1207–1210.

[11] Cowling, T.G. 1953. Solar electrodynamics. In *The sun*, ed. Gerard Peter Kuiper, 532.

[12] Dahlin, J. T. 2020. Adiabatic acceleration in a magnetotail flux rope. *Geophysical Research Letters* 47(11):e2020GL087918.

[13] Daughton, W., and V. Roytershteyn. 2011. Emerging parameter space map of magnetic reconnection in collisional and kinetic regimes. *Space Science Reviews - SPACE SCI REV* 172:1–12.

[14] Daughton, W., V. Roytershteyn, H. Karimabadi, L. Yin, B. Albright, B. Bergen, and K. Bowers. 2011. Role of electron physics in the development of turbulent magnetic reconnection in collisionless plasmas. *Nature Physics* 7:539–542.

[15] Denton, R. E., B. U. O. Sonnerup, C. T. Russell, H. Hasegawa, T.-D. Phan, R. J. Strangeway, B. L. Giles, R. E Ergun, P.-A. Lindqvist, R. B. Torbert, J. L Burch, and S. K. Vines. 2018. Determining l-m-n current sheet coordinates at the magnetopause from magnetospheric multiscale data. *Journal of Geophysical Research: Space Physics* 123(3):2274–2295.

[16] Dorelli, John C., Amitava Bhattacharjee, and Joachim Raeder. 2007. Separator reconnection at earth's dayside magnetopause under generic northward interplanetary magnetic field conditions. *Journal of Geophysical Research: Space Physics* 112(A2).

[17] Dorfman, S., H. Ji, M. Yamada, J. Yoo, E. Lawrence, C. Myers, and T. D. Tharp. 2013. Three-dimensional, impulsive magnetic reconnection in a laboratory plasma. *Geophysical Research Letters* 40(2):233–238.

[18] Drake, J, Marc Swisdak, Haihong Che, and Michael Shay. 2006. Electron acceleration from contracting magnetic islands during reconnection. *Nature* 443:553–6.

[19] Drake, J. F., M. A. Shay, and M. Swisdak. 2008. The hall fields and fast magnetic reconnection. *Physics of Plasmas* 15(4):042306.

[20] Dungey, J. W. 1961. Interplanetary magnetic field and the auroral zones. *Phys. Rev. Lett.* 6:47–48.

[21] Dungey, J.W. 1953. Lxxvi. conditions for the occurrence of electrical discharges in astrophysical systems. *The London, Edinburgh, and Dublin Philosophical Magazine and Journal of Science* 44(354):725–738.

[22] Eastman, T. E., S. A. Fuselier, and J. T. Gosling. 1996. Magnetopause crossings without a boundary layer. *Journal of Geophysical Research: Space Physics* 101(A1):49–57.

[23] Egedal, J., W. Daughton, and A. Le. 2012. Large-scale electron acceleration by parallel electric fields during magnetic reconnection. *Nature Physics* 8(4):321–324.

[24] Egedal, J., W. Daughton, A. Le, and A. L. Borg. 2015. Double layer electric fields aiding the produc- tion of energetic flat-top distributions and superthermal electrons within magnetic reconnection exhausts. *Phys. Plasmas* 22.

[25] Egedal, J., W. Fox, N. Katz, M. Porkolab, M. Øieroset, R. P. Lin, W. Daughton, and J. F. Drake. 2008. Evidence and theory for trapped electrons in guide field magnetotail reconnection. *Journal of Geophysical Research: Space Physics* 113(A12).

[26] Egedal, J., H. Gurram, S. Greess, W. Daughton, and A. Lê. 2023. The force balance of electrons during kinetic anti-parallel magnetic reconnection. *Physics of Plasmas* 30(6):062106.

[27] Egedal, J., A. Lê, and W. Daughton. 2013. A review of pressure anisotropy caused by electron trapping in collisionless plasma, and its implications for magnetic reconnection. *Physics of Plasmas* 20(6):061201.

[28] Egedal, J., M. Øieroset, W. Fox, and R. P. Lin. 2005. In situ discovery of an electrostatic potential, trapping electrons and mediating fast reconnection in the earth's magnetotail. *Phys. Rev. Lett.* 94:025006.

[29] Egedal, Jan, Noam Katz, Jeff Bonde, Will Fox, Ari Le, Miklos Porkolab, and Arturs Vrublevskis. 2011. Spontaneous onset of magnetic reconnection in toroidal plasma caused by breaking of 2d symmetry. *Physics of Plasmas* 18(11):111203.

[30] Endrizzi, Douglass. 2015. The formation of parallel and perpendicual collisionless shocks in the big red ball. Phd dissertation, University of Wisconsin Madison.

[31] Fiksel, G, A F Almagri, D Craig, M Iida, S C Prager, and J S Sarff. 1996. High current plasma electron emitter. *Plasma Sources Science and Technology* 5(1):78.

[32] Forest, C. B., K. Flanagan, M. Brookhart, M. Clark, et al. 2015. The wisconsin plasma astrophysics laboratory. *Journal of Plasma Physics* 81(5).

[33] Fukao, S., M. Ugai, and T. Tsuda. 1975. Topological study of magnetic field near a neutral point. *Report of Ionosphere and Space Research in Japan* 29(3):133–139.

[34] Giovanelli, R. G. 1947. Magnetic and electric phenomena in the sun's atmosphere associated with sunspots. *Monthly Notices of the Royal Astronomical Society* 107:338.

[35] Gradney, P., J. Egedal, I. Barnhill, R. Flores-García, S. Greess, C. Kuchta, J. Olson, J. Wallace, X. Yu, and C. Forest. 2023. Implementation of a drive cylinder for low

collisional experiments on magnetic reconnection. *Review of Scientific Instruments* 94(12):123503.

[36] Greene, John M. 1992. Locating three-dimensional roots by a bisection method. *Journal of Computational Physics* 98(2):194–198.

[37] Greess, S., J. Egedal, A. Stanier, W. Daughton, J. Olson, A. Lê, R. Myers, A. Millet-Ayala, M. Clark, J. Wallace, D. Endrizzi, and C. Forest. 2021. Laboratory verification of electron-scale reconnection regions modulated by a three-dimensional instability. *Journal of Geophysical Research: Space Physics* 126(7):e2021JA029316.

[38] Greess, S., J. Egedal, A. Stanier, J. Olson, W. Daughton, A. Lê, A. Millet-Ayala, C. Kuchta, and C. B. Forest. 2022. Kinetic simulations verifying reconnection rates measured in the laboratory, spanning the ion-coupled to near electron-only regimes. *Physics of Plasmas* 29(10):102103.

[39] Guo, Ruilong, Zuyin Pu, Xiaogang Wang, Chijie Xiao, and Jiansen He. 2022. 3d reconnection geometries with magnetic nulls: Multispacecraft observations and reconstructions. *Journal of Geophysical Research: Space Physics* 127(2):e2021JA030248.

[40] Hesse, Michael, Terry G. Forbes, and Joachim Birn. 2005. On the relation between reconnected magnetic flux and parallel electric fields in the solar corona. *The Astrophysical Journal* 631(2):1227.

[41] Hornig, Gunnar, and Lutz Rastätter. 1998. The magnetic structure of b $\neq$ 0 reconnection. *Physica Scripta* 1998(T74):34.

[42] Hutchinson, I. H. 2002. *Principles of plasma diagnostics*. 2nd ed. Cambridge University Press.

[43] Ji, H., and W. Daughton. 2011. Phase diagram for magnetic reconnection in heliophysical, astrophysical, and laboratory plasmas. *Physics of Plasmas* 18(11):111207.

[44] Ji, Hantao, William Daughton, Jonathan Jara-Almonte, Ari Le, Adam Stanier, and Jongsoo Yoo. 2022. Magnetic reconnection in the era of exascale computing and multiscale experiments. *Nature Reviews Physics* 4(4):263–282.

[45] Kleva, Robert G., J. F. Drake, and F. L. Waelbroeck. 1995. Fast reconnection in high temperature plasmas. *Physics of Plasmas* 2(1):23–34.

[46] Lau, Yun-Tung, and John M. Finn. 1990. Three-dimensional kinematic reconnection in the presence of field nulls and closed field lines. *APJ* 350:672.

[47] Lawrence, Eric E., Hantao Ji, Masaaki Yamada, and Jongsoo Yoo. 2013. Laboratory study of hall reconnection in partially ionized plasmas. *Phys. Rev. Lett.* 110:015001.

[48] Lazzeri, Chiara, Andrey Samsonov, Colin Forsyth, Graziella Branduardi-Raymont, and Yulia V. Bogdanova. 2024. A statistical study of the properties of, and geomagnetic responses to, large, rapid southward turnings of the interplanetary magnetic field. *Journal of Geophysical Research: Space Physics* 129(9).

[49] Le, A., J. Egedal, W. Daughton, J. F. Drake, W. Fox, and N. Katz. 2010. Magnitude of the hall fields during magnetic reconnection. *Geophysical Research Letters* 37(3).

[50] Le, A., J. Egedal, W. Daughton, W. Fox, and N. Katz. 2009. Equations of state for collisionless guide-field reconnection. *Phys. Rev. Lett.* 102:085001.

[51] Lê, A., J. Egedal, W. Daughton, V. Roytershteyn, H. Karimabadi, and C. Forest. 2015. Transition in electron physics of magnetic reconnection in weakly collisional plasma. *Journal of Plasma Physics* 81(1).

[52] Le, A., J. Egedal, O. Ohia, W. Daughton, H. Karimabadi, and V. S. Lukin. 2013. Regimes of the electron diffusion region in magnetic reconnection. *Phys. Rev. Lett.* 110:135004.

[53] Leake, James E., Lars K. S. Daldorff, and James A. Klimchuk. 2020. The onset of 3d magnetic reconnection and heating in the solar corona. *The Astrophysical Journal* 891(1):62.

[54] Li, Xiaocan, Fan Guo, and Yi-Hsin Liu. 2021. The acceleration of charged particles and formation of power-law energy spectra in nonrelativistic magnetic reconnection. *Physics of Plasmas* 28(5):052905.

[55] Liu, Yi-Hsin, Prayash Pyakurel, Xiaocan Li, Michael Hesse, Naoki Bessho, Kevin Genestreti, and Shiva B. Thapa. 2025. An analytical model of "Electron-Only" magnetic reconnection rates. *Communications Physics* 8(1):128.

[56] Longcope, D. W., D. E. McKenzie, J. Cirtain, and J. Scott. 2005. Observations of separator reconnection to an emerging active region. *The Astrophysical Journal* 630(1).

[57] Loureiro, N. F., A. A. Schekochihin, and S. C. Cowley. 2007. Instability of current sheets and formation of plasmoid chains. *Physics of Plasmas* 14(10):100703.

[58] Lynch, B. J., S. K. Antiochos, C. R. DeVore, J. G. Luhmann, and T. H. Zurbuchen. 2008. Topological evolution of a fast magnetic breakout cme in three dimensions. *The Astrophysical Journal* 683(2):1192.

[59] Masuda, S, T Kosugi, H. Hara, S. Tsuneta, and Y. Ogawara. 1994. A loop top hard x-ray source in a compact solar-flare as evidence for magnetic rconnection. *Nature* 371(6497):495–497.

[60] Masuda, S., T. Kosugi, H. Hara, S. Tsuneta, and Y. Ogawara. 1994. A loop-top hard x-ray source in a compact solar flare as evidence for magnetic reconnection. *Nature* 371(6497):495–497.

[61] McPherron, R. L., C. T. Russell, and M. P. Aubry. 1973. Satellite studies of magnetospheric substorms on august 15, 1968: 9. phenomenological model for substorms. *Journal of Geophysical Research* 78(16):3131–3149.

[62] Montag, P., J. Egedal, E. Lichko, and B. Wetherton. 2017. Impact of compressibility and a guide field on fermi acceleration during magnetic island coalescence. *Physics of Plasmas* 24(6):062906.

[63] Montag, Peter, Jan Egedal, and William Daughton. 2020. Influence of inflow density and temperature asymmetry on the formation of electron jets during magnetic reconnection. *Geophysical Research Letters* 47(20):e2020GL087612.

[64] ya Nitta, Shin, and Koji Kondoh. 2021. Fundamental properties of sheared/guide field mhd magnetic reconnection. *The Astrophysical Journal* 907(1):21.

[65] Northrop, Theodore G. 1963. Adiabatic charged-particle motion. *Reviews of Geophysics* 1(3):283–304.

[66] Nykyri, Katariina. 2024. Giant kelvin-helmholtz (kh) waves at the boundary layer of the coronal mass ejections (cmes) responsible for the largest geomagnetic storm in 20 years. *Geophysical Research Letters* 51(20):e2024GL110477.

[67] Oka, Mitsuo, Joachim Birn, Jan Egedal, Fan Guo, Robert Ergun, Drew Turner, Yuri Khotyaintsev, Kyoung-Joo Hwang, Ian Cohen, and James Drake. 2023. Particle acceleration by magnetic reconnection in geospace. *Space Science Reviews* 219.

[68] Olson, J., J. Egedal, S. Greess, R. Myers, M. Clark, D. Endrizzi, K. Flanagan, J. Milhone, E. Peterson, J. Wallace, D. Weisberg, and C. B. Forest. 2016. Experimental demonstration of the collisionless plasmoid instability below the ion kinetic scale during magnetic reconnection. *Phys. Rev. Lett.* 116(25).

[69] Olson, Joseph. 2020. Exploring driven, high lundquist number magnetic reconnection: Studies of sub-ion scale plasmoids, and the interplay between shocks and magnetic flux pile-up. Phd dissertation, University of Wisconsin Madison.

[70] Olson, Joseph, Jan Egedal, Michael Clark, Douglass A. Endrizzi, Samuel Greess, Alexander Millet-Ayala, Rachel Myers, Ethan E. Peterson, John Wallace, and Cary B.

Forest. 2021. Regulation of the normalized rate of driven magnetic reconnection through shocked flux pileup. *Journal of Plasma Physics* 87(3).

[71] Omidi, N., X. Blanco-Cano, C.T. Russell, and H. Karimabadi. 2004. Dipolar magnetospheres and their characterization as a function of magnetic moment. *Advances in Space Research* 33(11):1996–2003. Comparative Magnetospheres.

[72] Parker, E. N. 1957. Sweet's mechanism for merging magnetic fields in conducting fluids. *Journal of Geophysical Research (1896-1977)* 62(4):509–520.

[73] Parnell, C. E., A. L. Haynes, and K. Galsgaard. 2010. Structure of magnetic separators and separator reconnection. *Journal of Geophysical Research: Space Physics* 115(A2).

[74] Parnell, C. E., J. M. Smith, T. Neukirch, and E. R. Priest. 1996. The structure of three-dimensional magnetic neutral points. *Physics of Plasmas* 3(3):759–770.

[75] Phan, T. D., J. P. Eastwood, M. A. Ö. Shay, et al. 2018. Electron magnetic reconnection without ion coupling in earth's turbulent magnetosheath. *Nature* 557(7704):202–206.

[76] Phan, T. D., G. Paschmann, J. T. Gosling, M Oieroset, M. Fujimoto, J. F. Drake, and V. Angelopoulos. 2013. The dependence of magnetic reconnection on plasma β and magnetic shear: Evidence from magnetopause observations. *Geophysical Research Letters* 40(1):11–16.

[77] Phan, TD, JT Gosling, MS Davis, RM Skoug, M Oieroset, RP Lin, RP Lepping, DJ McComas, CW Smith, H Reme, and A Balogh. 2006. A magnetic reconnection x-line extending more than 390 earth radii in the solar wind. *Nature* 439(7073): 175–178.

[78] Pontin, David I., and Eric R. Priest. 2022. Magnetic reconnection: Mhd theory and modelling. *Living Reviews in Solar Physics* 19.

[79] Pontin, D.I. 2011. Three-dimensional magnetic reconnection regimes: A review. *Advances in Space Research* 47(9):1508–1522.

[80] Priest, A., and T. Forbes. 2000. *Magnetic reconnection mhd theory and applications*. Cambridge University Press.

[81] Priest, E. R., and T. G. Forbes. 1989. Steady magnetic reconnection in three dimensions. *Solar Physics* 119(1):211–214.

[82] Priest, E. R., and Forbes T. G. 2000. *Magnetic reconnection: Mhd theory and application*. Cambridge University Press.

[83] Priest, ER, and VS Titov. 1996. Magnetic reconnection at three-dimensional null points. *Phil. Trans. Roy. Soc. Lond* 354(1721):2951–2992.

[84] Priest, Eric. 2014. *Magnetohydrodynamics of the sun*. 32 Ave. of the Americas, New York, NY 10013, USA: Cambridge University Press.

[85] Sánchez, Raúl, and David Newman. 2018. *Planetary plasmas: Complex dynamics in the magnetosphere of the earth*, 339–380. Dordrecht: Springer Netherlands.

[86] Schaeffer, D. B., F. D. Cruz, R. S. Dorst, F. Cruz, P. V. Heuer, C. G. Constantin, P. Pribyl, C. Niemann, L. O. Silva, and A. Bhattacharjee. 2022. Laser-driven, ion-scale magnetospheres in laboratory plasmas. i. experimental platform and first results. *Physics of Plasmas* 29(4):042901.

[87] Schindler, K., J. Birn, and M. Hesse. 1991. Magnetic field–aligned electric potentials in nonideal plasma flows. *apj* 380:293.

[88] Schindler, K., M. Hesse, and J. Birn. 1988. General magnetic reconnection, parallel electric fields, and helicity. *Journal of Geophysical Research: Space Physics* 93(A6): 5547–5557.

[89] Schrijver, Carolus J., and George L. Siscoe. 2009. *Heliophysics: Plasma physics of the local cosmos*.

[90] Shay, M. A., J. F. Drake, B. N. Rogers, and R. E. Denton. 1999. The scaling of collisionless, magnetic reconnection for large systems. *Geophysical Research Letters* 26(14): 2163–2166.

[91] Shibata, K, and S Tanuma. 2001. Plasmoid-induced-reconnection and fractal reconnection. *EARTH PLANETS AND SPACE* 53(6):473–482. Symposium on Magnetic Reconnection in Space and Laboratory Plasmas, UNIV TOKYO, TOKYO, JAPAN, FEB 29-MAR 04, 2000.

[92] Shukla, A., and K. Mannheim. 2020. Gamma-ray flares from relativistic magnetic reconnection in the jet of the quasar 3c 279. *Nature Communications* 11(1):4176.

[93] Sweet, P. A. 1958. 14. the neutral point theory of solar flares. *Symposium - International Astronomical Union* 6:123–134.

[94] Swisdak, M., M. Opher, J. F. Drake, and F. Alouani Bibi. 2010. The vector direction of the interstellar magnetic field outside the heliosphere. *The Astrophysical Journal* 710(2):1769.

[95] Swisdak, M., B. N. Rogers, J. F. Drake, and M. A. Shay. 2003. Diamagnetic suppression of component magnetic reconnection at the magnetopause. *Journal of Geophysical Research: Space Physics* 108(A5).

[96] Taylor, J. B. 1986. Relaxation and magnetic reconnection in plasmas. *Rev. Mod. Phys.* 58:741–763.

[97] Tóth, Gábor, Yuxi Chen, Tamas I. Gombosi, Paul Cassak, Stefano Markidis, and Ivy Bo Peng. 2017. Scaling the ion inertial length and its implications for modeling reconnection in global simulations. *Journal of Geophysical Research: Space Physics* 122(10):10,336–10,355.

[98] Vasyliunas, V M. 1975. Theoretical models of magnetic field line merging. i. *Rev. Geophys. Space Phys.* 13:303–336.

[99] Wilmot-Smith, A. L., and E. R. Priest. 2007. Flux tube disconnection: An example of three-dimensional reconnection. *Physics of Plasmas* 14(10):102903.

[100] Wyper, P. F., and D. I. Pontin. 2014. Non-linear tearing of 3d null point current sheets. *Physics of Plasmas* 21(8):082114.

[101] Yamada, Masaaki. 2022. *Magnetic reconnection. a modern synthesis of theory, experiment, and observations*. Princeton University Press.

[102] Yamada, Masaaki, Russell Kulsrud, and Hantao Ji. 2010. Magnetic reconnection. *Rev. Mod. Phys.* 82:603–664.

[103] Ye, Yudong, Xiaojun Xu, Lou-Chuang Lee, Jiang Yu, Jing Wang, Bei Zhu, Qing Chang, Jiaying Xu, Qi Xu, and Zilu Zhou. 2024. In situ observation of mass ejections caused by magnetic reconnections in the ionosphere of mars. *Nature Astronomy* 8(7): 838–845.

[104] Yoo, Jongsoo, and Masaaki Yamada. 2012. Experimental evaluation of common spacecraft data analysis techniques for reconnection region analysis in a laboratory plasma. *Journal of Geophysical Research: Space Physics* 117(A12).

[105] Zweibel, E., and M. Yamada. 2016. Perspectives on magnetic reconnection. *Proceedings of the Royal Society A-Mathematical Physical and Engineering Sciences* 472(2196).